THE DYNAMICS OF CROSS-POLARIZATION COUPLING IN A SINGLE WHISPERING-GALLERY MICRORESONATOR

By

LIMU KE

Bachelor of Science in Physics
Hunan University
Changsha, China
2011

Submitted to the Faculty of the
Graduate College of the
Oklahoma State University
in partial fulfillment of
the requirements for
the Degree of
DOCTOR OF PHILOSOPHY
May, 2019

THE DYNAMICS OF CROSS-POLARIZATION

COUPLING IN A SINGLE WHISPERING-GALLERY

MICRORESONATOR

Dissertation Approved:

Dr. Albert Rosenberger

Dissertation Adviser

Dr. Donna Bandy

Dr. Mario Borunda

Dr. Weili Zhang

ACKNOWLEDGEMENTS

First I would like to thank my advisor, Dr. Albert T. Rosenberger, for his wisdom when helping me to understand various questions and his patience. I learned various experimental techniques and understood the principles behind the experiments under his whole-hearted guidance. I admire his supreme background in both physics and mathematics, his broad spectrum of knowledge in engineering and other fields, and his impeccable writing style. These are the very basis of this dissertation. His is my role model for the rest of my life.

Next I would like to thank my committee members: Dr. Mario Borunda, Dr. Donna Bandy and Dr. Weili Zhang. I appreciate their support and expertise in serving in my advisory committee. I also would like to thank my lab partners: Dr. Khoa Bui, for his kindhearted helps to show me the experimental techniques; Sreekul Raj Rajagopal, for his contribution in experimental data collection and thought-provoking questions every now and then; and Karleyda Sandoval, for her help in setting up a Python model for data analysis. In addition, former undergraduate student Brian Ragsdale also made contributions to the numerical analysis in this work.

Finally, I would like extend my gratitude to the Physics Department: Susan, Melissa, Alisha and Beth are great. They worked so hard to help the graduate students to focus on the research. Last but not least, I would like to thank my wife, Ayikamaer Xiaokaiti, and my family in China. Without their constant love and support over the years, I would not be where I am today.

Acknowledgements reflect the views of the author and are not endorsed by committee members or Oklahoma State University.

Name: LIMU KE

Date of Degree: MAY, 2019

Title of Study: THE DYNAMICS OF CROSS-POLARIZATION COUPLING IN A SINGLE WHISPERING-GALLERY MICRORESONATOR

Major Field: PHOTONICS

Abstract: In this dissertation, we investigate the dynamics of cross-polarization coupling (CPC) in a single whispering-gallery microresonator, both numerically and experimentally, and develop an independent method of estimating the CPC strength. First we introduce the basic properties of whispering-gallery modes (WGMs) in dielectric microresonators. Using WGM microresonators, we can observe classical analogs of the electromagnetically induced transparency (EIT) effects, both in coupled resonators and in a single resonator. Next, we focus on cross-polarization coupling (CPC) in a single microresonator. We analyze the dynamics of CPC using a ring cavity model and propose an independent way of estimating the CPC strength, which was previously found by fitting the experimental data to a computer model. Finally, we show experimental results of CMIT and ATS where the values of CPC strength are found by model fitting and by amplitude modulation. Then we compare the two values. Although we get both agreements and disagreements between the two methods, the results indicate that we have developed an independent method of estimating the CPC strength. We need to keep working and make full use of this independent way of estimating the coupling strength for optical signal processing and sensor applications of microresonators. We also need to identify the limitations of our new method.

TABLE OF CONTENTS

Chapter Page

I. INTRODUCTION 1

1.1. Whispering-Gallery Modes 1
1.2. Dissertation organization 6

II. INDUCED TRANSPARENCY AND INDUCED ABSORPTION 8

2.1. Electromagnetically Induced Transparency (IT) and Absorption (IA) 8
2.2. IT/IA in Coupled Resonators 11
2.3. IT/IA in a Single Resonator 12

III. CROSS-POLARIZATION COUPLING 14

3.1. Cross-Polarization Coupling (CPC) Effect 14
3.2. Coupled-Mode Induced Transparency (CMIT) and Coupled-Mode Induced Attenuation (CMIA) 17
3.3. Hollow-Bottle Microresonators for CMIT/CMIA 19

IV. DYNAMICS OF CPC 23

4.1. Ring Cavity Model 23
4.2. Analytical Analysis of CPC Dynamics 25
4.3. Numerical Analysis of CPC Dynamics 30
4.3.1. CMIT/CMIA with Gaussian Pulse Response 31
4.3.2. Response to Sinusoidal Input Modulation 34

V. EXPERIMENTAL RESULTS 53

5.1. Experimental Setup 53
5.2. Experimental Procedures 59
5.3. Results and Discussion 73

Chapter Page

VI. CONCLUSION.....104

6.1. Summary.....104
6.2. Future work.....105

REFERENCES 106

LIST OF TABLES

Table Page

1. Calculated values of Ω_{min}^2 for a range of T_s for CMIT 50

2. Calculated values of Ω_{min}^2 for a range of T_s for ATS 51

3. Comparing the values of T_s from numerical fitting and from amplitude modulation 101

LIST OF FIGURES

Figure Page

1.1. Ray diagram (a) and field distribution (b) of WGMs at the equatorial plane of a microresonator....2

1.2. The radial field distribution of a fundamental WGM showing the evanescent fraction....3

1.3. Fiber coupling for a microsphere....4

1.4. Lorentzian dips corresponding to WGMs excited in a microresonator....5

2.1. Energy-level structure of a Λ-type three-level system driven by a coherent coupling field....9

2.2. Relative absorption as a function of detuning of probe frequency from atomic resonance frequency....10

2.3. Dispersion as a function of detuning of probe frequency from atomic resonance frequency....10

3.1. Representation of the WGM structure for two different possible polarizations with respect to the resonator surface, TE or TM....15

3.2. A direct observation of the CPC effect....16

3.3. An HBR obtained by manual compression of air inside the capillary....20

3.4. Radial mode profile for TE polarization in an HBR....21

4.1. Ring cavity model consists of four mirrors....24

4.2. CMIT (CPC). Top to bottom: throughput power spectrum, dispersion, pulse response - input Gaussian pulse in black and delayed throughput pulse in blue....32

Figure Page

4.3. CMIA (CPC). Top to bottom: throughput power spectrum, dispersion, pulse response - input Gaussian pulse in black and delayed throughput pulse in blue 33

4.4. Illustration of frequency sidebands 34

4.5. For the case of same Q: (a) mode splitting in the throughput spectrum; (b) throughput power (blue curve) and input power (black curve) as a function of time for a sinusoidal modulation 36

4.6. For the case of same Q: throughput amplitude (a) and phase (b) with respect to input as a function of modulation frequency 38

4.7. For CMIT: (a) throughput spectrum; (b) throughput power (blue curve) and input power (black curve) as a function of time for a sinusoidal modulation 40

4.8. For CMIA: (a) throughput spectrum; (b) throughput power (blue curve) and input power (black curve) as a function of time for a sinusoidal modulation 41

4.9. For ATS: (a) mode splitting in the throughput spectrum; (b) throughput power (blue curve) and input power (black curve) as a function of time for a sinusoidal modulation 42

4.10. For CMIT: throughput amplitude (a) and phase (b) with respect to input as a function of modulation frequency 44

4.11. For CMIA: throughput amplitude (a) and phase (b) with respect to input as a function of modulation frequency 45

4.12. For ATS: throughput amplitude (a) and phase (b) with respect to input as a function of modulation frequency 46

4.13. Near proportional dependence of T_s on Ω_{min}^2 for CMIT 50

4.14. Near proportional dependence of T_s on Ω_{min}^2 for ATS 51

5.1. Experimental setup for studying the CPC dynamics in an HBR 54

5.2. Fiber puller stage for tapering optical fibers 56

Figure Page

5.3. Piezo-controlled strain tuner. The HBR is glued at two points on the PZT for streching 56

5.4. Experimental throughput power spectra (lower, yellow trace)....58

5.5. Throughput spectrum when the input has TE polarization (a) compared to throughput spectrum when the input has arbitrary polarization (b). Blue: TE throughput; yellow: TM throughput....60

5.6. Experimental throughput power spectra in the fast detector channel when the input has TE polarization (upper, blue trace)....62

5.7. Modulation response of the fast detector channel (upper, blue trace) and slow detector (lower, yellow trace)....63

5.8. Coresonant TE and TM modes showing CMIT in (a) and detuned and indicated by arrows in (b) when the input polarization is 45 degrees 65

5.9. Linewidth measurement for TE mode (upper, blue trace)....66

5.10. Dip depth measurement for TE mode (upper, blue trace) 67

5.11. WGM dip depth variation for overcoupled and undercoupled modes....68

5.12. Linewidth measurement for TM mode (lower, yellow trace)....69

5.13. Dip depth measurement for TM mode (lower, yellow trace) 70

5.14. Relative amplitude of the modulated throughput signal in the fast detector channel (upper, blue trace) at a range of different modulation frequencies of the AOM 72

5.15. CMIT/ATS experimental throughput spectrum (top) compared to model throughput spectrum (bottom) 74

5.16. CMIT (TE input) with 220-μm-radius HBR....77

5.17. CMIT (TE input) with 200-μm-radius HBR....78

5.18. CMIT (TE input) with 200-μm-radius HBR....79

5.19. CMIT (TE input) with 180-μm-radius HBR....80

Figure Page

5.20. CMIT (TE input) with 180-μm-radius HBR....81

5.21. CMIT (TE input) with 190-μm-radius HBR....82

5.22. CMIT (TE input) with 180-μm-radius HBR....83

5.23. ATS (TE input) with 180-μm-radius HBR....85

5.24. ATS (TE input) with 180-μm-radius HBR....86

5.25. ATS (TE input) with 180-μm-radius HBR....87

5.26. ATS (TE input) with 180-μm-radius HBR....88

5.27. ATS (TE input) with 190-μm-radius HBR....89

5.28. ATS (TE input) with 190-μm-radius HBR....90

5.29. ATS (TE input) with 180-μm-radius HBR....91

5.30. ATS (TE input) with 200-μm-radius HBR....92

5.31. CMIT (TM input) with 180-μm-radius HBR....94

5.32. ATS (TM input) with 180-μm-radius HBR....96

5.33. ATS (TM input) with 200-μm-radius HBR....97

5.34. ATS (TM input) with 180-μm-radius HBR....98

5.35. ATS (TM input) with 190-μm-radius HBR....99

CHAPTER I

INTRODUCTION

1.1. Whispering-Gallery Modes

In the Temple of Heaven, Beijing, China, there is a circular wall that was built in 1530 during the Ming dynasty. This wall is called “Echo Wall” as two people speaking in small voices on two ends of the wall can hear each other clearly. A similar phenomenon was discovered in the “whispering gallery” of St Paul's Cathedral, London, UK, where Lord Rayleigh first studied whispering-gallery modes (WGMs) of sound waves [1] in 1910.

For optical waves, however, the WGM structure remained a textbook example until 1961, when the first observation of optical WGMs in a spherical sample was reported [2]. WGMs of droplets were also studied in laser action [3, 4] and Raman scattering [5, 6]. But these early works did not initiate immediate scientific interest in WGMs. In 1989, Braginsky, Gorodetsky and Ilchenko showed the high quality (Q) factor of WGMs in a microsphere made by melting the tip of a silica fiber [7]. This effective and reliable method of fabricating silica microspheres spread out quickly and motivated a huge amount of recent works on optical WGMs. WGM microresonators, like microspheres, microdisks, microtoroids, microcylinders, microrings and hollow-bottle microresonators (HBRs), are characterized by having ultrahigh-Q factors and small optical-mode volumes [8], thereby making them advantageous for studies in areas such as cavity quantum

electrodynamics (QED), nonlinear optics, optomechanics, and high-sensitivity sensing.

A WGM is essentially the limiting case of propagation, by total internal reflection, around the greatest circumference of the microresonator (Fig. 1.1). As the number of internal reflections becomes very large the circumference equals an integral number of wavelengths of the light.

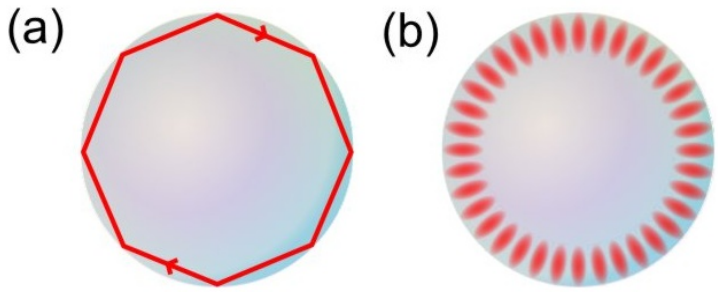

Figure 1.1. Ray diagram (a) and field distribution (b) of WGMs at the equatorial plane of a microresonator [9].

The WGM fields of a microsphere (actually, spheroid) or HBR are described in terms of Bessel functions and harmonic oscillator wave functions. Three numbers, *m*, *p*, and *q*, characterize a WGM: the mode number *m* is the number of wavelengths around the circumference, the mode order *p* is the number of radial maxima of the mode's intensity distribution, and *q* gives the number of latitudinal (sphere) or axial (HBR) field nodes. In addition, two different polarizations are possible for WGMs: transverse electric (TE) polarization and transverse magnetic (TM) polarization. The polarization dependence of the total-internal-reflection phase shift causes the effective refractive index to depend on polarization, so TE and TM modes with the same *m*, *p*, and *q* have different frequencies. In order to completely characterize a WGM inside a microresonator, we need to know all 4 indices: the mode numbers *m*, *p*, *q* and polarization (TE/TM). A "fundamental" mode has $p = 1$ and $q = 0$, giving one transverse maximum.

In a WGM, a portion of the mode is evanescent, extending a small distance outside the microresonator, and decaying approximately exponentially with distance from the surface (Fig. 1.2). This feature allows "whispering", or weak coupling, of light into a microresonator without sacrificing the low-loss and high confinement nature of the WGMs. It also allows the light to interact with matter on or near the resonator's surface and enables numerous sensing applications.

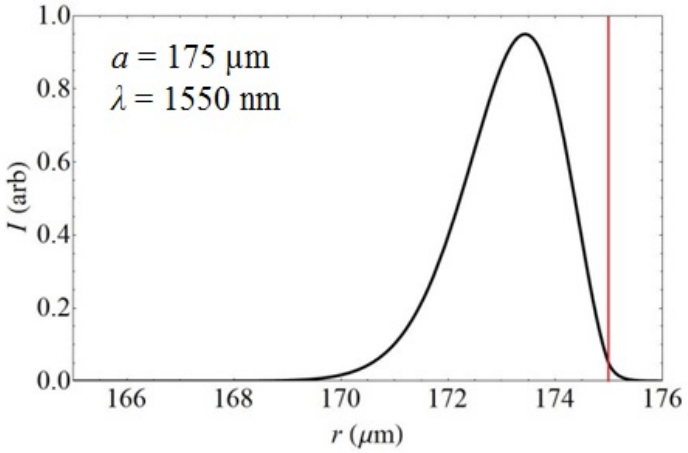

Figure 1.2. The radial field distribution of a fundamental WGM showing the evanescent fraction. (Here radius a = 175 μm, wavelength λ = 1550 nm and the resonator's surface is indicated in red).

There are two main methods for coupling of light into and out of the WGMs of a microresonator. The first method is prism coupling, in which the resonator is placed in contact with a prism while a tunable laser is focused to a small spot size at the prism-resonator interface at an angle greater than the critical angle [10]. Due to total internal reflection, an evanescent field is produced and allows the laser to couple from the prism surface into the resonator. At the same time, the resonator's evanescent field allows the light to couple back into the prism. This old method is effective but it is also very difficult experimentally. So prism coupling is rarely used in current research.

The second method is fiber coupling (Fig. 1.3), which is easier and more commonly used nowadays. In this method, an optical fiber is tapered to a diameter of a few microns and brought into contact with the resonator in its equatorial plane while light from a tunable laser is injected into one end of the fiber. When the light is propagating in the untapered region of the fiber it is confined within the core due to total internal reflection between the core and the cladding. As the light propagates into the tapered region it transforms from core-cladding guidance to cladding-air guidance, producing an external evanescent field which couples into the resonator. Likewise, the resonator's evanescent field allows the light to couple back into the fiber.

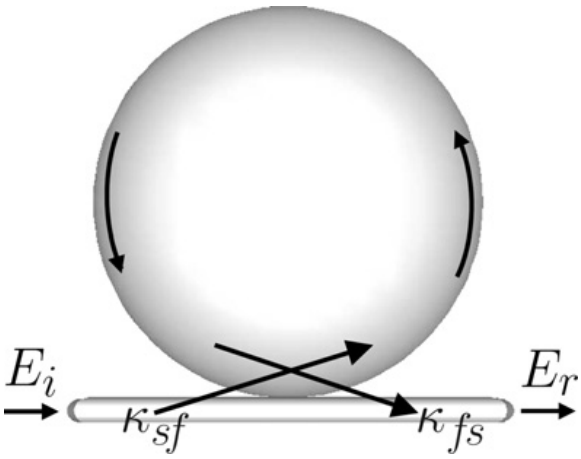

Figure 1.3. Fiber coupling for a microsphere.
E_i and E_r indicate the input field and throughput field. κ_{sf} and κ_{fs} refer to the coupling coefficients between the fiber (f) and microsphere (s) modes [11]. At the coupling point, the fiber is tapered to a diameter of a few microns (not shown).

After the tapered region, the light propagation changes back to core-cladding guidance and the throughput power is detected at the other end of the fiber. Tapered fiber coupling excites WGMs of the microresonator by optical tunneling of photons from the fiber to the resonator. The throughput spectrum

that is detected will display a resonance dip for each WGM excited (Fig. 1.4). The resonance dips take the structure of the Lorentzian profile, which is the Fourier transform of the exponential decay [12].

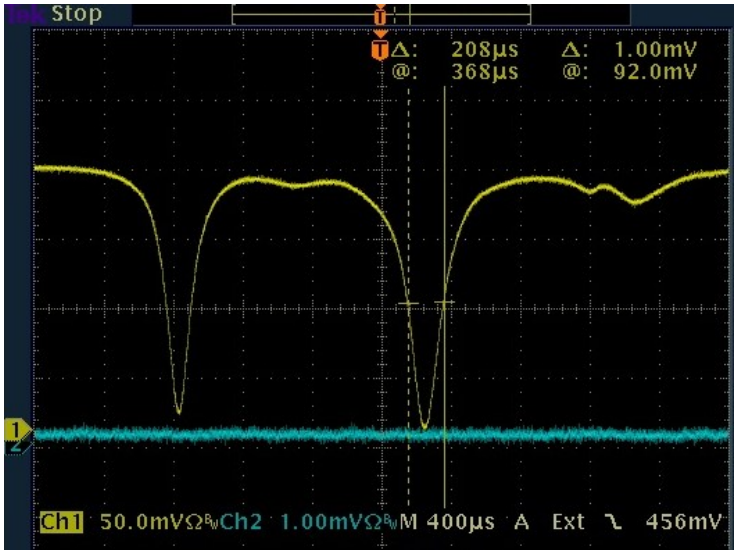

Figure 1.4. Lorentzian dips (yellow trace) corresponding to WGMs excited in a microresonator. The slight asymmetry visible is caused by weak overlapping of nearby modes.

For each dip, two parameters can be measured: mode linewidth and mode dip depth. The mode linewidth is proportional to the total loss, which includes radiation loss, absorption loss, surface scattering loss and coupling loss. The radiation, absorption, surface scattering loss are intrinsic loss while the coupling loss is extrinsic loss. The mode dip depth depends on the ratio of the coupling loss to intrinsic loss. The extremely loss-low nature of the WGMs usually results in very sharp dips, or modes with narrow linewidths.

The mode quality factor Q is closely related to the linewidth as: $Q = \nu/\Delta\nu = \omega\tau$, where $\nu = \omega/2\pi$ is the light frequency, $\Delta\nu$ is the WGM linewidth, and τ is the photon lifetime in the mode. High Q means, in

addition to narrow linewidth, that the light makes many intracavity round trips (longer photon lifetime). These two attributes are responsible for the sensitivity of the microresonator's response to changes in temperature, ambient absorption coefficient, and ambient index of refraction, and make it well suited for use as a sensor.

For chemical and biosensing purposes, we can measure the frequency shift of a WGM caused by the analyte's perturbation of the ambient's index of refraction [13, 14]. In addition, analyte absorption will change the effective intrinsic loss and *Q* of the WGM, and the modification of dip depth [15, 16] or mode linewidth [17] can be measured. As mechanical sensors, WGM microresonators can be used to measure strain, acceleration, and rotation. Their sensitivity to thermal effects has been noted and used to completely characterize microresonator losses [18].

1.2. Dissertation Organization

In this dissertation, we focus on another important application of the WGM microresonators: achieving electromagnetically induced transparency (EIT) -like effects to enable use of the resultant effects such as slow light for optical information processing. More specifically, we will investigate the dynamics of cross-polarization coupling (CPC), which is one way of achieving EIT-like effects in a single resonator.

In Chapter II, we give some background information about EIT effects. We also talk briefly about achieving EIT-like effects in coupled resonators, namely coupled resonator induced transparency (CRIT) or coupled resonator induced attenuation (CRIA). Then we look at different ways of achieving EIT-like effects in a single resonator, one of which involves cross coupling between orthogonally polarized light resulting in coupled mode induced transparency (CMIT) or coupled mode induced attenuation (CMIA).

In Chapter III, we emphasize the importance of polarization analysis and explain the nature of the CPC effect. We also introduce the hollow-bottle microresonator (HBR), which is the ideal resonator for our experiment because of several advantages over other types of resonators.

In Chapter IV, we analyze the dynamics of CPC using a ring cavity model. From our dynamical analysis, we propose an independent way of estimating the CPC strength by input amplitude modulation, rather than finding it by model fitting.

In Chapter V, we first describe our experimental setup and experimental procedures. Then we show results of estimating the CPC strength for different cases. We compare the CPC strength obtained by amplitude modulation to the value inferred from model fitting. Our experimental results confirm that we have developed an independent method of estimating the CPC strength.

In Chapter VI, we summarize the thesis and give an outlook for the future work.

CHAPTER II

INDUCED TRANSPARENCY AND INDUCED ABSORPTION

2.1. Electromagnetically Induced Transparency (IT) and Absorption (IA)

Since the invention of the laser, many new discoveries have been made possible with the help of this highly coherent light source. One of these exciting new phenomena is electromagnetically induced transparency (EIT) effects where laser-induced coherence of atomic states leads to quantum interference between the excitation pathways that control the optical response. This eliminates the absorption [19] at the resonant frequency of a transition, i.e., the coherently driven medium is transparent to the probe field. In 1990, Harris et al. [20] first used the term EIT to describe the cancellation of the linear response by destructive interference in a laser-dressed medium. In 1991, Boller et al. [21] reported the first experimental observation of EIT in Sr vapor. Nowadays EIT effects are used in areas such as ultraslow group velocities, longitudinal pulse compression, storage of light and efficient nonlinear mixing.

The optical properties of atomic and molecular gases are fundamentally tied to their intrinsic energy-level structure. So in order to understand the physics of EIT we need to look in detail at the dynamics in three-level atoms coupled to the applied laser fields and determine the optical response. Fig. 2.1 shows a Λ-type three-level system driven by a coherent coupling field.

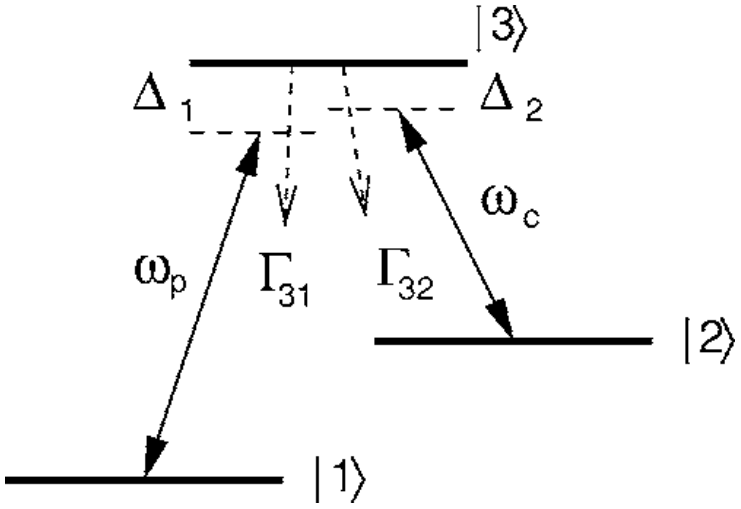

Figure 2.1. Energy-level structure of a Λ-type three-level system driven by a coherent coupling field: ω_p is the frequency of the probe field and ω_c is the frequency of the coupling field; $\Delta_1 = \omega_{31} - \omega_p$ and $\Delta_2 = \omega_{31} - \omega_c$ denote field detunings from atomic resonances; Γ_{ik} are the radiative decay rates from state $|i\rangle$ to state $|k\rangle$.

The probe field is tuned near resonance between two of the states and measures the absorption spectrum of the transition. The coupling field is much stronger and it is tuned near resonance at a different transition. If the states are selected properly, the presence of the coupling field will create a spectral "window" of transparency (Fig. 2.2) which will be detected by the probe. Extreme dispersion is also created (Fig. 2.3) within this transparency "window" which leads to "slow light", i.e. a light pulse passing through the system with group velocity less than the speed of light in the atomic medium.

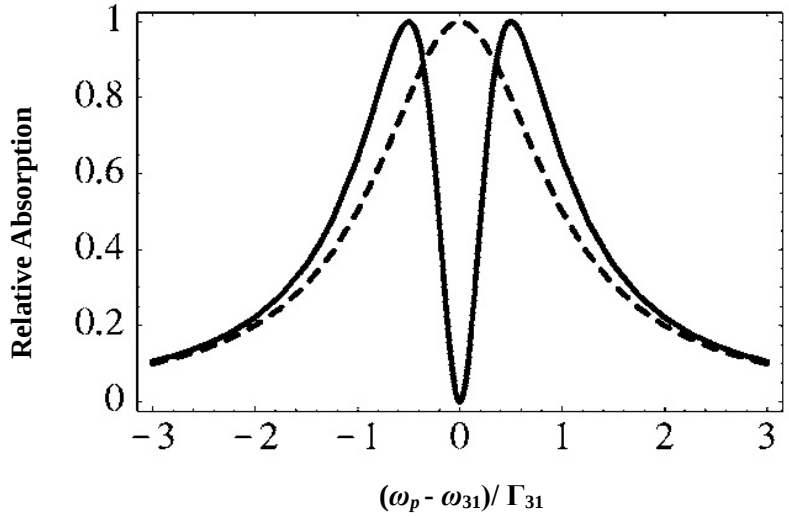

Figure 2.2. Relative absorption as a function of detuning of probe frequency ω_p from atomic resonance frequency ω_{31}, for a system with absorption linewidth $2\Gamma_{31}$ when the coupling field is off (dashed line) and an EIT system when the coupling field is on (solid line).

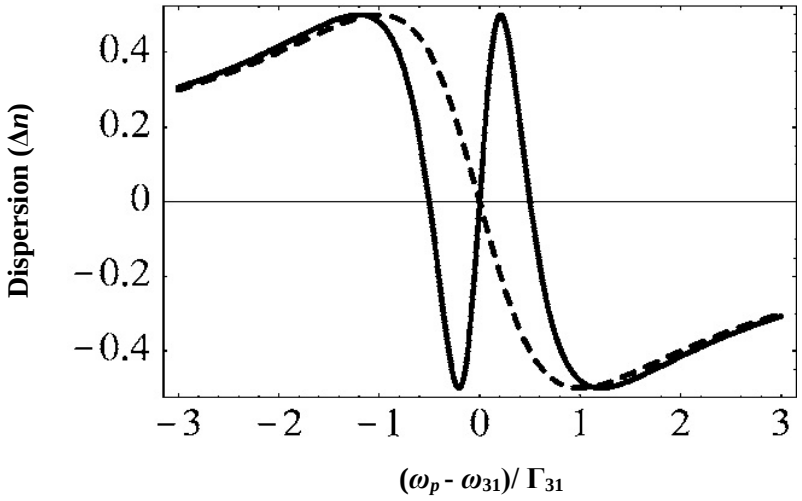

Figure 2.3. Dispersion (or change of refractive index) as a function of detuning of probe frequency ω_p from atomic resonance frequency ω_{31}, for a system with absorption linewidth $2\Gamma_{31}$ when the coupling field is off (dashed line) and an EIT system when the coupling field is on (solid line).

In contrast to EIT, electromagnetically induced absorption (EIA) happens when there is an increase in the absorption coefficient due to the constructive interference between the transfer of population and transfer of coherence between two hyperfine ground and excited states of an atomic system. In this case, the steep negative slope of refractive index vs. frequency (anomalous dispersion) on resonance gives rise to “fast light” [22].

Autler–Townes splitting [23] (ATS) also displays a transparency window (similar to EIT). However, ATS is not the result of interferences [24] but involves field-induced splitting of energy levels.

2.2. IT/IA in Coupled Resonators

Induced transparency is not a quantum phenomenon, but something more universal; e.g., it can be observed in a system of two oscillators with equal natural frequencies but different damping rates that are coupled to each other. Using WGM microresonators, we can also observe classical analogs of the EIT effects in atomic systems. Recent theoretical analysis of coupled microresonators [25] has revealed that coherence effects in the coupled resonator system are remarkably similar to those in atoms. Experimental observation of induced transparency and absorption in coupled microspheres [26] has also been reported.

In the coupled resonator experiment, two spheres are brought nearly into contact by using a precise actuator to control their separation. Due to the evanescent coupling between the coresonant whispering-gallery modes of the two microspheres, the net throughput power in the coupled resonator system has features analogous to the EIT and EIA phenomena [26]. This is accounted for by the destructive or constructive interference between the coresonant WGMs of the two microresonators, which either reduces or enhances light losses in the system, resulting in coupled resonator induced transparency (CRIT) or coupled resonator induced attenuation (CRIA) effects.

The inter-sphere evanescent coupling only occurs between two individual WGMs of the same polarization from two resonators.

2.3. IT/IA in a Single Resonator

Induced transparency can also be observed in a single microresonator. There are three methods for achieving IT/IA in a single resonator.

The first method for achieving induced transparency and attenuation uses cross-polarization coupling (CPC) [27]. Light of one polarization circulating in a WGM of the microresonator can be coupled into a coresonant WGM of the orthogonal polarization. This CPC is likely a result of weak polarization rotation. In this case, the input light and detected throughput is one polarization, say TE. Because of CPC, the interaction with a coresonant TM WGM produces a throughput spectrum (as the driving laser is scanned in frequency) showing cross-polarization coupled-mode induced transparency and attenuation (CMIT, CMIA) [28]. An input pulse whose center frequency is resonant will be delayed or advanced [29, 30].

The second method uses incident light linearly polarized at 45° (for example) in the TE-TM basis to drive coresonant modes of the two polarizations and produce induced transparency or attenuation in the throughput of the same linear polarization as the incident light. This occurs even in the absence of cross-polarization mode coupling, demonstrating that mode superposition is sufficient to produce these effects, including pulse delay or advancement. The effects induced in this manner are referred to as coresonant polarization induced transparency and attenuation (CPIT, CPIA) [31].

For the third method, linearly polarized light is input and excites only TE (or TM) modes; two modes, of like polarization but different radial order, are coresonant and coupled to each other [31-34]. In this case, the coupling between modes is mediated by the input/output coupling fiber – light

circulating in one WGM couples out into the fiber and then immediately back into the other WGM. We use FMIT and FMIA to refer to the fiber-mediated induced transparency and attenuation effects seen using this method.

CHAPTER III

CROSS-POLARIZATION COUPLING

In most of the applications of the WGM of microresonators, typical measurements of the system have been taken without polarization analysis, i.e. the polarization of the light was not carefully controlled, nor was the throughput polarization-analyzed.

3.1. Cross-Polarization Coupling (CPC) Effect

An important feature of a microresonator is the occurrence of transverse electric (TE) and transverse magnetic (TM) mode families that result from the boundary conditions applied to the wave equation. Each mode has its own field configuration and they are polarized orthogonally to each other; TE modes are tangentially polarized while TM modes are radially polarized with respect to the resonator surface (see Fig. 3.1).

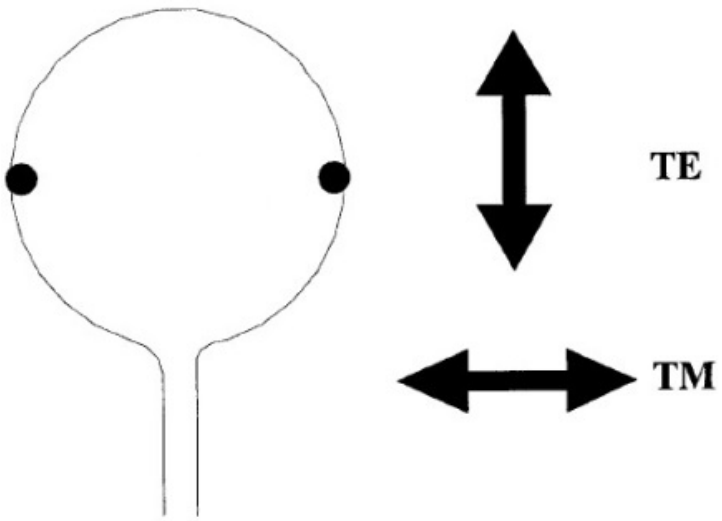

Figure 3.1. Representation of the WGM structure for two different possible polarizations with respect to the resonator surface, TE or TM (indicated by the arrows).

The polarization dependence of the total-internal-reflection phase shift causes the effective refractive index to depend on polarization, so TE and TM modes with the same *m*, *p*, and *q* have different frequencies. In a single microresonator with TE and TM WGMs, we would expect interesting phenomena to happen when TE and TM modes are brought into coresonance.

In an early series of experiments [27] it was observed that when one pumped the cavity using input light scanned through resonance, with linear polarization aligned to one of the cavity's polarizations, peaks of orthogonally polarized light were observed in the throughput (Fig. 3.2).

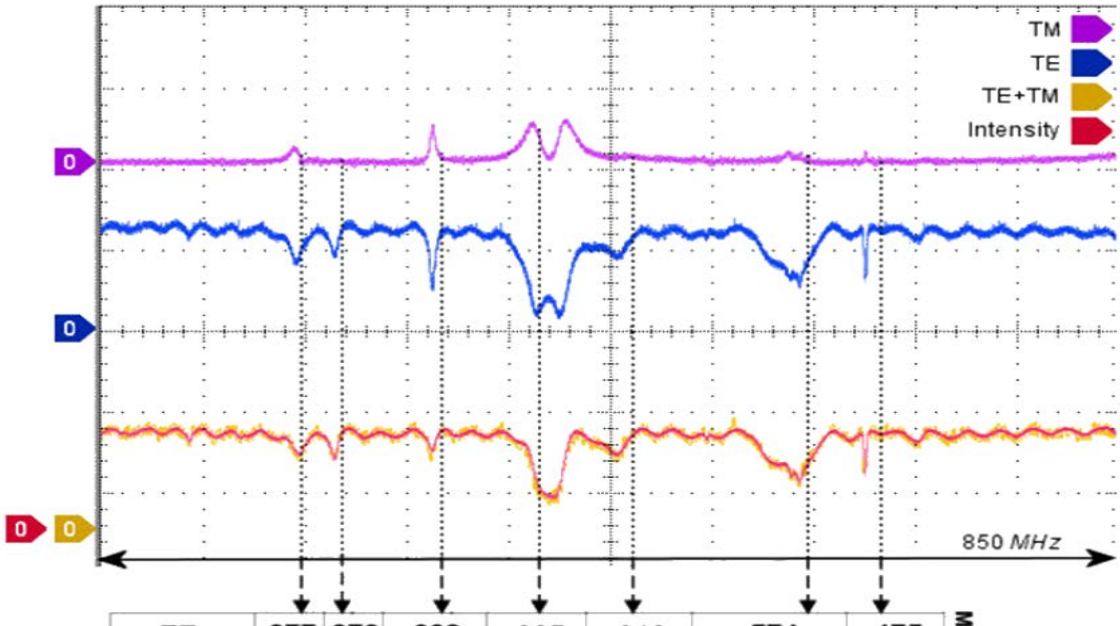

TE	.377	.279	.639	.885	.918	.574	.475
Intensity	.254	.22	.203	.678	.678	.542	.424
TE+TM	.254	.22	.271	.678	.678	.542	.424
Error	.123	.059	.436	.207	.240	.032	.051

Measured Dip Depth

Figure 3.2. A direct observation of the CPC effect. The system is pumped with a pure TE cavity polarization. The resulting TE and TM fiber outputs are summed (yellow trace) and compared to an unpolarized intensity trace (red). The table lists several examples of the respective dip depths [27]

Shown in Fig. 3.2 is a direct observation of the CPC effect and its consequences. The cavity is fiber coupled and pumped with linearly polarized light, TE in the cavity's polarization basis. This CPC effect must be explored rigorously if we are to infer correct information from our experiments. Simultaneous measurements are then made on the system throughput using separate detectors preceded by a polarizing beam splitter, to detect TE and TM separately, as well as another detector with no polarization analysis. The TE and TM output are added, in real time, and compared to the unpolarized detector response. If we don't polarization analyze the throughput, we can just detect the sum of the two orthogonally polarized throughput powers (the superimposed yellow and red traces). If we analyze the throughput, we get the TE polarization (the blue trace), with dips marking the resonant TE WGMs. But, more remarkably, we get the orthogonally polarized throughput TM (the purple trace), which would be zero without the CPC effect, with several peaks demonstrating that CPC is occurring for several of the resonant TE WGMs. The table lists several examples of the respective fractional dip depths and the errors that would be made by measuring the total power only.

The concurrence of the unpolarized power detector response with the direct addition of the orthogonal polarization powers suggests strongly that if the experimental parameters were to be determined without an understanding of the polarization response, the inferred parameters could be in serious error.

3.2. Coupled-Mode Induced Transparency (CMIT) and Induced Attenuation (CMIA)

Coupling between orthogonally polarized WGMs results in mode splitting, and if one mode's Q is much greater than the other's, induced transparency/ attenuation (IT/IA) can be observed. These effects are termed coupled-mode induced transparency (CMIT) and induced attenuation (CMIA)

and they enable slow light or fast light, where a light pulse passing through the system travels slower or faster than the speed of light in silica. These are useful in certain applications such as optical gyroscope sensitivity enhancement, sensing, and fast-light data buffers for telecommunications, so it is desirable to understand the circumstances under which the CPC effect can occur.

The nature of CPC is due to the mode coupling between orthogonally polarized WGMs at resonance. Mode coupling is a feature of many different physical systems. For a system that is composed of a single oscillator, free vibrations occur when the system is displaced initially from its equilibrium configuration and is then allowed to oscillate by itself. Very often, however, the system is damped and set into oscillation by an external driving force that continues to act on the system after t = 0. The frequency of such a forced oscillation is then determined by the frequency of the driving force and not by the resonant frequency [35]. The amplitude of oscillation depends on the detuning of the driving frequency from resonance, and if the driving force is turned off, the amplitude will be reduced gradually because of the damping. However, in the real world, many physics systems involve coupled oscillators, in which oscillators are connected in such a way that energy can be transferred between them. The behavior of each oscillator influences that of the others, which makes the apparent motions of the system very complicated, but it is easier to understand if we resolve the motion into normal modes. A normal mode of a coupled oscillator system is a pattern of motion in which all parts of the system move sinusoidally with the same frequency and with a fixed phase relation. The motion described by the normal modes can take place at frequencies different from the system's natural frequencies. Mode coupling can shift the system's resonant frequencies. Normal modes (or supermodes) are mathematically orthogonal to each other and their superposition gives us the general motion of the system. For example, in a system with two coupled harmonic oscillators, the normal modes are the symmetric mode and the antisymmetric mode, when the two oscillators are in phase and out of phase, respectively. The

extent to which each normal mode is excited is determined by the amplitude of the driving force and the closeness of the driving frequency to the resonant frequency of the mode.

CPC is a manifestation of mode coupling in optical resonators. Light circulating in one polarization is coupled into the other by polarization rotation caused by slight asymmetry in the microresonator profile which enables an optical spin-orbit interaction [36]. For the coupling between orthogonally polarized WGMs to be easily observable, TE-TM coresonance is required. Because when one polarization, TE for example, is directly excited, there is always some nonzero power in the orthogonal TM polarization due to CPC. But only when TM is coresonant with TE, the power in the TM modes can build up to an experimentally observable value. As we will discuss below, the hollow-bottle microresonator (HBR) is a near-ideal system in which to study these effects.

3.3. Hollow-Bottle Microresonators for CMIT/CMIA

We use a hollow-bottle microresonator [37] (HBR), instead of a silica microsphere, in our experiments. Due to its bottle shape, the HBR has some advantages over the microsphere for controlling the cross polarization coupling. Bottle resonators provide the benefits of high *Q*, tunability (by stretching), axial mode confinement, and mode selectivity (by positioning the coupling fiber). The WGMs of an HBR can be tuned easily by stretching the resonator, and the two polarizations tune at different rates, so coresonance can be imposed (rather than achieving it by coincidence). So it is easier to see CPC effects and study the resultant CMIT/CMIA with the help of HBRs.

To make the HBR, a fused-silica capillary is internally etched with a hydrofluoric acid solution to thin its walls to a thickness of 5-10 μm, and then a short length is heated using a hydrogen torch

while under internal air pressure, leading to the formation of a bottle-shaped bulge [37]. A typical HBR made in our lab is shown in Fig. 3.3.

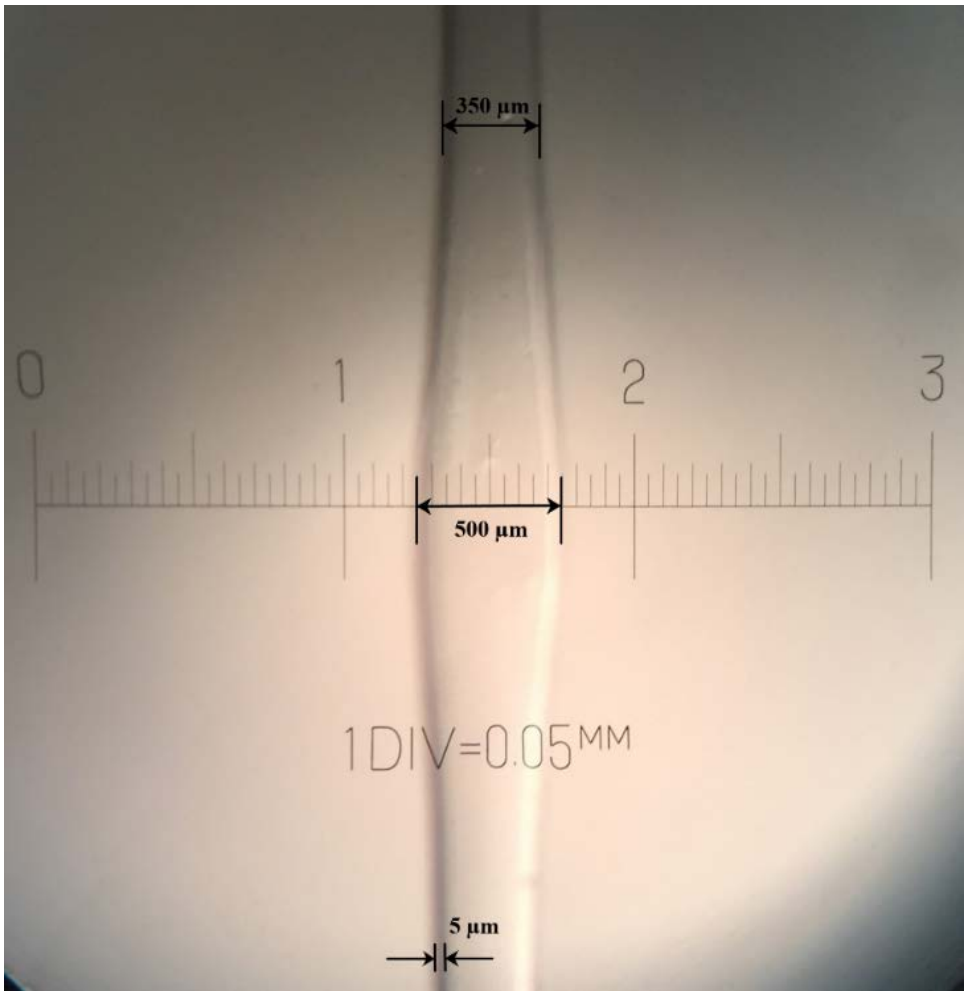

Figure 3.3. A hollow bottle resonator (HBR) obtained by manual compression of air inside the capillary. Initial diameter of the capillary is about 350 µm and the diameter at the bulge is about 500 µm. The wall thickness is about 5 µm after etching.

As a sensor, the HBR takes advantage of intracavity enhancement (because it is a resonator), and in addition it combines the advantages of capillary-based optical ring resonators (because it is hollow) and whispering-gallery bottle resonators (because of the bottle shape). Capillary-based optical ring resonators are advantageous because they permit internal sensing (see Fig. 3.4), which means that much smaller volumes of analyte are required, and it is easy to incorporate the sensor into microfluidic and/or chromatographic systems. Bottle resonators provide the benefits of high *Q*, tunability (by stretching), axial mode confinement, and mode selectivity (by positioning the coupling fiber).

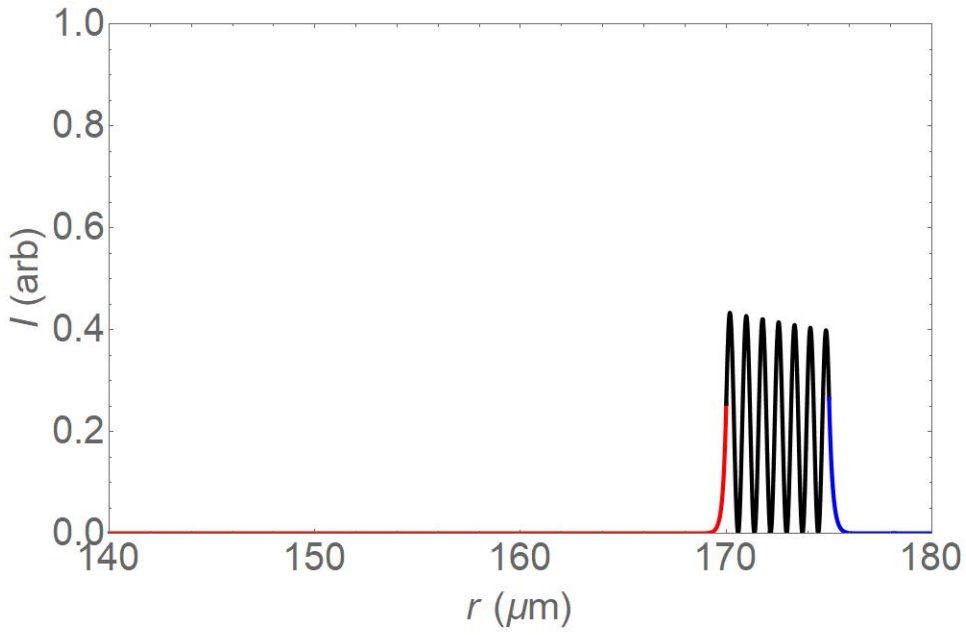

Figure 3.4. Radial mode profile for TE polarization in a HBR with outer radius of 175 μm and inner radius of 170 μm. Both internal (red) and external (blue) evanescent fractions can be used for sensing.

The HBR, then, has all of these positive attributes, and can be used in any application where a capillary-based sensor could, while providing significantly enhanced sensitivity owing to the HBR's one- to two-order-of-magnitude higher *Q*. The HBR is an especially promising platform for sensing and other applications.

CHAPTER IV

DYNAMICS OF CPC

4.1. Ring Cavity Model

To get a physical understanding of the dynamics of CPC and the resultant CMIT/CMIA effects, we can use a ring cavity model as shown in Fig. 4.1. In the model, the CPC between the intracavity circulating TE and TM modes is treated as a cross-polarization rotation near the input/output coupling point. Two input fields (actually, the TE and TM components of a single input field) are injected into the resonator, where they couple to each other. The net reflected fields are analogous to the throughput fields in a whispering-gallery microresonator system. The labeled fields and system parameters are defined and discussed in the following text.

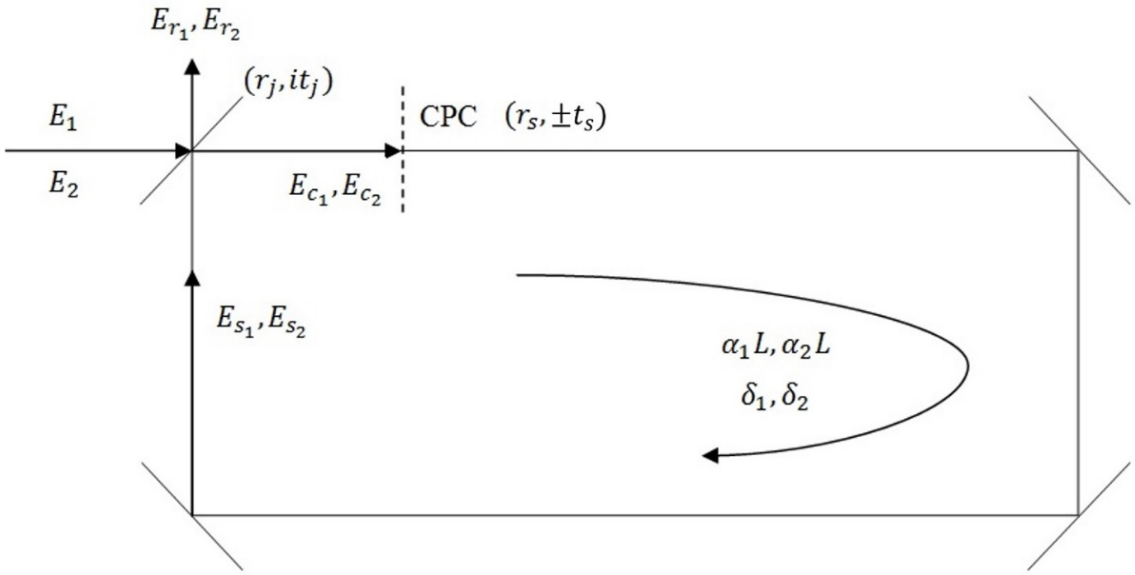

Figure 4.1. Ring cavity model consists of four mirrors: the top left mirror is partially transmitting while all others have 100% reflectivity.

In the model, E_j (j = 1, 2) are orthogonal polarization components of the input field. One of the four mirrors is a partially transmitting mirror with reflection and transmission coefficients r_j and it_j, while the other three mirrors are perfectly reflective. (Because the input and output coupling coefficients, κ_{fs} and κ_{fs} of Fig. 1.3, differ by only about 10% [11], they are both taken to be equal to it_j in this model.) The partial reflector is assumed to be ideal, so that its reflectivity R_j and transmissivity T_j satisfy $R_j + T_j = 1$, where $R_j = r_j^2$ and $T_j = t_j^2$. Immediately after the fields enter the cavity, CPC (modeled here as polarization rotation) takes place with an amplitude of t_s. As the polarization rotates clockwise in the 1-2 basis, we have t_s for E_1 to E_2 coupling and $-t_s$ for E_2 to E_1 coupling. Thus, $T_s = t_s^2 = 1 - r_s^2$ is the cross coupling probability per round trip, and is the measure of intermodal coupling strength. The intracavity fields of the two orthogonally polarized modes

just before and just after the input/output coupler are E_{s_j} and E_{c_j}, respectively. With CPC just after the coupler, we assume round-trip intensity losses of $\alpha_j L$ and round-trip phase shifts δ_j. The E_{r_j} denote the throughput fields, which are given by

$$E_{r_1} = r_1 E_1 + i t_1 E_{s_1} \quad \text{and} \quad E_{r_2} = r_2 E_2 + i t_2 E_{s_2}, \tag{4.1}$$

where, in steady state,

$$\begin{aligned} E_{s_1} &= \left(r_s E_{c_1} - t_s E_{c_2}\right) e^{-\frac{\alpha_1 L}{2}} e^{i\delta_1}, \\ E_{s_2} &= \left(r_s E_{c_2} + t_s E_{c_1}\right) e^{-\frac{\alpha_2 L}{2}} e^{i\delta_2}, \\ E_{c_1} &= i t_1 E_1 + r_1 E_{s_1}, \\ E_{c_2} &= i t_2 E_2 + r_2 E_{s_2}. \end{aligned} \tag{4.2}$$

4.2. Analytical Analysis of CPC Dynamics

We assume that changes in a round trip are small, so that the fields on the right-hand sides of the first two of Eqs. (4.2) are actually one round trip earlier (denoted by primes below) than the left-hand sides, and the steady-state equations can be converted into time-evolution equations by using, for example, $\dot{E}_{s_j} = \dfrac{E_{s_j} - E'_{s_j}}{\tau_{rt_j}}$, where the τ_{rt_j} are the round-trip times in the two modes.

The relation between the coefficients and total (complex) loss rate γ_j for intracavity fields E_{s_j} is given by,

$$\gamma_j = \frac{T_j + \alpha_j L}{2\tau_{rt_j}} - i\frac{\delta_j}{\tau_{rt_j}} + \frac{T_s}{2\tau_{rt_j}} = \kappa_j\left(1 + i\theta_j\right) + \frac{T_s}{2\tau_{rt_j}}, \tag{4.3}$$

with field decay rate is $\kappa_j = (T_j + \alpha_j L)/2\tau_{rt_j} = 1/2\tau_j$, where τ_j is the photon lifetime for mode j; and θ_j is detuning of the resonant frequency of mode j from the input frequency, in units of half the mode linewidth. The cross-polarization coupling to the orthogonal mode comes in as an additional "intrinsic" loss. Note that the quality factor of mode j can be written as $Q_j = \omega_j \tau_j = \omega_j / (2\kappa_j)$, where ω_j is mode j's resonant frequency.

In this way we will get the differential equations for intracavity field amplitudes,

$$\dot{E}_{s_1} = -\gamma_1 E_{s_1} - \frac{t_s}{\tau_{rt_1}} E_{s_2} + \frac{it_1}{\tau_{rt_1}} E_1 - \frac{it_2 t_s}{\tau_{rt_1}} E_2 , \tag{4.4}$$

$$\dot{E}_{s_2} = -\gamma_2 E_{s_2} + \frac{t_s}{\tau_{rt_2}} E_{s_1} + \frac{it_2}{\tau_{rt_2}} E_2 + \frac{it_1 t_s}{\tau_{rt_2}} E_1 . \tag{4.5}$$

These equations have the correct steady-state limit and a form that makes physical sense.

Now using $E_{r_j} = r_j E_j + it_j E_{s_j}$ gives the differential equations for the throughput fields. So the first-order differential equations for throughput fields are

$$\dot{E}_{r_1} = \dot{E}_1 - \gamma_1 (E_{r_1} - r_1 E_1) - \frac{t_s t_1}{t_2 \tau_{rt_1}} (E_{r_2} - r_2 E_2) - \frac{t_1^{\,2}}{\tau_{rt_1}} E_1 + \frac{t_1 t_2 t_s}{\tau_{rt_1}} E_2 , \tag{4.6}$$

$$\dot{E}_{r_2} = \dot{E}_2 - \gamma_2 (E_{r_2} - r_2 E_2) + \frac{t_s t_2}{t_1 \tau_{rt_2}} (E_{r_1} - r_1 E_1) - \frac{t_2^{\,2}}{\tau_{rt_2}} E_2 - \frac{t_1 t_2 t_s}{\tau_{rt_2}} E_1 . \tag{4.7}$$

For the case where the input fields are not assumed to be constant ($\dot{E}_j \neq 0$), the second-order differential equations (throughput) are

$$\ddot{E}_{r_j} = r_j \ddot{E}_j + it_j \ddot{E}_{s_j} . \tag{4.8}$$

We can look at $\ddot{E}_{s_1}$ as an example,

$$\ddot{E}_{s_1} = -\gamma_1 \dot{E}_{s_1} - \frac{t_s}{\tau_{rt_1}} \dot{E}_{s_2} + \frac{it_1}{\tau_{rt_1}} \dot{E}_1 - \frac{it_2 t_s}{\tau_{rt_1}} \dot{E}_2 , \tag{4.9}$$

which, with Eqs. (4.4) and (4.5) gives

$$\ddot{E}_{s_1} + (\gamma_1 + \gamma_2)\dot{E}_{s_1} + \left(\gamma_1\gamma_2 + \frac{T_s}{\tau_{rt_1}\tau_{rt_2}} \right) E_{s_1} = \frac{it_1}{\tau_{rt_1}} \dot{E}_1 - \frac{it_2 t_s}{\tau_{rt_1}} \dot{E}_2 + \frac{it_1\gamma_2}{\tau_{rt_1}} E_1 - \frac{it_2 t_s}{\tau_{rt_1}\tau_{rt_2}} E_2 . \tag{4.10}$$

Then, if we assume the intermodal coupling strength T_s is very small and both modes are driven on resonance ($\theta_j = 0$), so $\gamma_j \approx \kappa_j$, we have:

$$\ddot{E}_{s_1} + (\kappa_1 + \kappa_2)\dot{E}_{s_1} + \left(\kappa_1\kappa_2 + \frac{T_s}{\tau_{rt_1}\tau_{rt_2}} \right) E_{s_1} = \frac{it_1}{\tau_{rt_1}} \dot{E}_1 - \frac{it_2 t_s}{\tau_{rt_1}} \dot{E}_2 + \frac{it_1\kappa_2}{\tau_{rt_1}} E_1 - \frac{it_2 t_s}{\tau_{rt_1}\tau_{rt_2}} E_2, \tag{4.11}$$

which is a general result and has the form of a damped driven oscillator.

In the case of no driving, input fields $E_1 = E_2 = 0$, we can try $E_{s_1} \propto e^{-\beta t}$ in Eq. (4.11) and get:

$$\beta^2 - (\kappa_1 + \kappa_2)\beta + \left(\kappa_1\kappa_2 + \frac{T_s}{\tau_{rt_1}\tau_{rt_2}} \right) = 0 . \tag{4.12}$$

The roots of this equation give us the complex decay constants of the supermodes:

$$\beta_{\pm} = \frac{\kappa_1 + \kappa_2}{2} \pm \sqrt{\left(\frac{\kappa_1 - \kappa_2}{2} \right)^2 - \frac{T_s}{\tau_{rt_1}\tau_{rt_2}}} . \tag{4.13}$$

Then for weak (but non-negligible) intermode coupling: $\frac{T_s}{\tau_{rt_1}\tau_{rt_2}} < \left(\frac{\kappa_1 - \kappa_2}{2} \right)^2$, the radicand is positive and gives two real values for $\beta_{\pm}$, and the destructive interference between the direct and

indirect excitation paths of the intracavity fields produces the induced transparency (CMIT) feature of the throughput power.

In contrast, if the coupling is made strong enough: $\frac{T_s}{\tau_{rt_1}\tau_{rt_2}} > \left(\frac{\kappa_1 - \kappa_2}{2}\right)^2$, the radicand becomes negative and gives two complex values for $\beta_{\pm}$, indicating a frequency splitting. The throughput now is split on both sides from the center of the feature due to the coupling between the intracavity TE and TM modes, and this phenomenon is referred to as Autler-Townes splitting (ATS) [24].

If we look at the case of one component where that component is the only input and might be sinusoidally modulated in amplitude at frequency Ω:

$$E_1 = A_1 e^{-i\Omega t},\ E_2 = 0. \tag{4.14}$$

Trying $E_{s_1} = A_{s_1} e^{-i\Omega t}$ gives

$$-\Omega^2 A_{s_1} - i\Omega A_{s_1}(\kappa_1 + \kappa_2) + \left(\kappa_1\kappa_2 + \frac{T_s}{\tau_{rt_1}\tau_{rt_2}}\right)A_{s_1} = -i\Omega\frac{it_1}{\tau_{rt_1}}A_1 + \frac{it_1\kappa_2}{\tau_{rt_1}}A_1, \tag{4.15}$$

which then gives

$$A_{s_1} = \frac{\left(\Omega + i\kappa_2\right)\frac{t_1}{\tau_{rt_1}}A_1}{{\Omega_0}^2 - \Omega^2 - i\Omega(\kappa_1 + \kappa_2)}, \tag{4.16}$$

where ${\Omega_0}^2 = \kappa_1\kappa_2 + \frac{T_s}{\tau_{rt_1}\tau_{rt_2}}$, and is a measure of the CPC coupling strength.

So now the amplitude of the throughput field is

$$A_{r_1} = r_1 A_1 + i t_1 A_{s_1} = r_1 A_1 + i t_1 \frac{(\Omega + i\kappa_2)\frac{t_1}{\tau_{rt_1}} A_1}{\Omega_0{}^2 - \Omega^2 - i\Omega(\kappa_1 + \kappa_2)}. \tag{4.17}$$

Within the same resonator, the two modes have very nearly the same *n*, so same τ_{rt}; also, r_j can be approximated by 1, so we have:

$$\frac{A_{r_1}}{A_1} = \frac{(\Omega_0{}^2 - \Omega^2) - \frac{T_1\kappa_2}{\tau_{rt}} + i\Omega[\frac{T_1}{\tau_{rt}} - (\kappa_1 + \kappa_2)]}{\Omega_0{}^2 - \Omega^2 - i\Omega(\kappa_1 + \kappa_2)}. \tag{4.18}$$

We can look at the simple case where the two modes have the same *Q*. Then we can drop the 1, 2 subscripts and write:

$$\frac{A_r}{A} = \frac{(\Omega_0{}^2 - \Omega^2) - \frac{T\kappa}{\tau_{rt}} + i\Omega(\frac{T}{\tau_{rt}} - 2\kappa)}{\Omega_0{}^2 - \Omega^2 - i2\kappa\Omega}. \tag{4.19}$$

Let's interpret this result with some typical parameter values. Recall that $\kappa = \frac{1}{2\tau}$; choose $Q = 1.2\times10^8$, $T_s = 2.51\times10^{-8}$, and carrier wavelength $\lambda_c = 1.55$ μm. Then, from $Q = \omega\tau$, we have $\kappa = \frac{1}{2\tau} = \frac{\omega}{2Q} = \frac{\pi c}{\lambda_c Q} = 5.07\times10^6$ s^{-1}, and with radius *a* = 300 μm, *n* = 1.44, we have

$\tau_{rt} = \frac{2\pi a n}{c} = 9.04\times10^{-12}$ s. Then we get the effective resonance frequency of the damped driven oscillator: $\Omega_0 = \sqrt{\kappa^2 + \frac{T_s}{\tau_{rt}{}^2}} = 1.82\times10^7$ s^{-1} (or $\nu_0 = \frac{\Omega_0}{2\pi} = 2.91$ MHz).

Now choose $\Omega = \Omega_0$, then Eq. (4.19) becomes

$$\frac{A_r}{A} = \frac{-\frac{T\kappa}{\tau_{rt}} + i\Omega_0(\frac{T}{\tau_{rt}} - 2\kappa)}{-i2\kappa\Omega_0}. \tag{4.20}$$

Look at the imaginary term in the numerator: it will be small compared to the real term, at least in the limit of strong overcoupling ($T >> \alpha L$). Then $\kappa = \frac{T}{2\tau_{rt}} = \frac{1}{2\tau}$, so we have $T = \frac{\tau_{rt}}{\tau} = 9.17 \times 10^{-5}$.

So $\frac{T}{\tau_{rt}} - 2\kappa = 2\kappa - 2\kappa = 0$, we are only left with the real part $-\frac{T\kappa}{\tau_{rt}} = -5.14 \times 10^{13}\ \mathrm{s}^{-2}$. Thus we have $\frac{A_r}{A} = -i\frac{T}{2\Omega_0\tau_{rt}} \approx -i(0.279)$ and $\left|\frac{A_r}{A}\right|^2 \approx 0.078 = 7.8 \times 10^{-2}$. The -*i* means a 90° phase shift.

We took $E = Ae^{-i\Omega t}$, to represent the physical input $E = A\sin\Omega t$, so the throughput A_r will vary as $-ie^{-i\Omega t} = e^{-i\Omega t}e^{-i\frac{\pi}{2}}$, leading the input by π/2. Measurement of this modulation resonance frequency Ω_0 can be used to determine the intermode coupling strength T_s; however, we will show that there is an even simpler method, without requiring strong over coupling, to use modulation response to determine T_s.

4.3. Numerical Analysis of CPC Dynamics

The ring cavity model described above has been incorporated into a Mathematica program for calculation of CMIT/CMIA behavior (intermode CPC). Depending on what we want to see, the input amplitude can be Gaussian modulated (to see pulse response), sinusoidally modulated (to see throughput modulation amplitude and phase shift), or square-pulse modulated (to see precursors). In the program, typical experimental parameter values are input, and the cross-polarization

coupling strength is treated as an adjustable parameter. The output coupling and intrinsic loss are input indirectly by giving the values of the quality factor Q of each mode (determines total loss), of the depth of each mode's resonance dip (determines ratio of losses), and of the coupling regime (allows determination of each loss independently). The coupling regimes are overcoupled (coupling loss greater), undercoupled (intrinsic loss greater), and critical (losses equal).

4.3.1 CMIT/CMIA with Gaussian Pulse Response

Here, if cw light is input (linearly polarized, only one mode is driven) the program plots the throughput spectrum (relative throughput power as a function of detuning of the input light from coresonance), and the dispersion (phase of the throughput field as a function of detuning). Then it also plots the throughput as a function of time when a resonant Gaussian pulse is input (showing attenuation and delay or advancement).

An example [28] of CMIT is shown in Fig. 4.2. The parameter values are: quality factors $Q_1 = 8 \times 10^6$, $Q_2 = 1.98 \times 10^8$; cross coupling probability $T_s = 5 \times 10^{-8}$; dip depths $M_1 = 0.96$ (overcoupled), $M_2 = 0.93$ (undercoupled). For this CMIT, we see a steep normal dispersion and pulse delay.

An example [28] of CMIA is shown in Fig. 4.3. The parameter values are: quality factors $Q_1 = 8 \times 10^6$, $Q_2 = 1.98 \times 10^8$; cross coupling probability $T_s = 6.3 \times 10^{-9}$; dip depths $M_1 = 0.36$ (overcoupled), $M_2 = 0.53$ (undercoupled). For this CMIA, we see a steep anomalous dispersion and pulse advancement.

In these examples, we assume a large difference in Q values and a typical (relatively low) CPC strength.

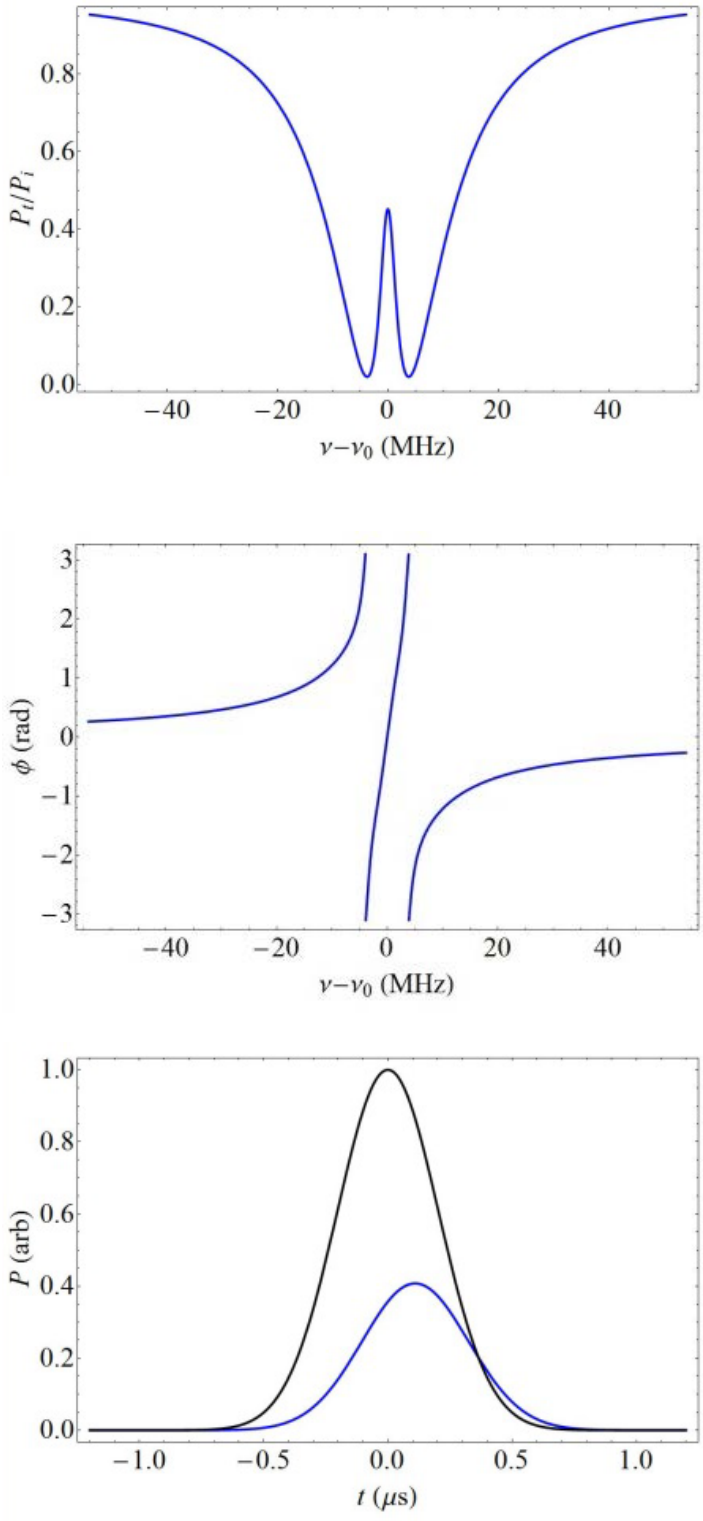

Figure 4.2. CMIT (CPC). Top to bottom: throughput power spectrum, dispersion, pulse response - input Gaussian pulse in black and delayed throughput pulse in blue [28].

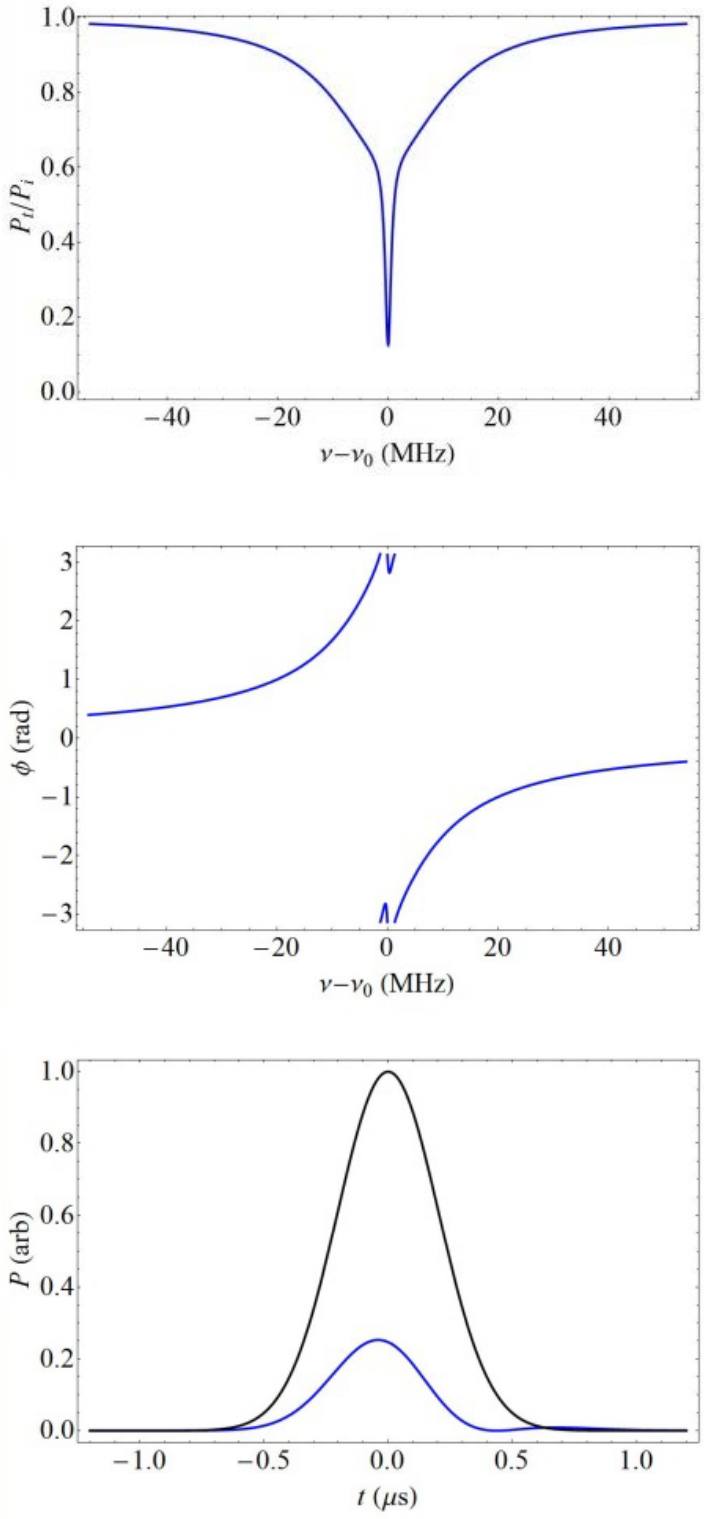

Figure 4.3. CMIA (CPC). Top to bottom: throughput power spectrum, dispersion, pulse response - input Gaussian pulse in black and delayed throughput pulse in blue [28].

4.3.2 Response to Sinusoidal Input Modulation

Now the input amplitude is sinusoidally modulated to see throughput modulation amplitude and phase shift. With sinusoidal input, there will be an obvious phase shift and the amplitude is not just the zero-detuning value of the throughput power. We will see the occurrence of sidebands and the attenuation on the throughput amplitude can be strong or weak depending on the position of the sidebands on the throughput power spectrum.

To analyze the modulation behavior in terms of the frequency sidebands, we can add "carrier detuning" as another adjustable parameter to the program. If the optical carrier frequency is ω, the modulated input is

$$E = A\sin\Omega t\sin\omega t = \frac{1}{2}A[\cos(\omega-\Omega)t - \cos(\omega+\Omega)t]\,. \tag{4.21}$$

So the input frequency spectrum looks like Fig. 4.4:

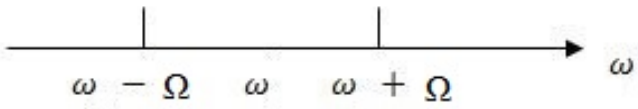

Figure 4.4. Illustration of frequency sidebands for an optical carrier frequency of ω.

The beat at 2Ω describes the intensity: $\sin^2 \Omega t = \frac{1}{2}[1 - \cos 2\Omega t]$. The carrier frequency is resonant with the coresonant WGMs, so the sidebands are symmetrically displaced into regions of smaller throughput power in the case of CMIT when the modulation frequency is not too large.

Let's first choose the same parameter values as in the example in the analytical analysis: both modes have high quality factors $Q_1 = Q_2 = 1.2 \times 10^8$; cross coupling probability $T_s = 2.5 \times 10^{-8}$; dip depths $M_1 = 0.05$ (overcoupled), $M_2 = 0.05$ (overcoupled); in the example, we get $\nu_0 = 2.91$ MHz and choose to modulate at the resonant frequency, so we set the value for $\Omega = 2\pi \times (2.91 \text{ MHz})$.

With the same cw light input (linearly polarized, only one mode is driven) the program again plots the throughput spectrum, the dispersion, and the throughput as a function of time for a sinusoidally modulated input. (The dispersion is not shown in the figures that follow.)

We can see from Fig. 4.5 that mode splitting occurs rather than induced transparency, because $\kappa_1 = \kappa_2$ in this case and Eq. (4.13) gives frequency splitting. We also note that the throughput field is indeed leading the input field by $\pi/2$, making the throughput power appear to be leading by π. Also, the throughput power is consistent with the analytical prediction that it should be about 7.8% of the input power. This confirms our analytical results in the previous chapter.

In the case of same Q, comparing the throughput spectrum in Fig. 4.5(a) to the modulated throughput in Fig. 4.5(b) shows us that the throughput at the sidebands ($\pm$ 2.91 MHz) has the same amplitude as the modulated throughput.

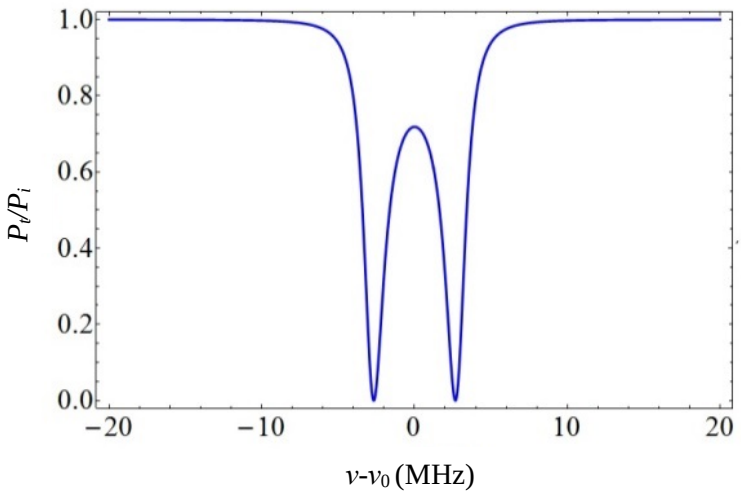

(a)

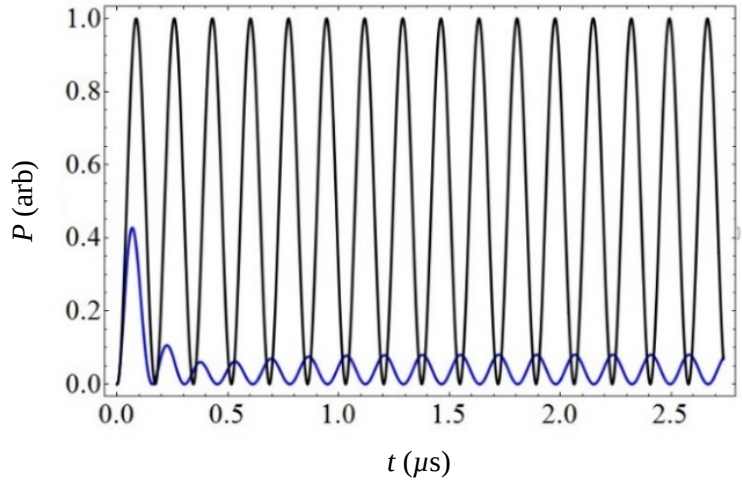

(b)

Figure 4.5. For the case of same Q: (a) mode splitting in the throughput spectrum; (b) throughput power (blue curve) and input power (black curve) as a function of time for a sinusoidal modulation.

From Eq. (4.19) we can plot $\left|\frac{A_r}{A}\right|^2$ vs Ω in the range of ($\frac{\Omega_0}{2}$, $2\Omega_0$) as in Fig. 4.6(a); we can also plot $2Arg(\frac{A_r}{A})$ vs Ω in the same range, as in Fig. 4.6(b). For our case of same *Q* values, the resonance frequency is calculated to be $\Omega_0 = 1.82 \times 10^7$ s^{-1} (or $\nu_0 = 2.91$ MHz). On resonance ($\Omega = \Omega_0$), we can estimate from Fig. 4.6(a) that the amplitude at the modulation frequency of $\Omega = 1.82 \times 10^7$ s^{-1} is around 0.08. In our analytical analysis, the throughput power is about 7.8% of the input power. This confirms that our amplitude plot is consistent with our model. Now let's look at our phase plot of Fig. 4.6(b). At the modulation frequency of $\Omega = 1.82 \times 10^7$ s^{-1} the phase shift is about -3.1, which is almost equal to $-\pi$, meaning the throughput power is leading the input by π. This confirms that our phase plot is also consistent with our model. We may be able to generalize these plotting methods to other cases.

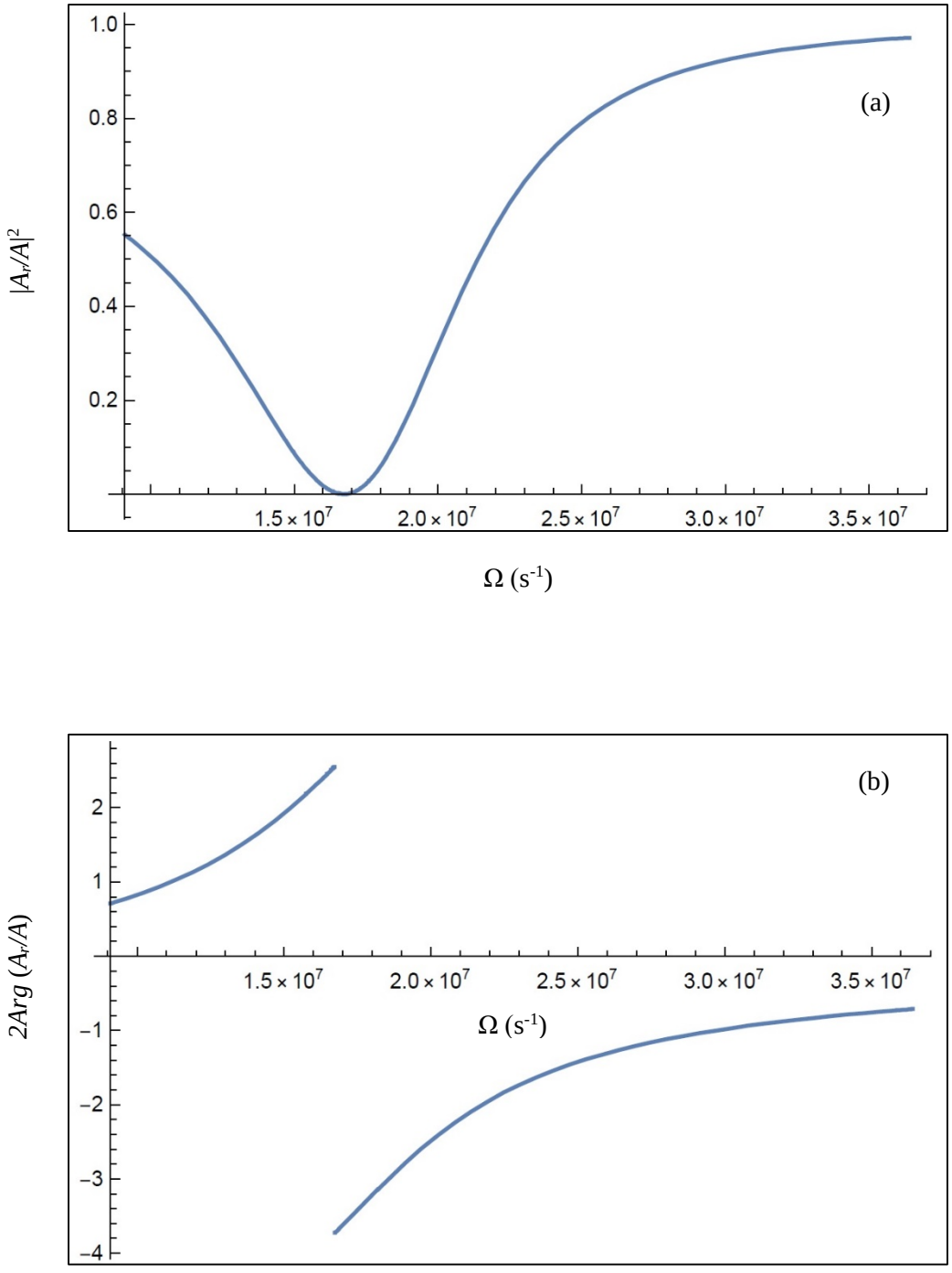

Figure 4.6. For the case of same *Q*: throughput amplitude (a) and phase (b) with respect to input as a function of modulation frequency.

Now let's look at some cases where the Q values are very different. We can take the case of CMIT as in Fig. 4.2, the case of CMIA as in Fig. 4.3 and another case of ATS with the same parameters as our CMIT but with larger T_s.

As given in [28], the parameter values are: for CMIT, quality factors $Q_1 = 8 \times 10^6, Q_2 = 1.98 \times 10^8$; cross coupling probability $T_s = 5 \times 10^{-8}$; dip depths $M_1 = 0.96$ (overcoupled), $M_2 = 0.93$ (undercoupled); for CMIA, the parameters are the same as for CMIT except for these: $M_1 = 0.36$, $M_2 = 0.53$, $T_s = 6.3 \times 10^{-9}$; for ATS, same parameters as CMIT but $T_s = 10^{-6}$. We can zoom in on the CMIT/CMIA and ATS throughput spectra by decreasing the plotting range to check the throughput power at the sidebands. With the given parameter values above, the throughput spectrum looks like Fig. 4.7(a) for CMIT, Fig. 4.8(a) for CMIA, and Fig. 4.9(a) for ATS.

Using these parameter values and the definition of the modulation resonance frequency, $\Omega_0^{\,2} = \kappa_1\kappa_2 + \dfrac{T_s}{\tau_{rt_1}\tau_{rt_2}}$, we can calculate for each case: $\Omega_0 = 2.907 \times 10^7 s^{-1}$ (or $\nu_0 = 4.63$ MHz) for CMIT, $\Omega_0 = 1.76 \times 10^7 s^{-1}$ (or $\nu_0 = 2.8$ MHz) for CMIA and $\Omega_0 = 1.115 \times 10^8 s^{-1}$ (or $\nu_0 = 17.7$ MHz) for ATS.

For the sinusoidally modulated input, on resonance ($\Omega = \Omega_0$), the modulation response looks like Fig. 4.7(b) for CMIT, Fig. 4.8(b) for CMIA, and Fig. 4.9 (b)for ATS. In each case, the throughput seen in Figs. 4.7(a), 4.8(a), and 4.9(a) at the sidebands (± 4.63 MHz for CMIT, ±2.8 MHz for CMIA and ±17.7 MHz for ATS) has the same amplitude as the modulated throughput seen in the (b) plots of the same figure (0.04 for CMIT, 0.658 for CMIA and 0.01 for ATS), respectively.

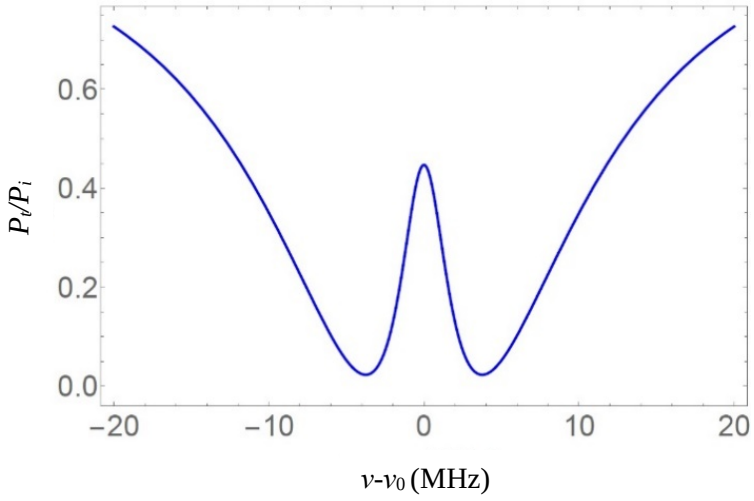

(a)

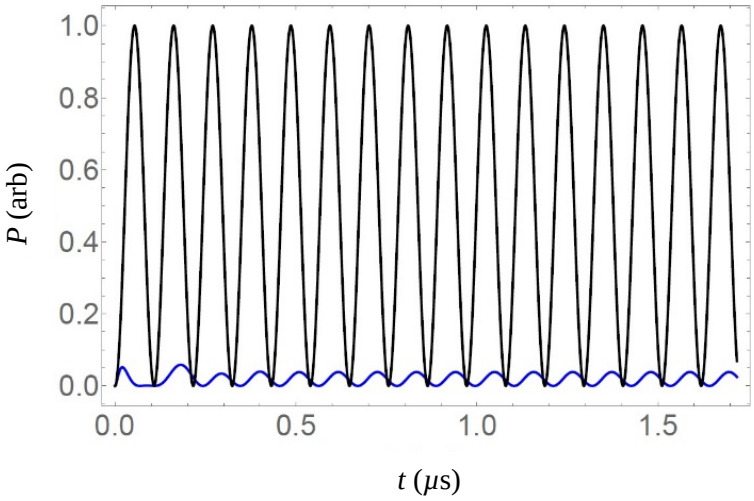

(b)

Figure 4.7. For CMIT: (a) throughput spectrum; (b) throughput power (blue curve) and input power (black curve) as a function of time for a sinusoidal modulation.

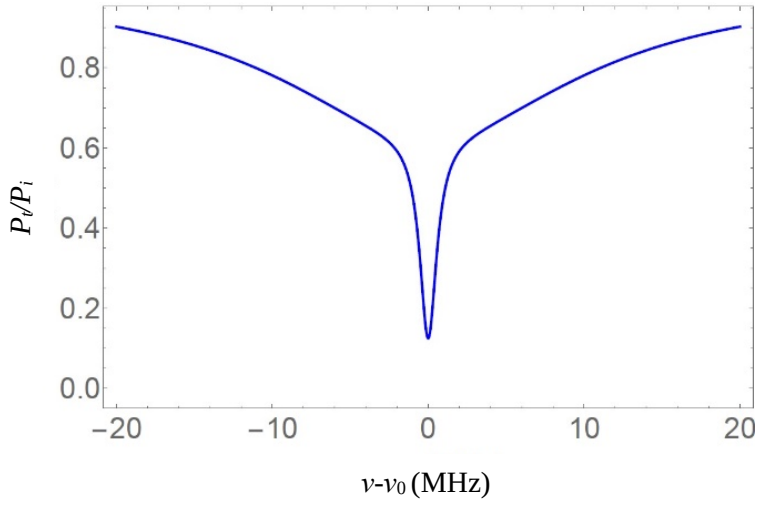

(a)

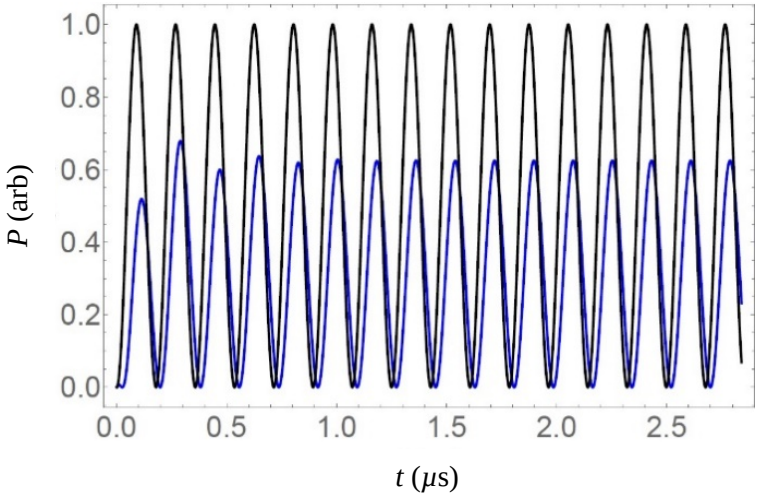

(b)

Figure 4.8. For CMIA: (a) throughput spectrum; (b) throughput power (blue curve) and input power (black curve) as a function of time for a sinusoidal modulation.

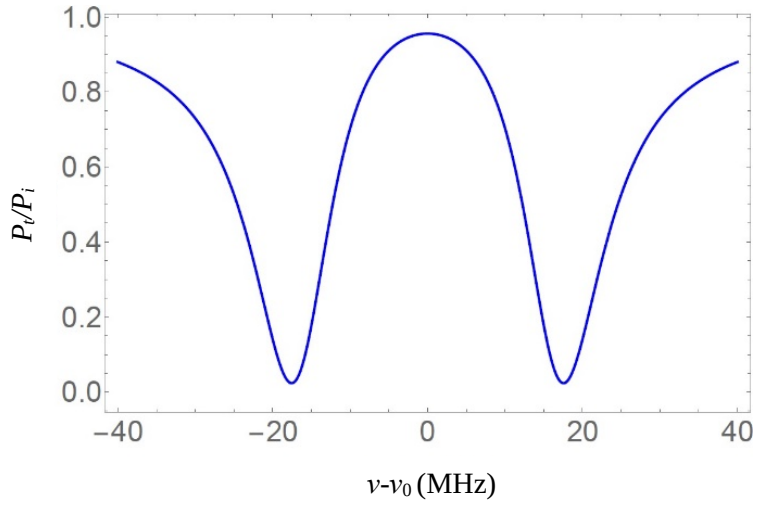

(a)

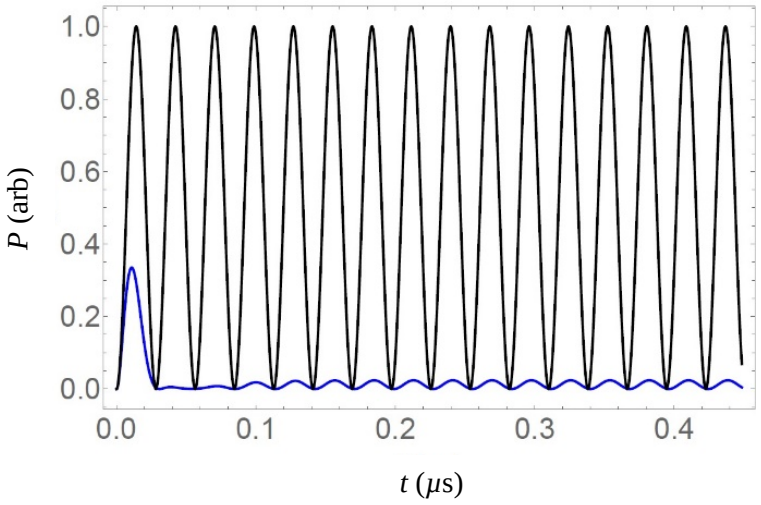

(b)

Figure 4.9. For ATS: (a) throughput spectrum; (b) throughput power (blue curve) and input power (black curve) as a function of time for a sinusoidal modulation.

For the case of same *Q* values, we plotted the amplitude and phase of the throughput with respect to the input using the simplified Eq. (4.19). Now for the cases of different *Q* values, we can use the general Eq. (4.18) to plot $\left|\frac{A_{r_1}}{A_1}\right|^2$ vs Ω in the range of $(\frac{\Omega_0}{2}, 2\Omega_0)$, as in Fig. 4.10(a) for CMIT, Fig. 4.11(a) for CMIA, and Fig. 4.12(a) for ATS; we can also plot $2Arg(\frac{A_{r_1}}{A_1})$ vs Ω in the same range, as in Fig. 4.10(b) for CMIT, Fig. 4.11(b) for CMIA, and Fig. 4.12(b) for ATS.

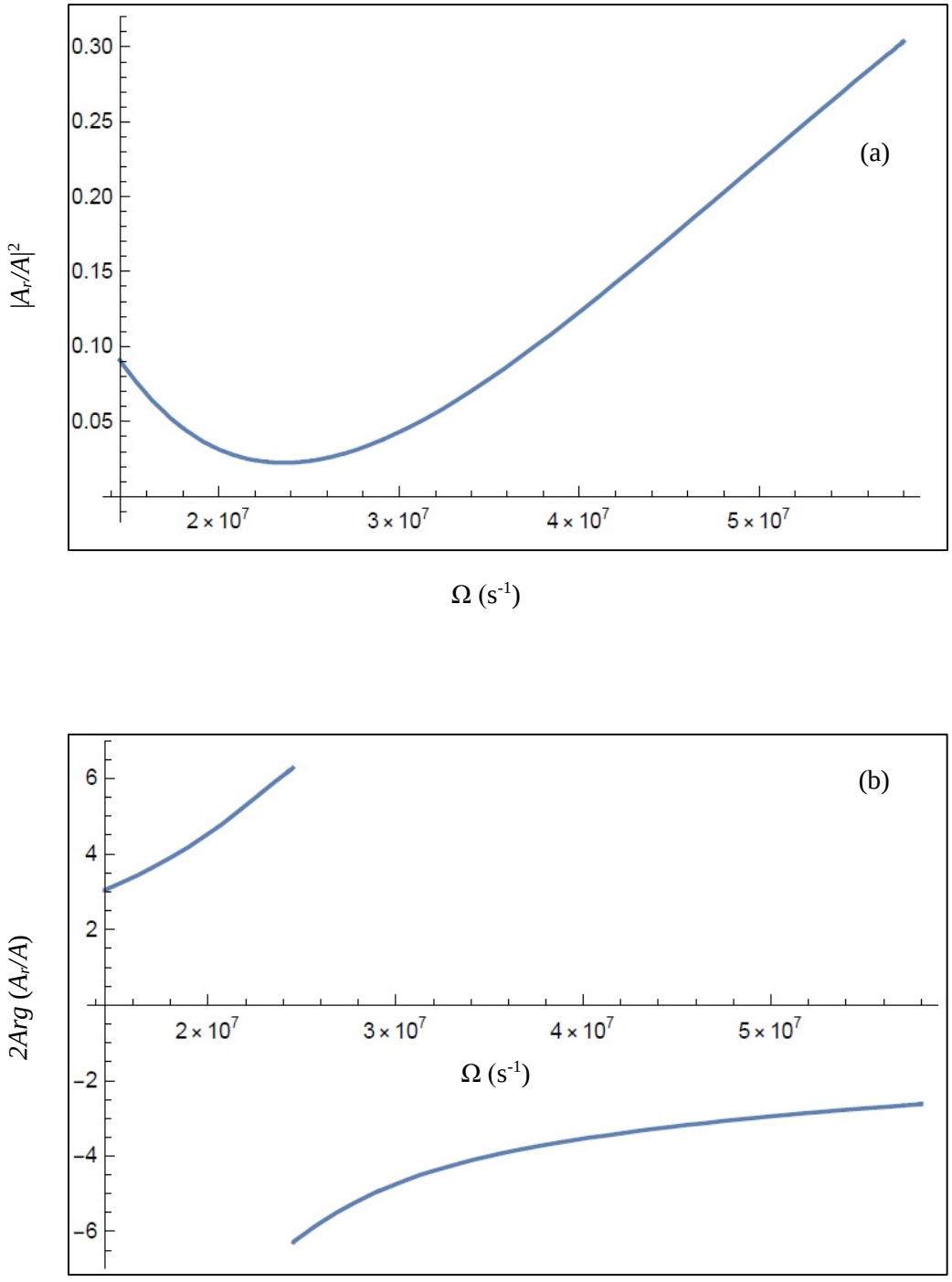

Figure 4.10. For CMIT: throughput amplitude (a) and phase (b) with respect to input as a function of modulation frequency.

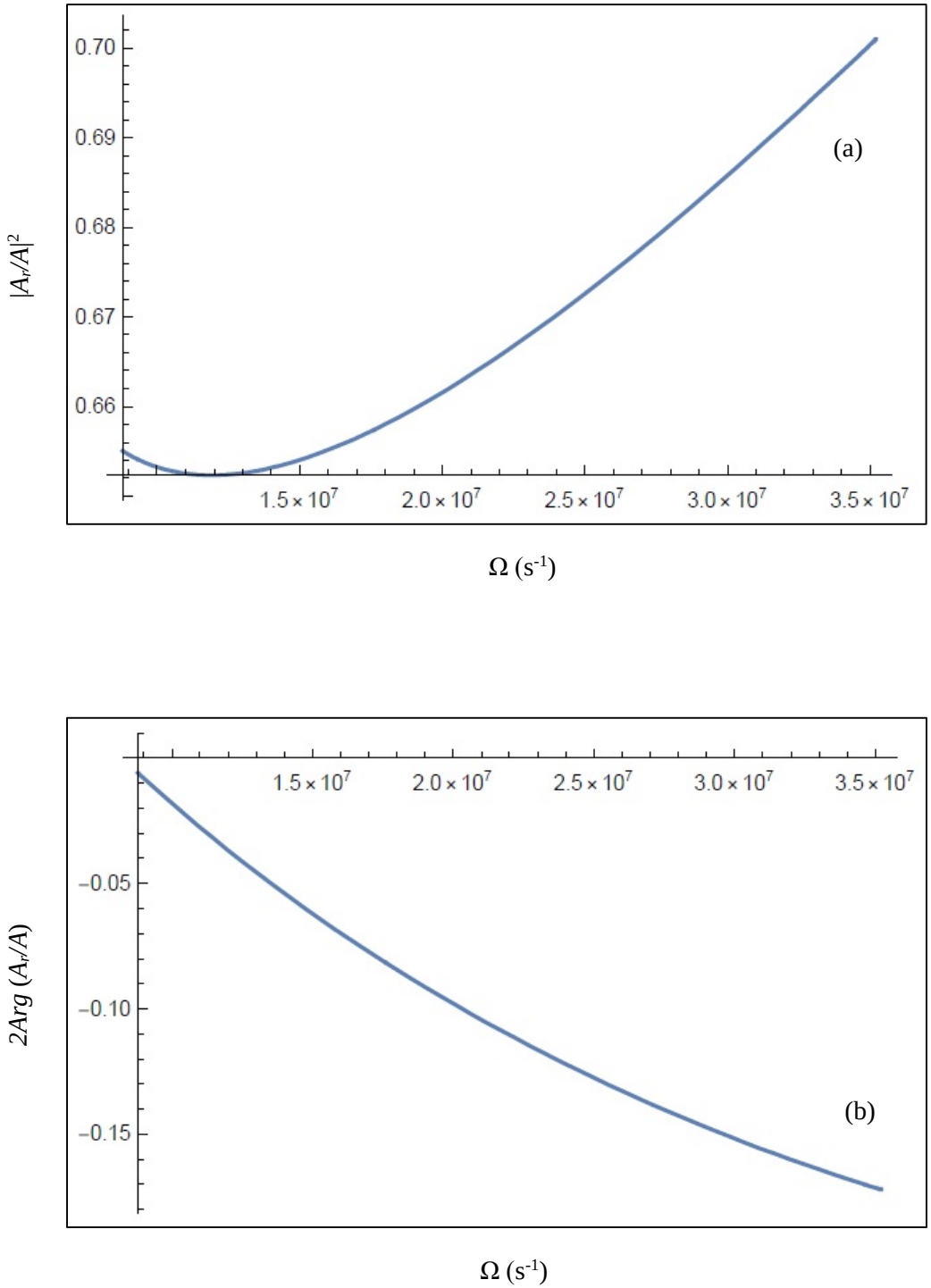

Figure 4.11. For CMIA: throughput amplitude (a) and phase (b) with respect to input as a function of modulation frequency.

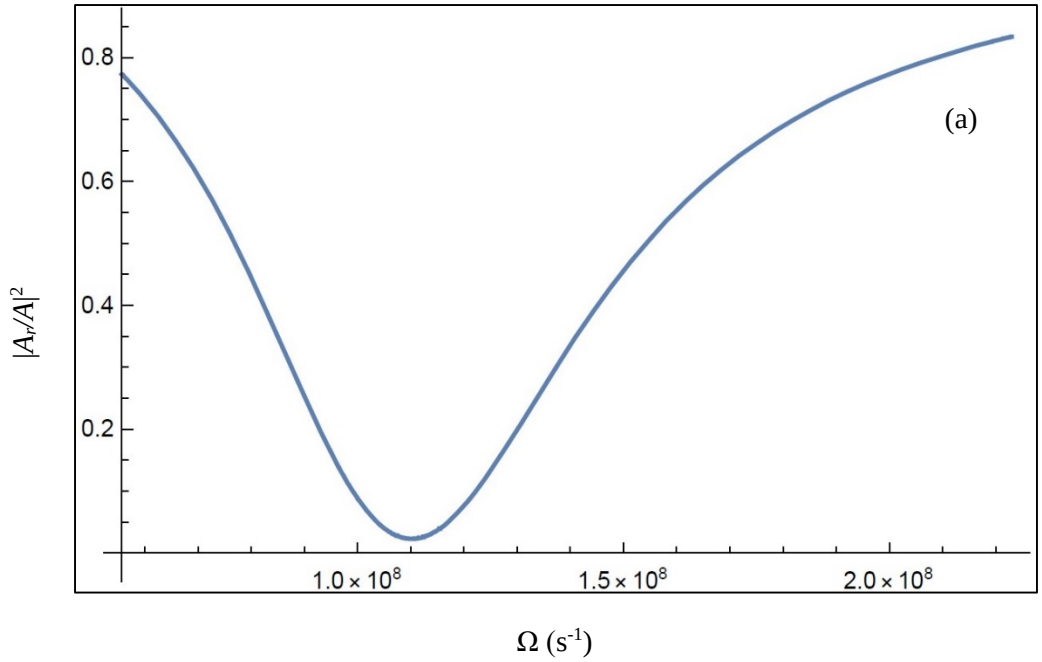

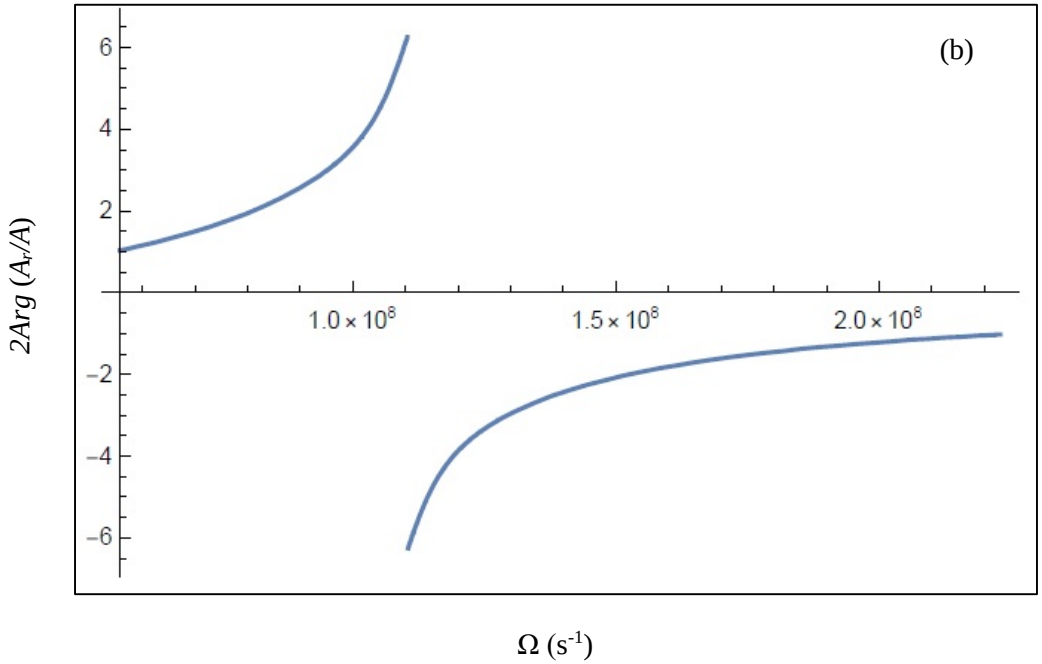

Figure 4.12. For ATS: throughput amplitude (a) and phase (b) with respect to input as a function of modulation frequency.

For the case of CMIT, we can see from the amplitude plot of Fig. 4.10(a) that the amplitude at modulation frequency of $\Omega = 2.907 \times 10^7$ s^{-1} is around 0.04. From the phase plot of Fig. 4.10(b), we can see that at the modulation frequency of $\Omega = 2.907 \times 10^7$ s^{-1} the phase shift is about -5.5, which is a little more than -2π. Both the amplitude and phase agree with the modulated throughput response of Fig. 4.7(b).

For the case of CMIA, we can see from the amplitude plot of Fig. 4.11(a) that the amplitude at modulation frequency of $\Omega = 1.76 \times 10^7$ s^{-1} is around 0.658. From the phase plot of Fig. 4.11(b), we can see that at modulation frequency of $\Omega = 1.76 \times 10^7$ s^{-1} the phase shift is about -0.085, which is a little less than 0. Both the amplitude and phase agree with the modulated throughput response of Fig. 4.8(b).

For the case of ATS, we can see from the amplitude plot of Fig. 4.12(a) that the amplitude at modulation frequency of $\Omega = 1.115 \times 10^8$ s^{-1} is around 0.01. From the phase plot of Fig. 4.12(b), we can see that at the modulation frequency of $\Omega = 1.115 \times 10^8$ s^{-1} the phase shift is almost 0. Both the amplitude and phase agree with the modulated throughput response of Fig. 4.9(b).

If we look at the $\left|\frac{A_{r_1}}{A_1}\right|^2$ plots and $2Arg(\frac{A_{r_1}}{A_1})$ plots, it seems like there is a correlation between Ω at minimum amplitude and the point at zero phase (at least for CMIT and ATS plots). So we can try writing Eq. (4.18) as

$$\frac{A_{r_1}}{A_1} = \frac{(\Omega_0{}^2 - \Omega^2) - \frac{T_1\kappa_2}{\tau_{rt}} + i\Omega[\frac{T_1}{\tau_{rt}} - (\kappa_1 + \kappa_2)]}{\Omega_0{}^2 - \Omega^2 - i\Omega(\kappa_1 + \kappa_2)} = \frac{x_1 + iy_1}{x_2 + iy_2} = \frac{z_1}{z_2} = \frac{\rho_1}{\rho_2} e^{i(\varphi_1 - \varphi_2)}, \qquad (4.22)$$

where
$$\varphi_1 = \tan^{-1}\left(\frac{y_1}{x_1}\right) = \tan^{-1}\left\{\frac{\Omega\left[\frac{T_1}{\tau_{rt}} - \left(\kappa_1 + \kappa_2\right)\right]}{\left(\Omega_0{}^2 - \Omega^2\right) - \frac{T_1\kappa_2}{\tau_{rt}}}\right\}, \tag{4.23}$$

$$\varphi_2 = \tan^{-1}\left(\frac{y_2}{x_2}\right) = \tan^{-1}\left[\frac{-\Omega\left(\kappa_1 + \kappa_2\right)}{\Omega_0{}^2 - \Omega^2}\right]. \tag{4.24}$$

Then

$$Arg\left(\frac{A_{r1}}{A_1}\right) = \phi = \varphi_1 - \varphi_2 = \tan^{-1}\left\{\frac{\Omega\left[\frac{T_1}{\tau_{rt}} - \left(\kappa_1 + \kappa_2\right)\right]}{\left(\Omega_0{}^2 - \Omega^2\right) - \frac{T_1\kappa_2}{\tau_{rt}}}\right\} - \tan^{-1}\left[\frac{-\Omega\left(\kappa_1 + \kappa_2\right)}{\Omega_0{}^2 - \Omega^2}\right]. \tag{4.25}$$

From trigonometric identity

$$\tan(\alpha - \beta) = \frac{\tan\alpha - \tan\beta}{1 + \tan\alpha\tan\beta} \tag{4.26}$$

we have

$$\tan\phi = \tan(\varphi_1 - \varphi_2) = \frac{\dfrac{\Omega\left[\frac{T_1}{\tau_{rt}} - \left(\kappa_1 + \kappa_2\right)\right]}{\left(\Omega_0{}^2 - \Omega^2\right) - \frac{T_1\kappa_2}{\tau_{rt}}} + \dfrac{\Omega\left(\kappa_1 + \kappa_2\right)}{\Omega_0{}^2 - \Omega^2}}{1 - \dfrac{\Omega\left[\frac{T_1}{\tau_{rt}} - \left(\kappa_1 + \kappa_2\right)\right]}{\left(\Omega_0{}^2 - \Omega^2\right) - \frac{T_1\kappa_2}{\tau_{rt}}}\dfrac{\Omega\left(\kappa_1 + \kappa_2\right)}{\Omega_0{}^2 - \Omega^2}} \tag{4.27}$$

$$= \frac{\left[\Omega_0{}^2 - \Omega^2 - \kappa_2\left(\kappa_1 + \kappa_2\right)\right]\frac{T_1}{\tau_{rt}}\Omega}{\left\{1 - \dfrac{\Omega\left[\frac{T_1}{\tau_{rt}} - \left(\kappa_1 + \kappa_2\right)\right]}{\left(\Omega_0{}^2 - \Omega^2\right) - \frac{T_1\kappa_2}{\tau_{rt}}}\dfrac{\Omega\left(\kappa_1 + \kappa_2\right)}{\Omega_0{}^2 - \Omega^2}\right\}\left[\left(\Omega_0{}^2 - \Omega^2\right) - \frac{T_1\kappa_2}{\tau_{rt}}\right]\left(\Omega_0{}^2 - \Omega^2\right)}.$$

Setting $\tan\phi = 0$ gives us (for large Q_2),

$$\Omega_{\min}{}^2 = \Omega_0{}^2 - \kappa_2(\kappa_1 + \kappa_2) \approx \Omega_0{}^2 - \kappa_1\kappa_2 = \frac{T_s}{\tau_{rt}{}^2}. \tag{4.28}$$

So from Eq. (4.28), when the two Qs are very different, specifically $Q_2 >> Q_1$ so $\kappa_2 << \kappa_1$,the intermode coupling strength T_s is determined only by the modulation frequency at minimum amplitude $\Omega_{\min}$.

To illustrate this, we looked at a case of typical CMIT from the model, where the parameter values chosen are experimentally realistic [29]. In this CMIT case the coupling strength is $T_s = 5 \times 10^{-8}$. We wrote a separate Mathematica program that calculates the modulation frequency Ω_{min} at the minimum modulation amplitude using Eq. (4.18). For our CMIT with $T_s = 5 \times 10^{-8}$, the program gives $\Omega_{min} = 2.36 \times 10^7\, s^{-1}$. And then with minimal perturbation to our CMIT feature and keeping the two Qs very different, we tried in the ring cavity model a range of different values of T_s and calculated Ω_{min} for each case, as in Table 1. The square of the calculated values of Ω_{min} has a near proportional dependence on T_s (Fig. 4. 13).

We continued with a case of ATS where the parameter values are the same as our CMIT but with a larger T_s. In the ring cavity model, choosing $T_s = 10^{-6}$ gave us an ATS feature, for which our new program gives $\Omega_{min} = 1.1 \times 10^8\, s^{-1}$. Again, while keeping the ATS feature and two different Qs, we tried another range of different values of T_s and calculated the corresponding values for Ω_{min} in each case, as in Table 2. The square of the calculated values of Ω_{min} also has a near proportional dependence on T_s (Fig. 4.14).

Table 1. Calculated values of Ω_{min}^2 (s^{-2}) for a range of T_s for CMIT.

T_s	Ω_{min}	Ω_{min}^2
1×10^{-8}	0.757×10^7	0.573049×10^{14}
2×10^{-8}	1.36×10^7	1.8496×10^{14}
3×10^{-8}	1.76×10^7	3.0976×10^{14}
4×10^{-8}	2.08×10^7	4.3264×10^{14}
5×10^{-8}	2.36×10^7	5.5696×10^{14}
6×10^{-8}	2.6×10^7	6.76×10^{14}
7×10^{-8}	2.83×10^7	8.0089×10^{14}
8×10^{-8}	3.04×10^7	9.2416×10^{14}
9×10^{-8}	2.23×10^7	10.4329×10^{14}
10×10^{-8}	3.43×10^7	11.6964×10^{14}

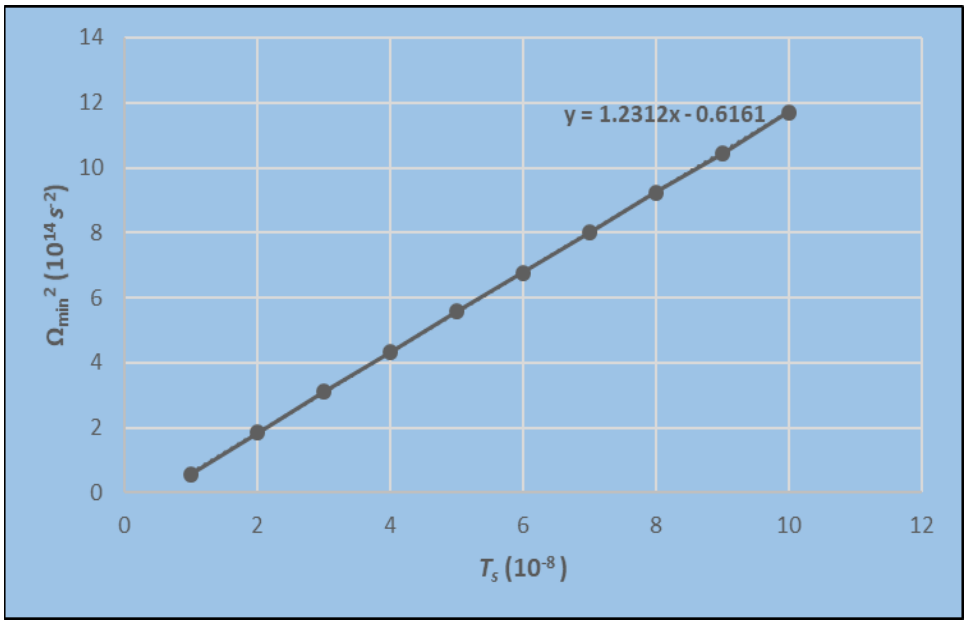

Figure 4.13. Near proportional dependence of T_s on Ω_{min}^2 for CMIT.

Table 2. Calculated values of Ω_{min}^2 (s^{-2}) for a range of T_s for ATS.

T_s	Ω_{min}	Ω_{min}^2
0.3×10^{-6}	0.6×10^{8}	0.36×10^{16}
0.5×10^{-6}	0.78×10^{8}	0.6084×10^{16}
0.7×10^{-6}	0.92×10^{8}	0.8464×10^{16}
0.9×10^{-6}	1.046×10^{8}	1.094116×10^{16}
1×10^{-6}	1.1×10^{8}	1.21×10^{16}
3×10^{-6}	1.91×10^{8}	3.6481×10^{16}
5×10^{-6}	2.47×10^{8}	6.1009×10^{16}
7×10^{-6}	2.92×10^{8}	8.5264×10^{16}
9×10^{-6}	3.31×10^{8}	10.9561×10^{16}

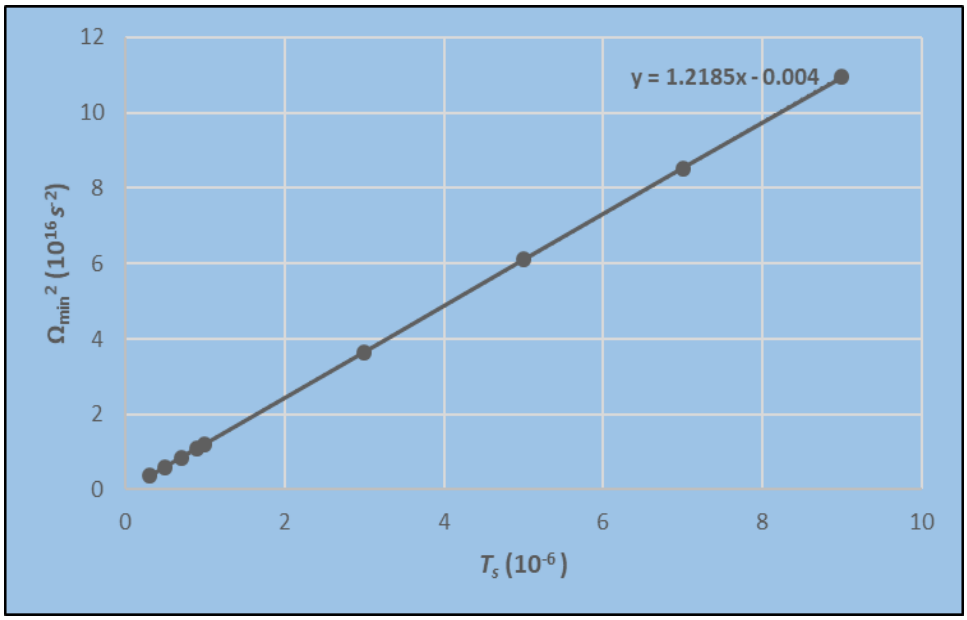

Figure 4.14. Near proportional dependence of T_s on Ω_{min}^2 for ATS.

Both graphs are linear, meaning that our approximation in Eq. (4.28) in numerical analysis is reasonable, at least for CMIT and ATS where the two *Q*s are very different. In the graphs, the y-intercept represents the difference between the true values of Ω_{min}^2 and our approximation in Eq. (4.28), namely κ_2^2. For our cases, however, this difference can be neglected since $\kappa_2 << \kappa_1$. Then we can establish a direct proportional relation between Ω_{min}^2 and T_s. Previously [30], experimental throughput spectra such as in Fig. 4.2(a) and 4.3(a) were fit to the model by adjusting the value of T_s in the model. This is how the values of T_s used in those figures were found. Our numerical investigation leads us to think that, experimentally, by only finding the modulation frequency corresponding to minimum modulation amplitude, we should be able to directly estimate the CPC strength without the need to fit to a computer model.

CHAPTER V

EXPERIMENTAL RESULTS

We have investigated in the numerical model the dependence of the response on CPC strength, input coupling regimes and strength, *Q* values, etc. Now that we have a clear understanding, we can compare these results to expectations from the analytic analysis and predict which parameter ranges should enhance experimental observation of the CPC effects. Using these guidelines, we have performed an experimental investigation of CPC dynamics in the HBR system. Specifically, we use sinusoidal modulation to independently determine the CPC strength in CMIT/ATS experiments.

5.1. Experimental Setup

The experimental setup we used is shown in Fig. 5.1 and explained in detail in the following text.

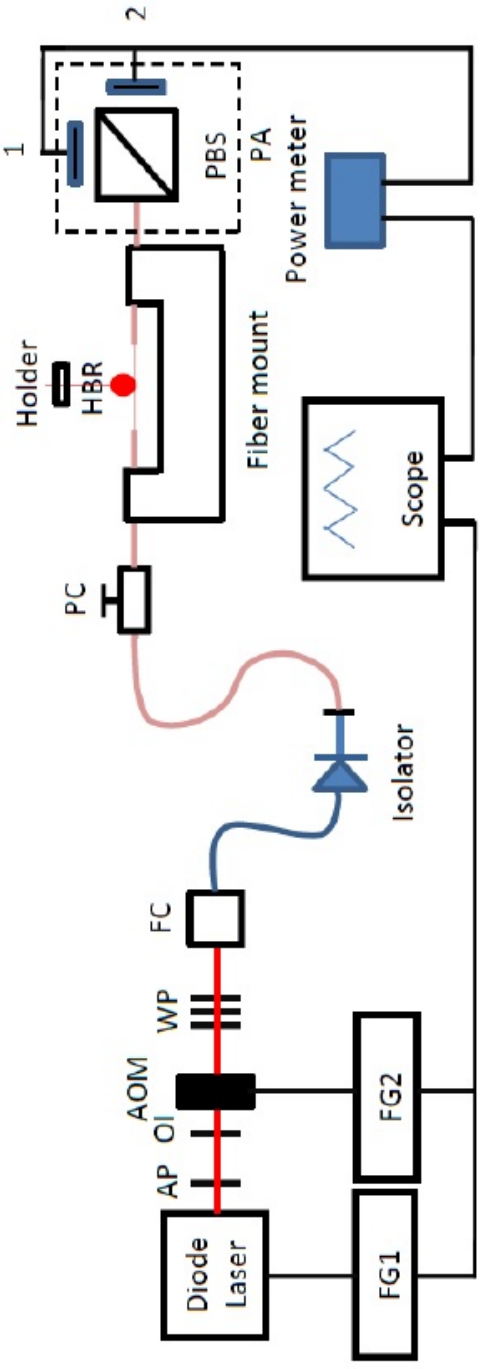

Figure 5.1. Experimental setup for studying the CPC dynamics in an HBR [29].

The tunable diode laser is scanned in frequency by function generator FG1. An acousto-optic modulator (AOM), controlled by function generator FG2, is then used to split the incoming beam into two outgoing parts: the zeroth-order undeflected beam of higher intensity with the same frequency and direction, and the first-order deflected beam of lower intensity with different frequency and direction from the incoming beam. Before going to the fibercoupler (FC), the deflected light beam passes through a set of wave plates (WP) which are used to control the input polarization. Usually, the wave plates are adjusted to provide linearly polarized light. The fiber coupler FC launches the light into a single mode fiber. The fiber isolator, acting as an optical diode, is used to prevent any backward propagating light. The single mode fiber is also mounted in a compression based polarization controller, PC, for further regulation of the input light. The fiber is made adiabatically bi-tapered using a puller stage (see Fig. 5.2) controlled by a LabVIEW program and brought into contact with the HBR in its equatorial plane using a 3D translation stage (not shown). The HBR is mounted on a piezo-controlled strain tuner (see Fig. 5.3) for strain tuning.

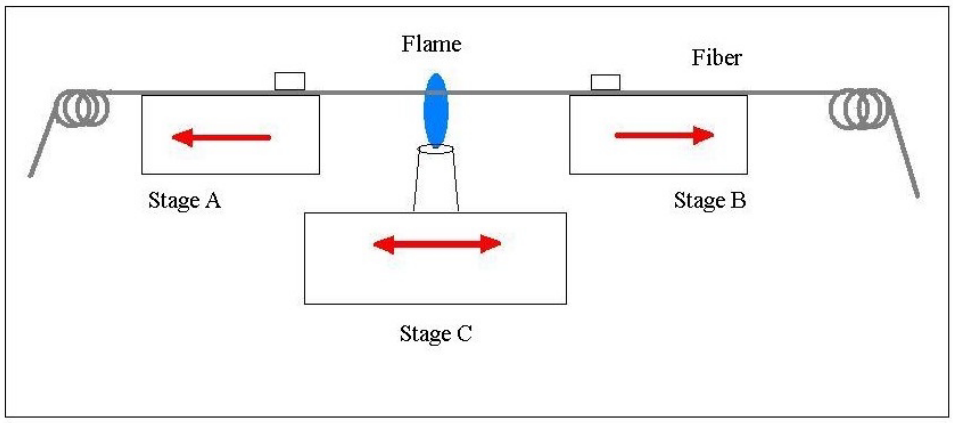

Figure 5.2. Fiber puller stage for tapering optical fibers.

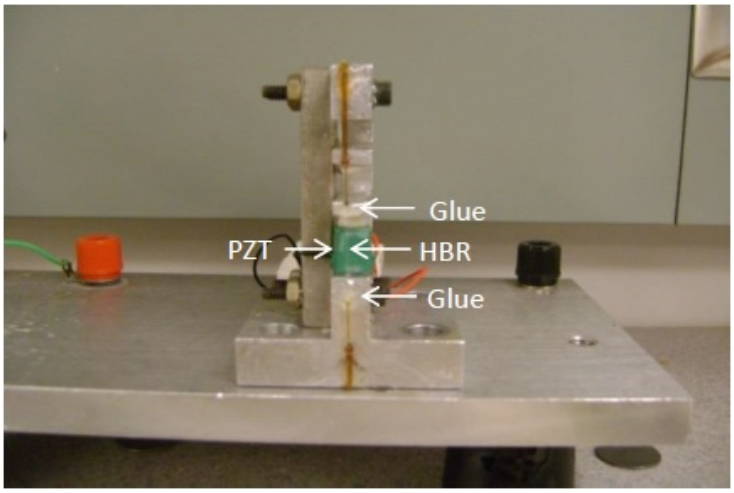

Figure 5.3. Piezo-controlled strain tuner. The HBR is glued at two points on the PZT for streching.

In all cases, the resonator is kept inside an acrylic box to minimize the temperature fluctuations and other effects of air movement. The output signal is sent to a fiber coupled polarization analyzer (PA) which includes the polarizing beam splitter (PBS) and two detectors, 1-fast detector and 2-slow detector. For data analysis, the signal on the slow detector is captured with the power meter and sent to the oscilloscope while the fast detector is directly connected to the oscilloscope.

Strain tuning to coresonance and proper adjustment of the input polarization will result in the throughput spectrum consisting of the throughput power vs. scanned laser frequency. A set of typical CMIT and CMIA throughput spectra are shown in Fig. 5.4 where the input is TM polarized.

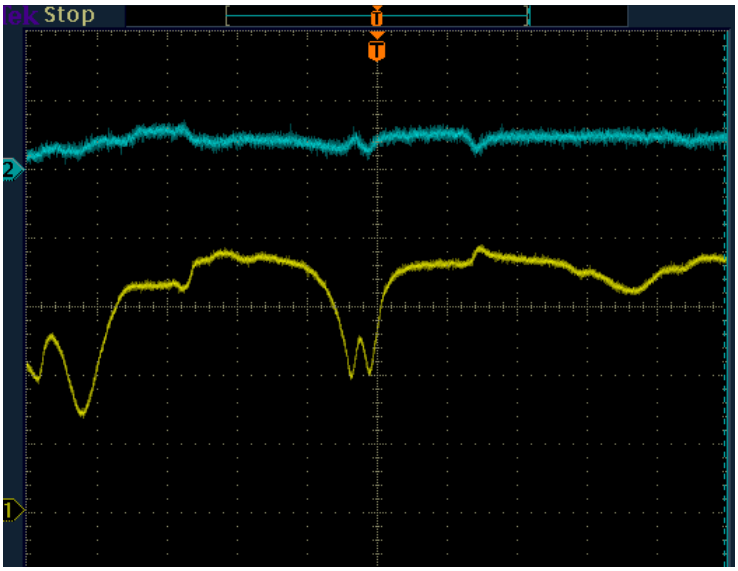

(a)

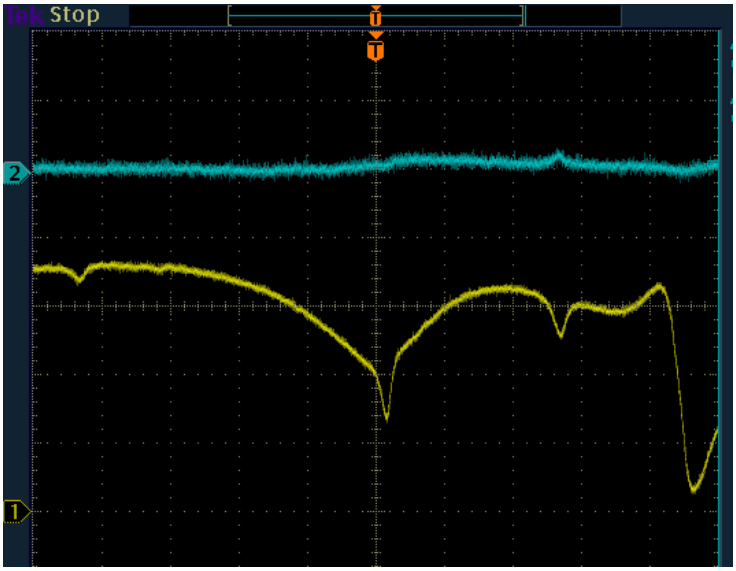

(b)

Figure 5.4. Experimental throughput power spectra (lower, yellow trace). (a): CMIT; (b): CMIA. [30].

5.2. Experimental Procedures

To start the CMIT/CMIA experiments, first we need to make sure only one polarization is driven at the input. Using only one polarization, either TE or TM, for the input will reduce the spectral mode density of the throughput signal, compared to the spectral mode density of the throughput power when the input has an arbitrary polarization (as seen in Fig. 5.5).

In Fig. 5.5 and subsequent oscilloscope traces, the horizontal time axis is converted to frequency through the use of a Mathematica scaling program. This program is the result of a careful calibration of frequency scan range dependence on the amplitude of the triangle-wave voltage signal provided by FG1 of Fig. 5.1. This, together with the frequency of the triangle wave, allows the conversion from time to scanned frequency.

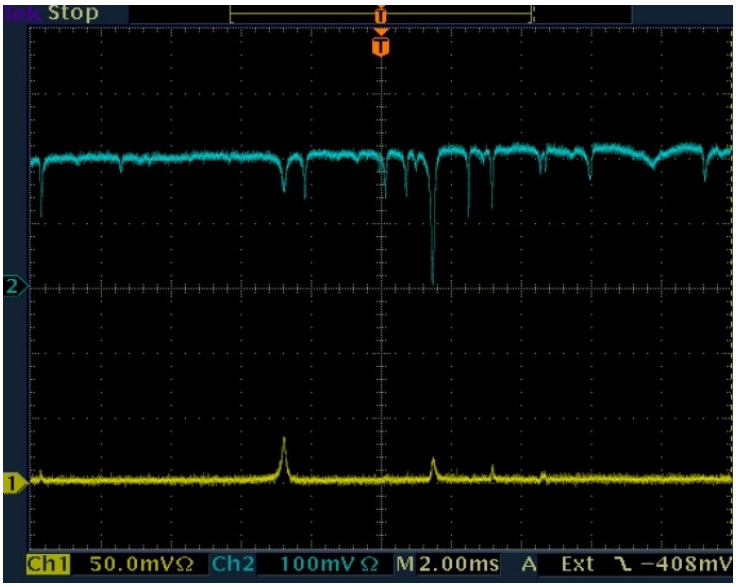

(a)

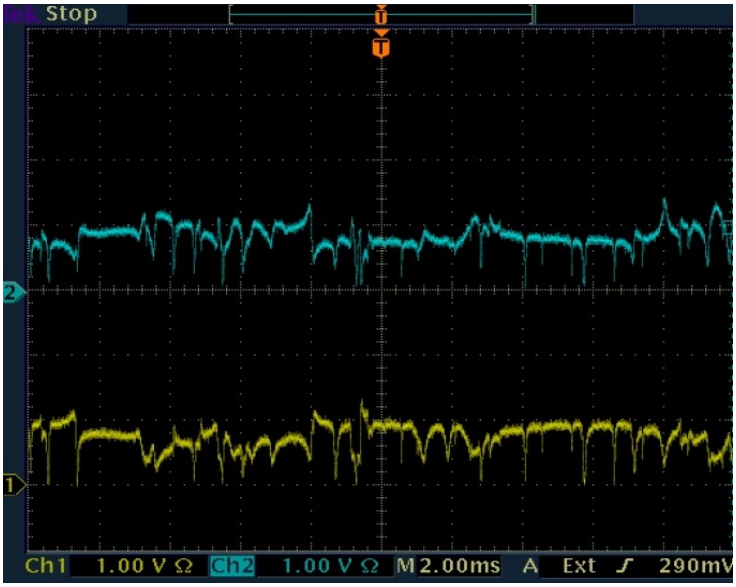

(b)

Figure 5.5. Throughput spectrum when the input has TE polarization (a) compared to throughput spectrum when the input has arbitrary polarization (b). Blue: TE throughput; yellow: TM throughput.

We begin by applying some voltage across the PZT (around 50 V) before exciting WGMs, so we have the freedom to strain tune in both directions from 0 to 100 V. Then, to get linearly polarized light at the input, we excite the WGMs and rotate the analyzer 45 degrees with respect to the vertical (TE) axis. In this orientation, each detector (fast detector and slow detector) will display dips corresponding to both TE and TM modes. Now we rotate the polarization controller (PC) to make half of the modes disappear in each channel. Then we move the fiber away from the resonator and rotate the analyzer back to 0 degree. If the power in the slow detector increases and the power in the fast detector decreases, then we have more TM polarization at the input than TE polarization. If the power in the slow detector decreases and the power in the fast detector increases, then we have more TE polarization at the input than TM polarization. At this point, we can use the wave plates to maximize the power in one of the channels and get linearly polarized input on whichever channel we need.

The examples in Fig. 5.4 are CMIT/CMIA detected on the slow detector when the input is linearly TM polarized. And TM polarization at the input is preferred because the TM modes usually have lower *Q* values. In our experiment, we can also use TE polarization at the input. But in both cases, we need to show the CMIT/CMIA feature on the fast detector channel (Fig. 5.6). Because we are going to modulate the input sinusoidally to look at the response on the throughput amplitude and phase. Modulation frequency is in the range of a few MHz. The slow detector cannot respond to these frequencies. Only the fast detector is able to respond to this modulation (Fig. 5.7). So in our experiments, when we have TE input, we look for the CMIT/CMIA features in the fast detector (TE) channel without rotating the analyzer. When we have TM input, we look for the CMIT/CMIA features in the slow detector (TM) channel and rotate the analyzer by 90 degrees for modulating the throughput amplitude.

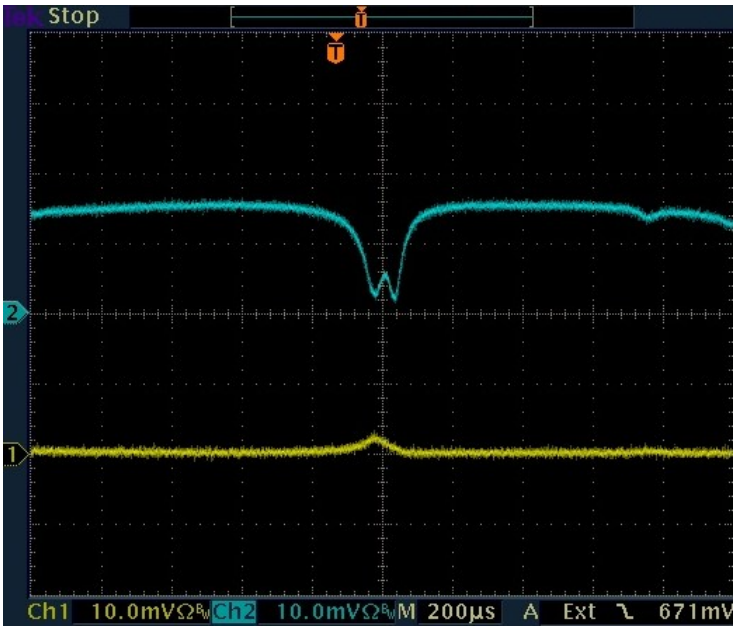

(a)

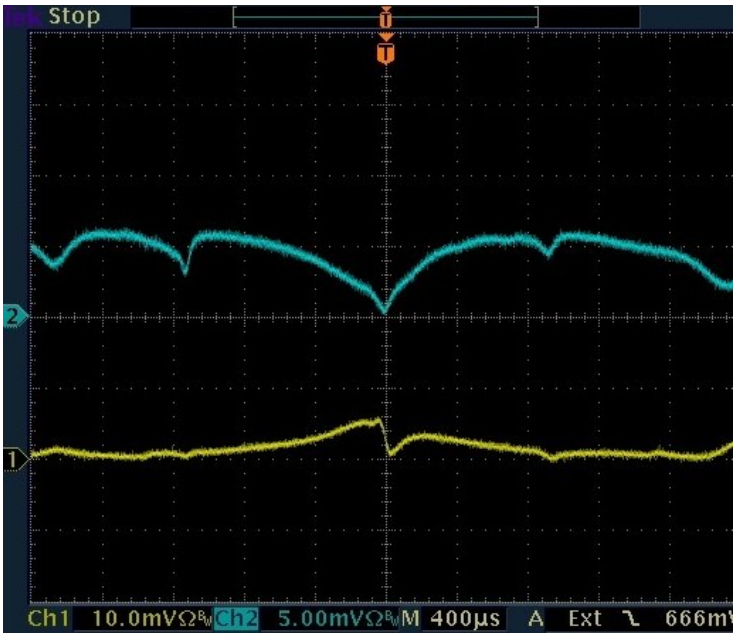

(b)

Figure 5.6. Experimental throughput power spectra in the fast detector channel when the input has TE polarization (upper, blue trace). (a): CMIT; (b): CMIA.

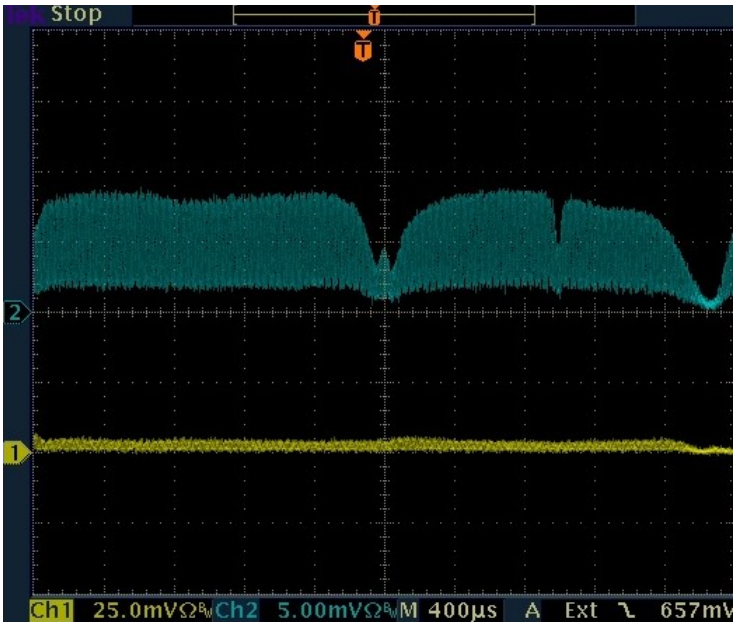

(a)

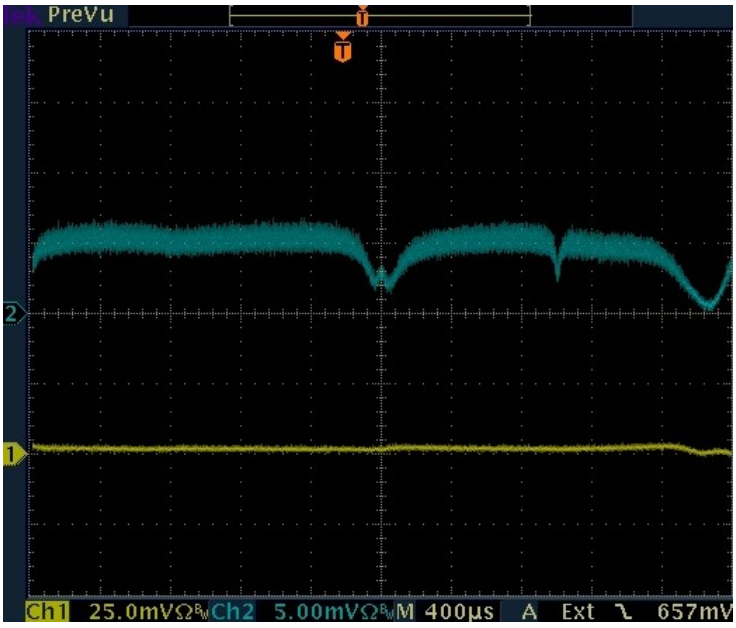

(b)

Figure 5.7. Modulation response of the fast detector channel (upper, blue trace) and slow detector (lower, yellow trace) to a low frequency (a) and a high frequency (b).

To measure the relevant parameters of the CMIT coupling modes, the input polarization is changed to linear at 45 degrees by using the half-wave plate. At this point the throughput powers measured from the fast detector and the slow detector are equal, and the coresonant TE and TM pair of modes with very different quality factors are determined as follows. During the CMIT experiment, CPC can happen and change the true values of the mode parameters like quality factors, dip depths, and coupling regimes of the coresonant TE and TM modes. So in order to determine the mode parameters correctly, detuning the coresonant TE and TM modes is necessary. For CMIT/CMIA or ATS features as Fig.5.6, we want to detune the resonance modes at 45 degrees input as shown in Fig. 5.8; coresonant in (a), detuned and indicated by arrows in (b). And then look at the individual modes in each polarization and measure the mode parameters. We use those values to fit the throughput spectrum to the model and get our first estimate of T_s.

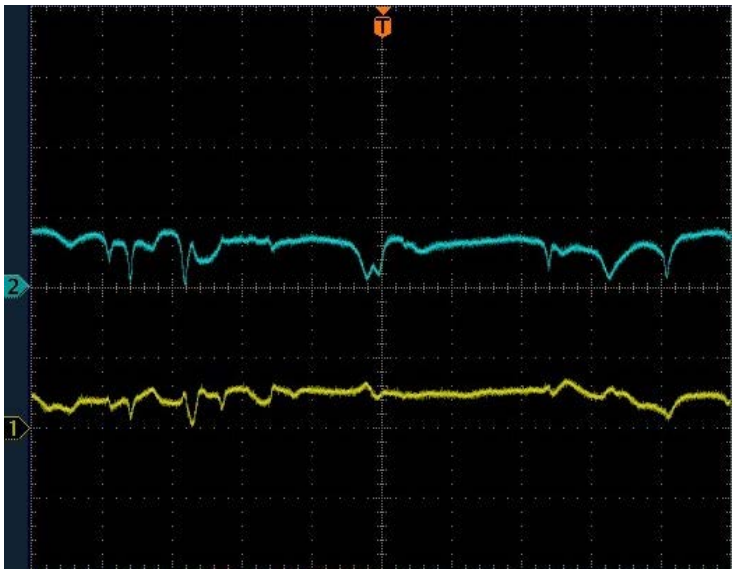

(a)

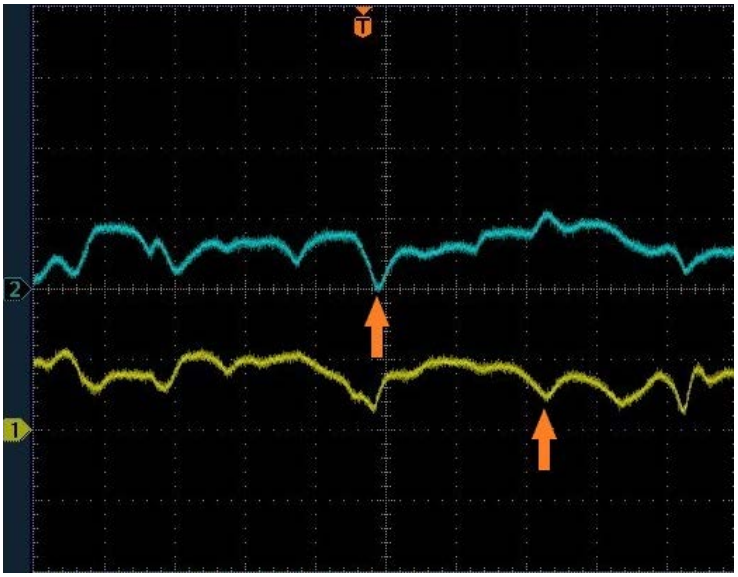

(b)

Figure 5.8. Coresonant TE and TM modes showing CMIT in (a) and detuned and indicated by arrows in (b) when the input polarization is 45 degrees.

After we detune the modes at 45 degrees input, the two modes are off resonance so we don't see an IT anymore. But this doesn't mean we can take measurements of the individual mode parameters at this point. Because when the input polarization is at 45 degrees, we have both TE and TM input. Even if they are completely detuned, some residues from one polarization will remain in the throughput spectrum of the other polarization. In order to solve this problem, we take measurements at 0 degree input and 90 degrees input, for TE and TM modes, respectively.

At 0 degree input, we will get the detuned TE mode in Channel 2, from which we take our measurements for mode linewidth in time (from which we use the Mathematica scaling program to calculate the mode quality factor *Q*), as in Fig. 5.9. We also measure mode dip depth (the ratio of the voltage difference at the dip to the full voltage difference), as in Fig. 5.10.

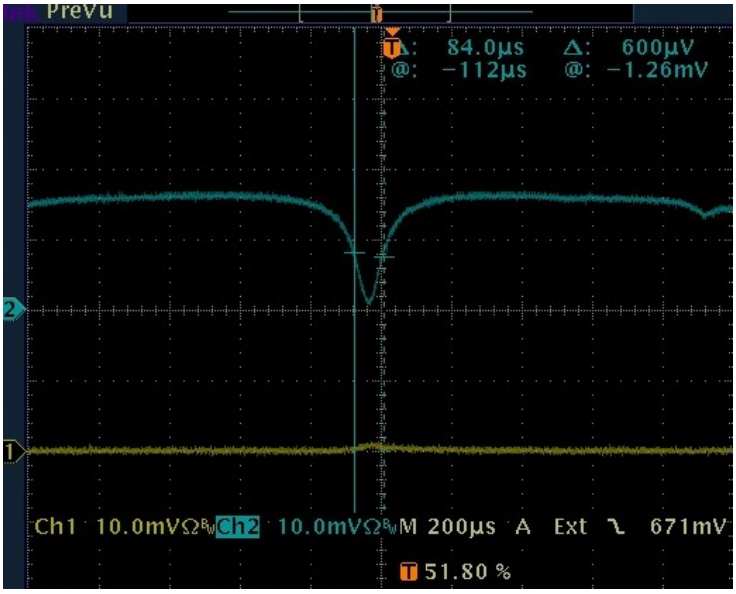

Figure 5.9. Linewidth measurement for TE mode (upper, blue trace). A linewidth in time of 84.0 µs corresponds to a quality factor of $Q = 2.7 \times 10^7$.

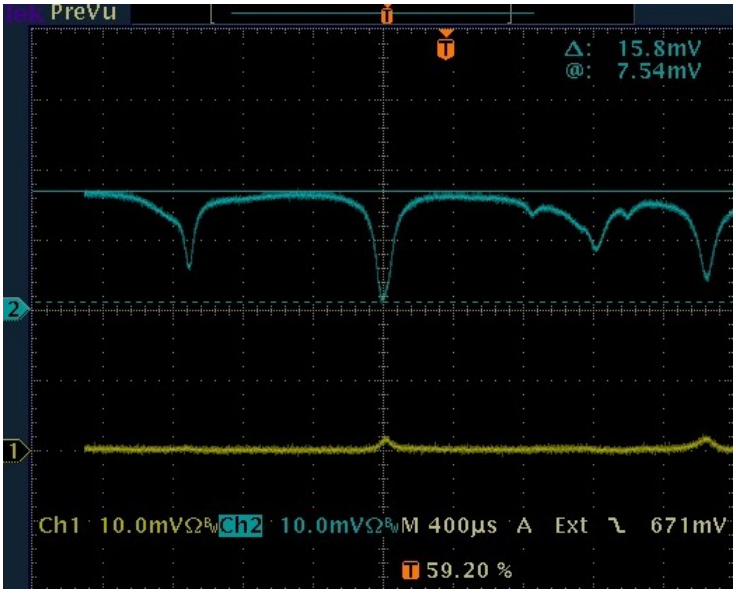

(a)

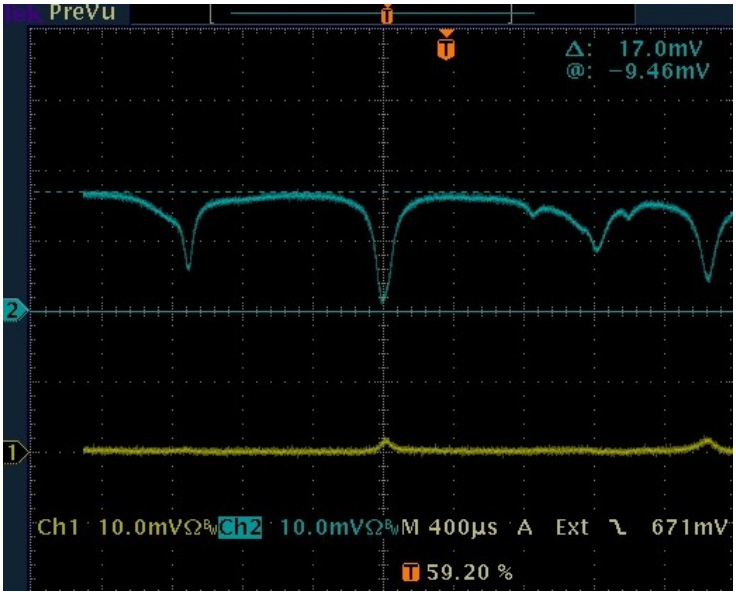

(b)

Figure 5.10. Dip depth measurement for TE mode (upper, blue trace). The ratio of the cursor voltage difference at the dip (a) to the full voltage difference (b) gives a dip depth of 0.93.

Finally, the coupling regime of the mode is found by adding extra loss by touching the mode region with a segment of another tapered fiber: if the dip of the WGM throughput gets shallower, we have an undercoupled mode; if the dip of the WGM throughput gets deeper, we have an overcoupled mode. Fig. 5.11 illustrates WGM dip depth variation for undercoupled and overcoupled modes. We need to be very careful when determining the coupling regimes. We need to put the segment of the second tapered fiber in contact with the HBR on the opposite side of the working tapered fiber. This increases the total round-trip loss. It has to be done in a gentle manner. For example, for an overcoupled mode, if we push the second fiber too hard, the dip depth may get shallower, because it passes through critical coupling, and make the mode look like an undercoupled mode.

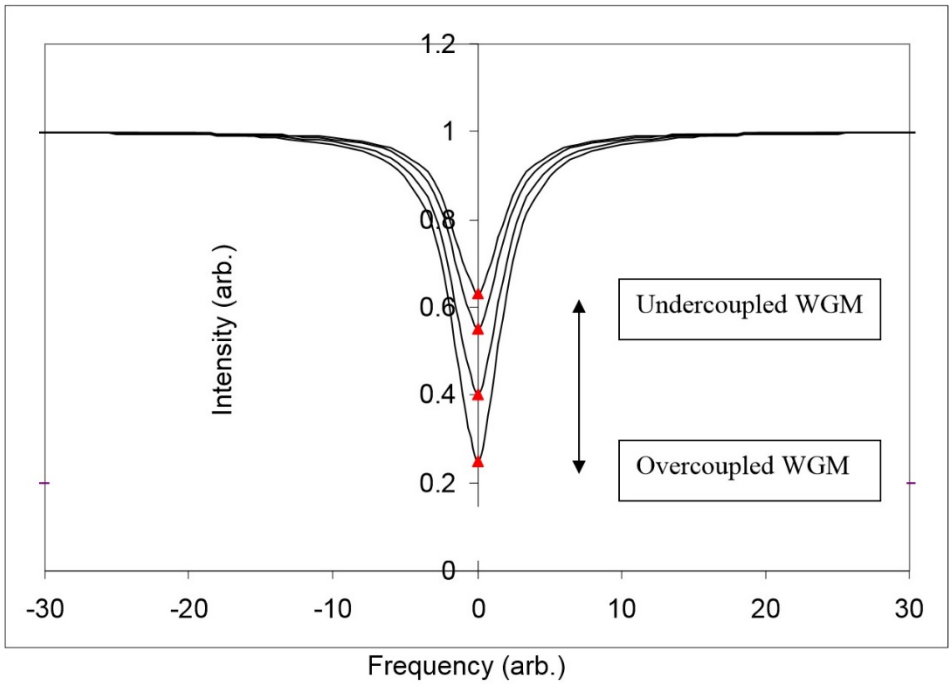

Figure 5.11. WGM dip depth variation for overcoupled and undercoupled modes. When the round-trip loss increases, the dip gets shallower for undercoupled WGMs; the dip gets deeper for overcoupled WGMs.

After taking measurements for the TE mode, we rotate our input polarization to 90 degrees, while keeping the output analyzer at 0 degree. This step will minimize the TE channel and maximize the TM channel. So we can take the measurements for TM mode (Fig. 5.12, Fig. 5.13) and determine the coupling regime for TM mode as in Fig. 5.11.

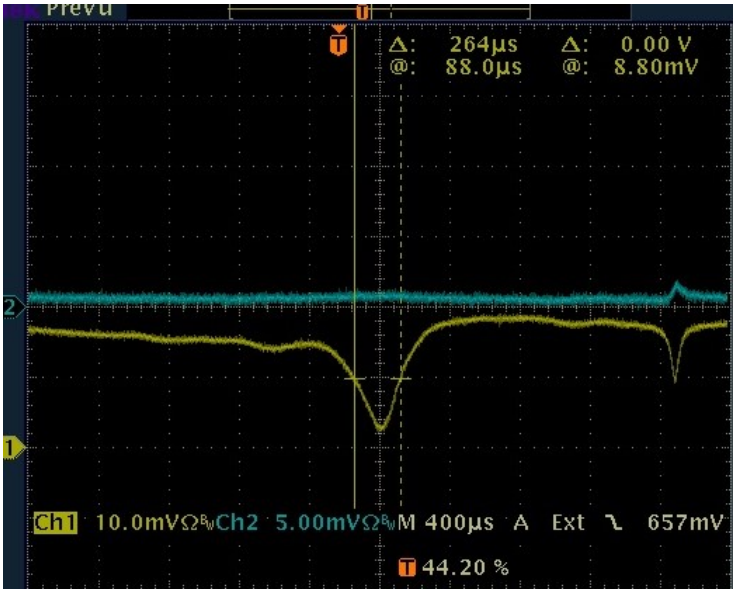

Figure 5.12. Linewidth measurement for TM mode (lower, yellow trace). A linewidth in time of 264 µs corresponds to a quality factor of $Q = 8.3 \times 10^6$.

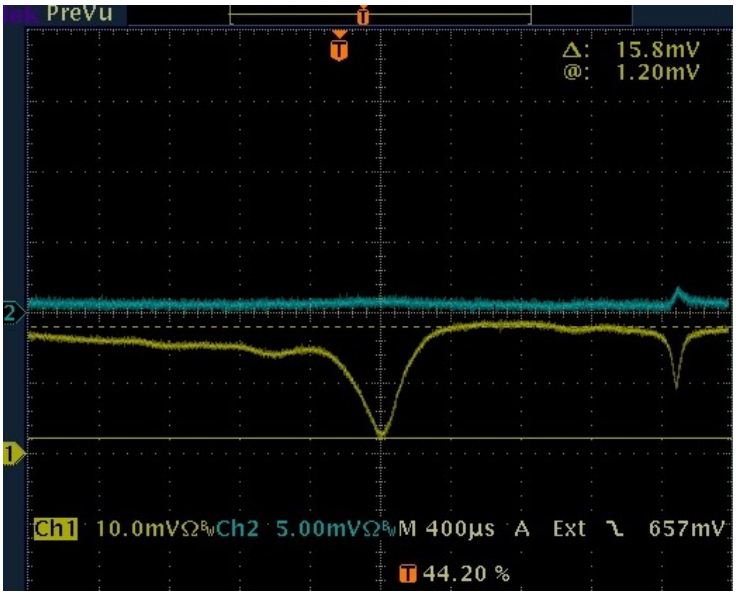

(a)

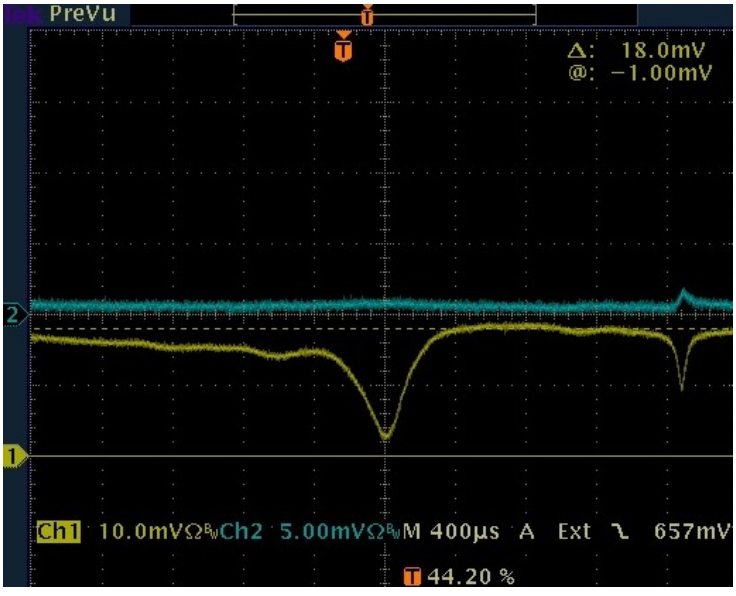

(b)

Figure 5.13. Dip depth measurement for TM mode (lower, yellow trace). The ratio of the cursor voltage difference at the dip (a) to the full voltage difference (b) gives a dip depth of 0.88.

Using the individual mode parameters, we fit our CMIT feature in the program by adjusting the value of CPC strength and get our first estimate of the T_s.

After that, we carefully bring the two detuned modes back to resonance and retrieve our CMIT feature. And then we turn on the sinusoidal modulation to look at the response of the throughput spectrum. We vary the modulation frequency and record the amplitude of the modulated signal at different modulation frequencies (Fig. 5.14). Here we are looking for the modulation frequency that gives the minimum amplitude at the WGM resonance (the IT peak) relative to the modulation amplitude far off resonance, as in Fig. 5.14 (c).

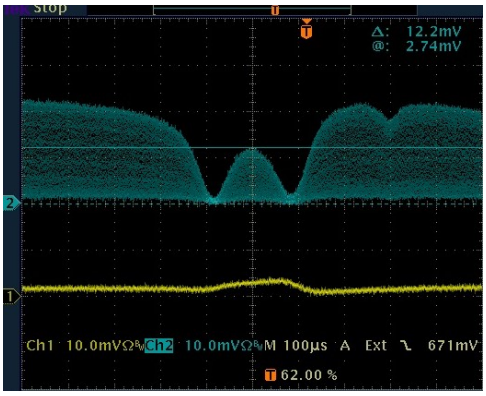

(a)

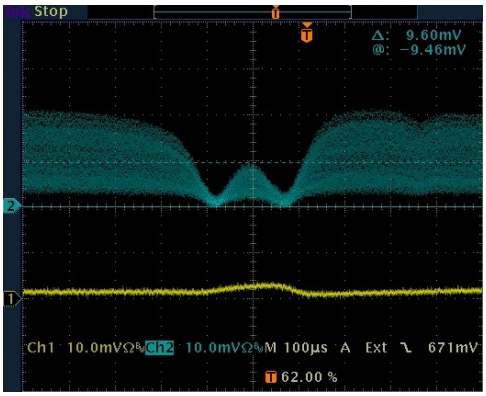

(b)

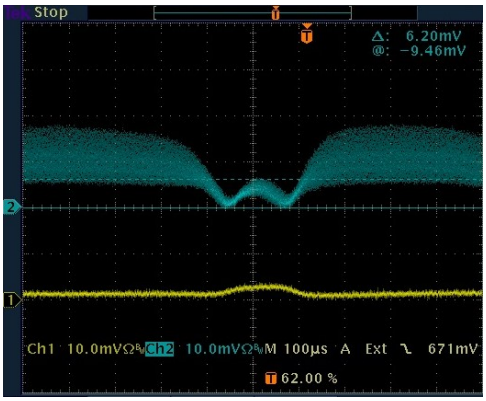

(c)

Figure 5.14. Relative amplitude of the modulated throughput signal in the fast detector channel (upper, blue trace) at a range of different modulation frequencies of the AOM. (a) at 1 MHz, (a) at 3 MHz and (c) at 4.2 MHz.

We hope that, at the frequency that gives the minimum modulation amplitude, we can use the relation $\Omega_{\min}{}^2 = \frac{T_s}{\tau_{rt}{}^2}$ to find another estimate of the CPC strength for comparison.

5.3. Results and Discussion

The following results were obtained by using 4 HBRs with different radii: 180 μm, 190 μm, 200 μm and 220 μm. The tapered fiber diameter ranges from 2 μm to 3.5 μm.

In each case, we started from a CMIT/ATS feature in one channel as in Fig. 5.15, and detuned the modes using the procedures outlined above and took measurements for the individual modes. From Fig. 5.15, we can also see some nonzero power in the second channel (both in the experiment and in the model). This indicates that our CMIT/ATS effects are truly the result of cross coupling between the two orthogonal polarization rather than interference between modes of the same polarization.

After measuring the individual mode parameter values, we fit the experimental CMIT feature to our model. This gives us the first estimate of the CPC strength.

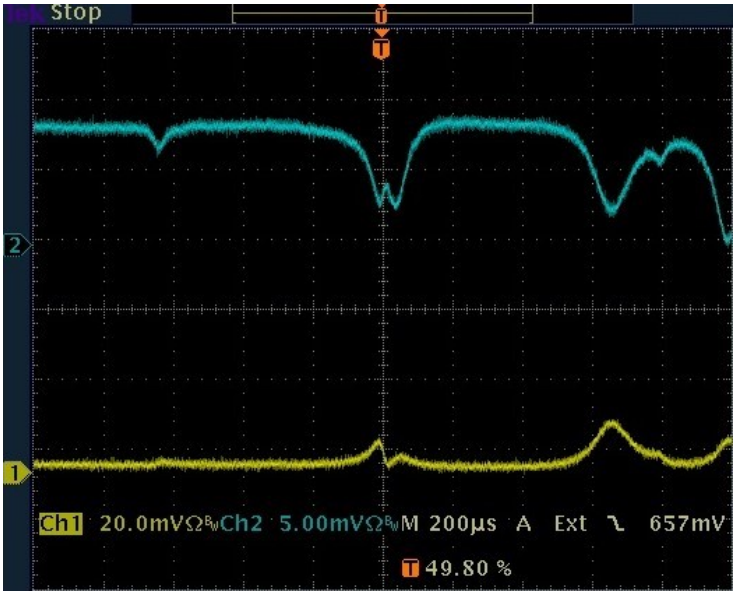

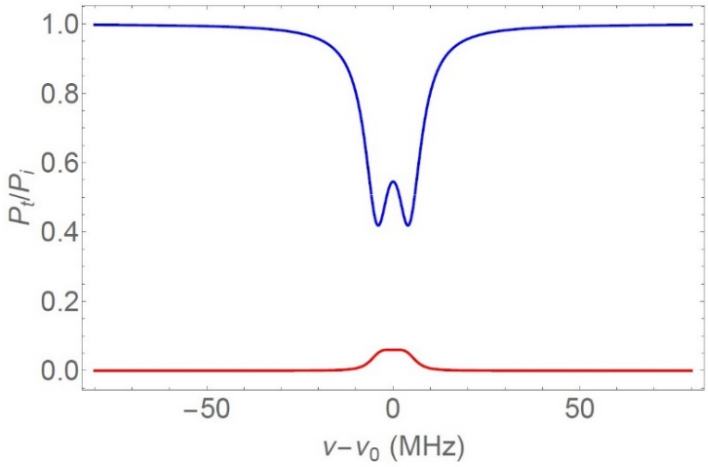

Figure 5.15. CMIT/ATS experimental throughput spectrum (top) compared to model throughput spectrum (bottom). Some nonzero power can be seen in the second channel (both experimentally and in the model prediction), indicating that our CMIT/ATS effects are truly the result of CPC.

Then we turned on the sinusoidal modulation on the AOM and tried to minimize the relative amplitude (as in Fig. 5.14). When we have a minimum relative amplitude, we record the modulation frequency. Using the modulation frequency at the minimum modulation amplitude, we calculate the CPC strength from $\Omega_{\min}{}^2 = \frac{T_s}{\tau_{rt}{}^2}$, where $\tau_{rt} = \frac{2\pi an}{c}$.The two values of CPC strength are then compared to each other. For each case, we use Eq. (4.13) to determine if it is CMIT or ATS: $\frac{T_s}{\tau_{rt_1}\tau_{rt_2}} < \left(\frac{\kappa_1 - \kappa_2}{2}\right)^2$ for CMIT and $\frac{T_s}{\tau_{rt_1}\tau_{rt_2}} > \left(\frac{\kappa_1 - \kappa_2}{2}\right)^2$ for ATS.

Note that the sinusoidal modulation of the input field amplitude is achieved by using our AOM, which has a finite response time and limits the modulation frequency to less than 10 MHz (actually the modulation signal starts to be distorted when the frequency exceeds 5 MHz). So we had to keep the modulation frequency relatively low. From the model fitting result, we estimate the range of the modulation frequency we need. If it is too large, we will skip that set of data and look for another CMIT/ATS feature that gives a modulation frequency within the safe range. Another challenge is that the presence of mode overlap in the throughput spectra made it difficult to find clear CMIT and ATS features. By using tapered fibers with larger diameters, we reduced the mode density and hence minimized mode overlap of the WGMs when the tapered fiber is in contact with the HBR. For a number of cases of CMIT and ATS, we estimated the CPC strength from model fitting and observed the modulation amplitude of the input field to get another estimate of CPC strength; these are shown in Figs. 5.16 – 5.35. In the captions of Figs. 5.16 – 5.35, "detuning" means the difference $v_2 - v_1$ of the resonant frequencies of the two WGMs. Table 3 compares the values of T_s from numerical fitting and from amplitude modulation for the cases shown in Figs. 5.16 – 5.35.

First, let's look at some cases when the input has TE polarization. Figs. 5.16 – 5.22 show some experimental CMIT throughput spectra (gray) fitted with model (blue) in the top figures; and the bottom figures show the modeled relative modulation amplitude (blue) corresponding to the fitted T_s compared to the minimum relative modulation amplitude (green dashed lines) found in the experiment. The experimental throughput spectrum is properly scaled in frequency, as discussed earlier, and imported into the Mathematica model program using Python. This allows us to directly compare the experimental trace to the model trace and do the fitting precisely.

The results are presented with increasing modulation frequency of the AOM.

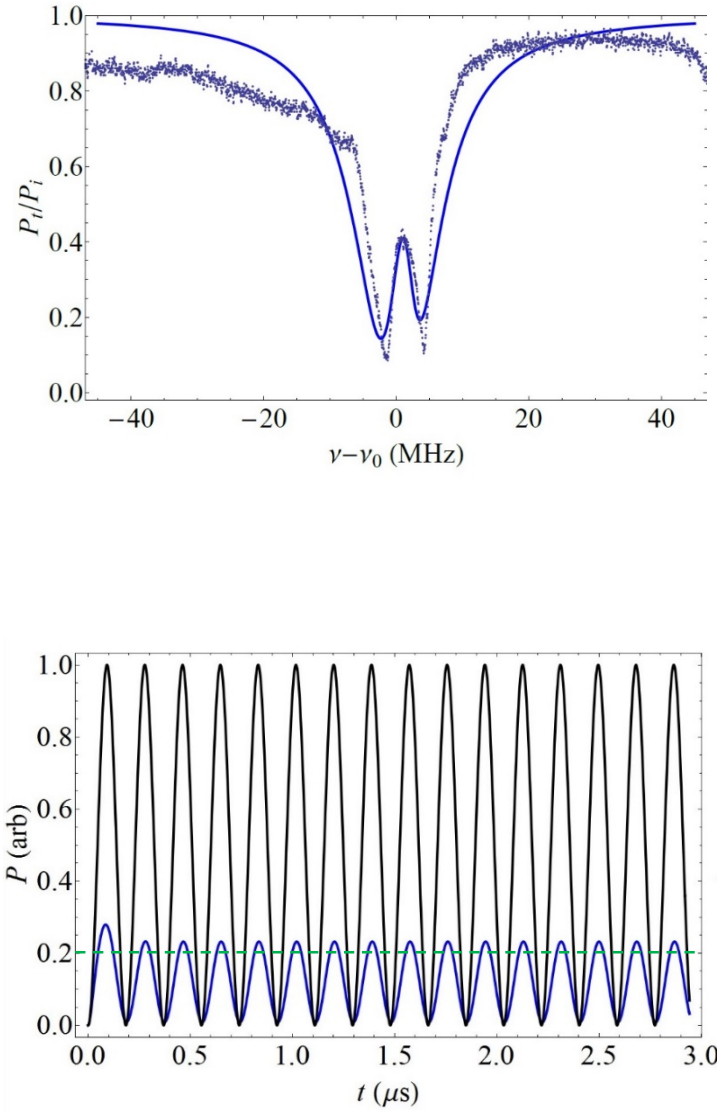

Figure 5.16. CMIT (TE input) with 220-μm-radius HBR.
Top: experimental throughput trace (gray) fit into the model (blue) throughput spectra, which gives $T_s = 1.26 \times 10^{-8}$. Bottom: Modeled relative modulation amplitude of 0.23 corresponding to the fitted T_s. Mode parameters: $Q_1 = 1.5 \times 10^7$, $Q_2 = 8.6 \times 10^7$; $M_1 = 0.90$ (undercoupled), $M_2 = 0.74$ (undercoupled); detuning = 1.2 MHz. A minimum relative modulation amplitude of 0.20 was found (green dashed line) at 3.5 MHz using the AOM, giving $T_s = 2.11 \times 10^{-8}$.

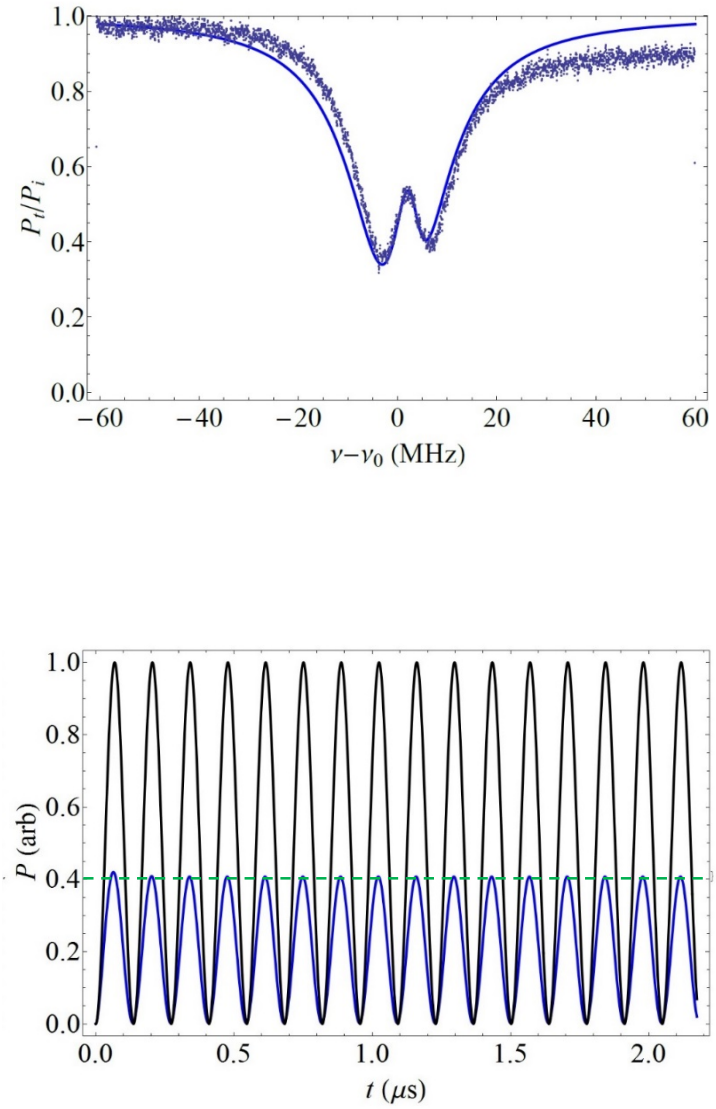

Figure 5.17. CMIT (TE input) with 200-μm-radius HBR.
Top: experimental throughput trace (gray) fit into the model (blue) throughput spectra, which gives $T_s = 1.99 \times 10^{-8}$. Bottom: Modeled relative modulation amplitude of 0.40 corresponding to the fitted T_s. Mode parameters: $Q_1 = 9.6 \times 10^6$, $Q_2 = 5.2 \times 10^7$; $M_1 = 0.70$ (undercoupled), $M_2 = 0.65$ (undercoupled); detuning = 2.3 MHz. A minimum relative modulation amplitude of 0.40 was found (green dashed line) at 4.0 MHz using the AOM, giving $T_s = 2.29 \times 10^{-8}$.

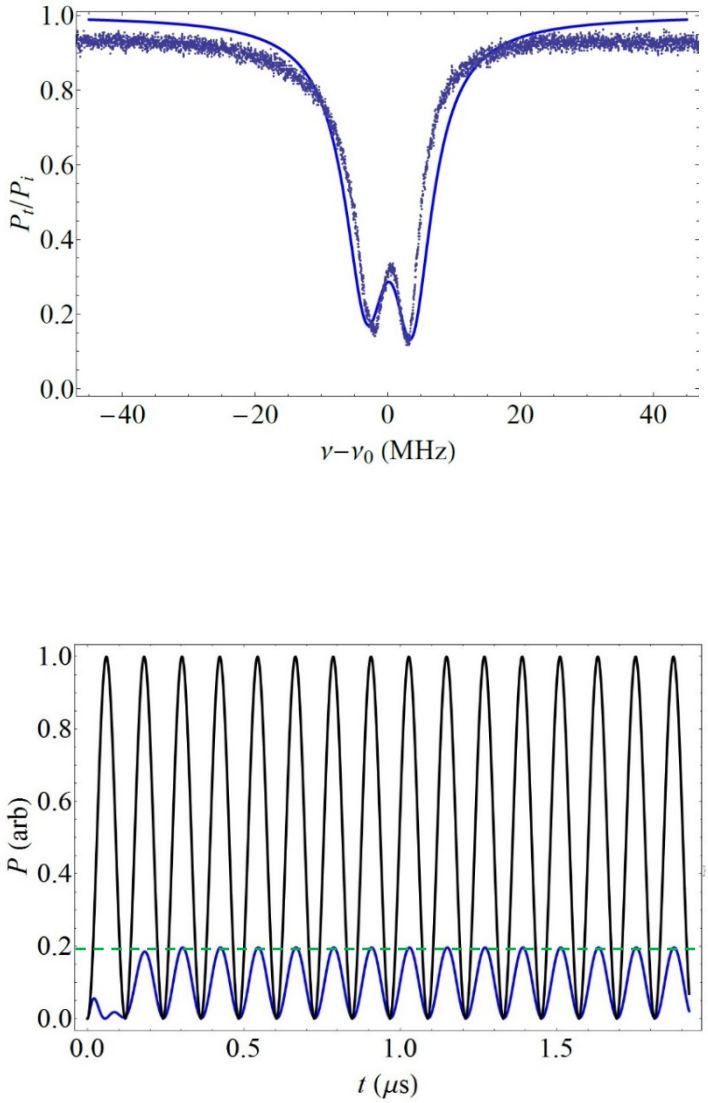

Figure 5.18. CMIT (TE input) with 200-μm-radius HBR.
Top: experimental throughput trace (gray) fitted with the model (blue) throughput spectra, which gives $T_s = 2.51 \times 10^{-8}$. Bottom: Modeled relative modulation amplitude of 0.20 corresponding to the fitted T_s. Mode parameters: $Q_1 = 1.6 \times 10^7$, $Q_2 = 9.7 \times 10^7$; $M_1 = 0.55$ (overcoupled), $M_2 = 0.42$ (undercoupled); detuning = -0.4 MHz. A minimum relative modulation amplitude of 0.19 was found (green dashed line) at 4.0 MHz using the AOM, giving $T_s = 2.29 \times 10^{-8}$.

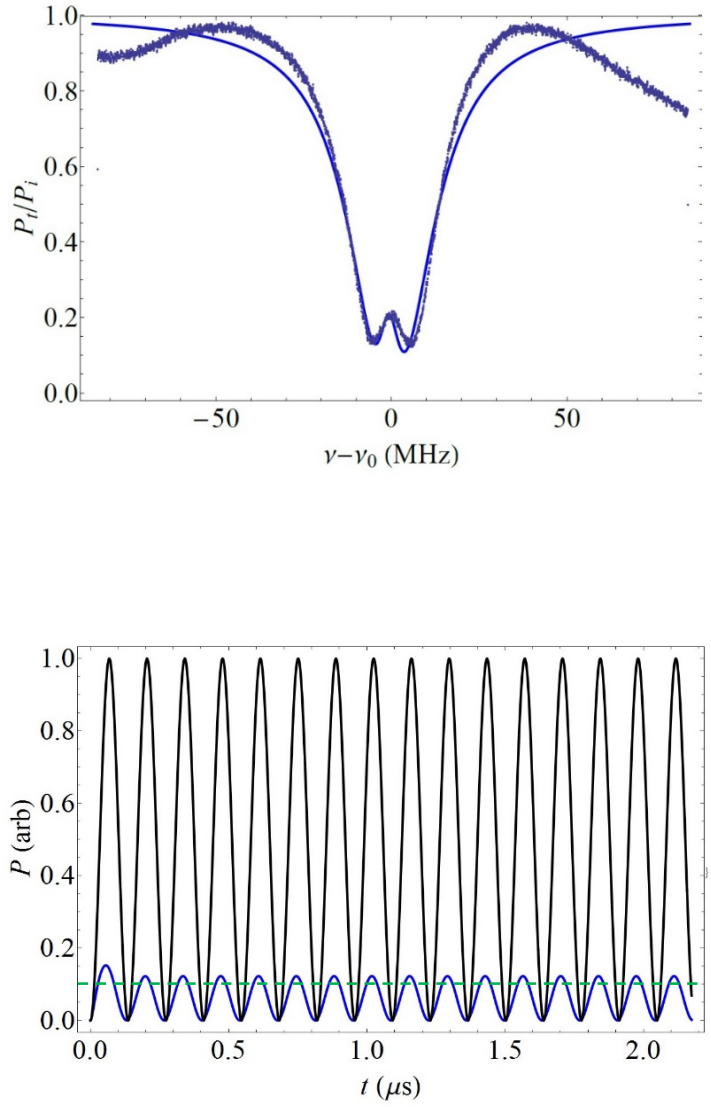

Figure 5.19. CMIT (TE input) with 180-μm-radius HBR.
Top: experimental throughput trace (gray) fit into the model (blue) throughput spectra, which gives $T_s = 1.58 \times 10^{-8}$. Bottom: Modeled relative modulation amplitude of 0.12 corresponding to the fitted T_s. Mode parameters: $Q_1 = 7.7 \times 10^6$, $Q_2 = 3.7 \times 10^7$; $M_1 = 0.94$ (undercoupled), $M_2 = 0.91$ (undercoupled); detuning = -0.8 MHz. A minimum relative modulation amplitude of 0.10 was found (green dashed line) at 4.5 MHz using the AOM, giving $T_s = 2.35 \times 10^{-8}$.

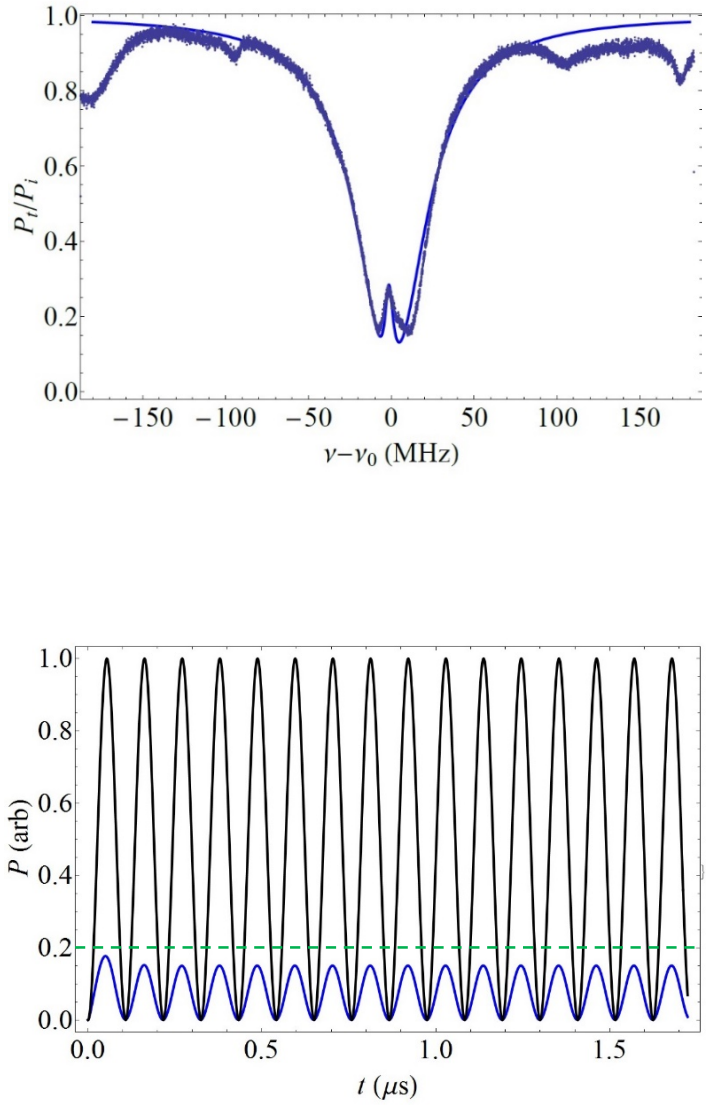

Figure 5.20. CMIT (TE input) with 180-μm-radius HBR.
Top: experimental throughput trace (gray) fit into the model (blue) throughput spectra, which gives $T_s = 2.51 \times 10^{-8}$. Bottom: Modeled relative modulation amplitude of 0.15 corresponding to the fitted T_s. Mode parameters: $Q_1 = 4.1 \times 10^6$, $Q_2 = 5.0 \times 10^7$; $M_1 = 0.89$ (undercoupled), $M_2 = 0.82$ (undercoupled); detuning = -1.6 MHz. A minimum relative modulation amplitude of 0.20 was found (green dashed line) at 5.0 MHz using the AOM, giving $T_s = 2.90 \times 10^{-8}$.

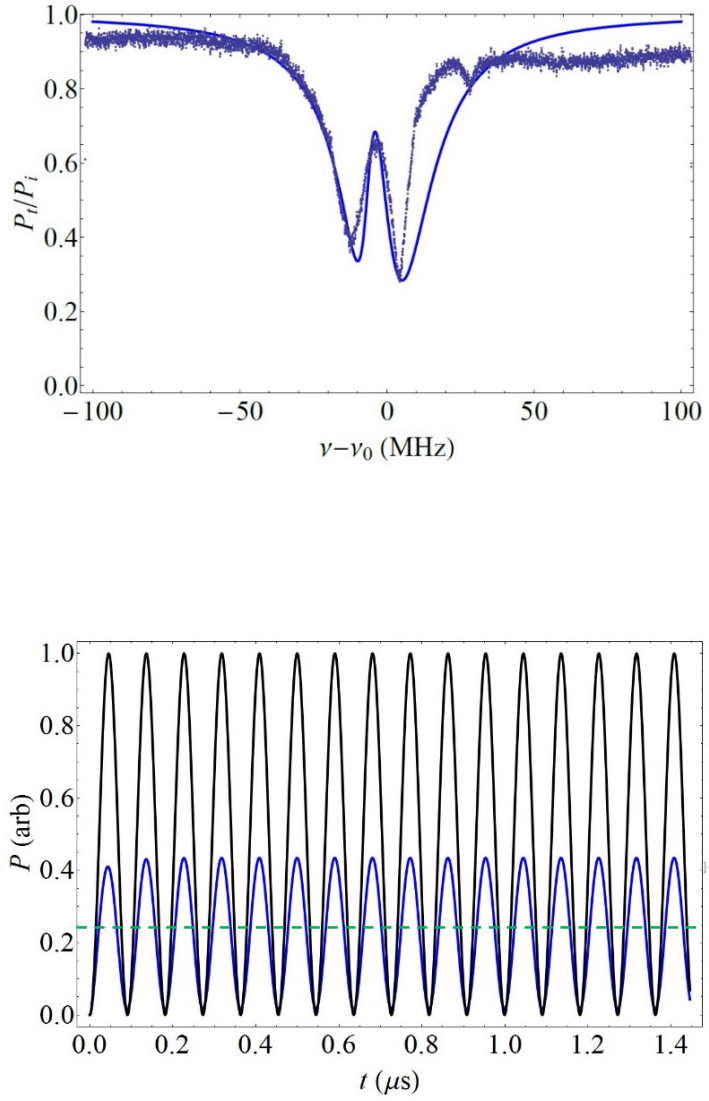

Figure 5.21. CMIT (TE input) with 190-μm-radius HBR.
Top: experimental throughput trace (gray) fit into the model (blue) throughput spectra, which gives $T_s = 3.98 \times 10^{-8}$. Bottom: Modeled relative modulation amplitude of 0.41 corresponding to the fitted T_s. Mode parameters: $Q_1 = 6.4 \times 10^6$, $Q_2 = 6.4 \times 10^7$; $M_1 = 0.74$ (undercoupled), $M_2 = 0.31$ (undercoupled); detuning = - 4.6 MHz. A minimum relative modulation amplitude of 0.24 was found (green dashed line) at 6.5 MHz using the AOM, giving $T_s = 5.45 \times 10^{-8}$.

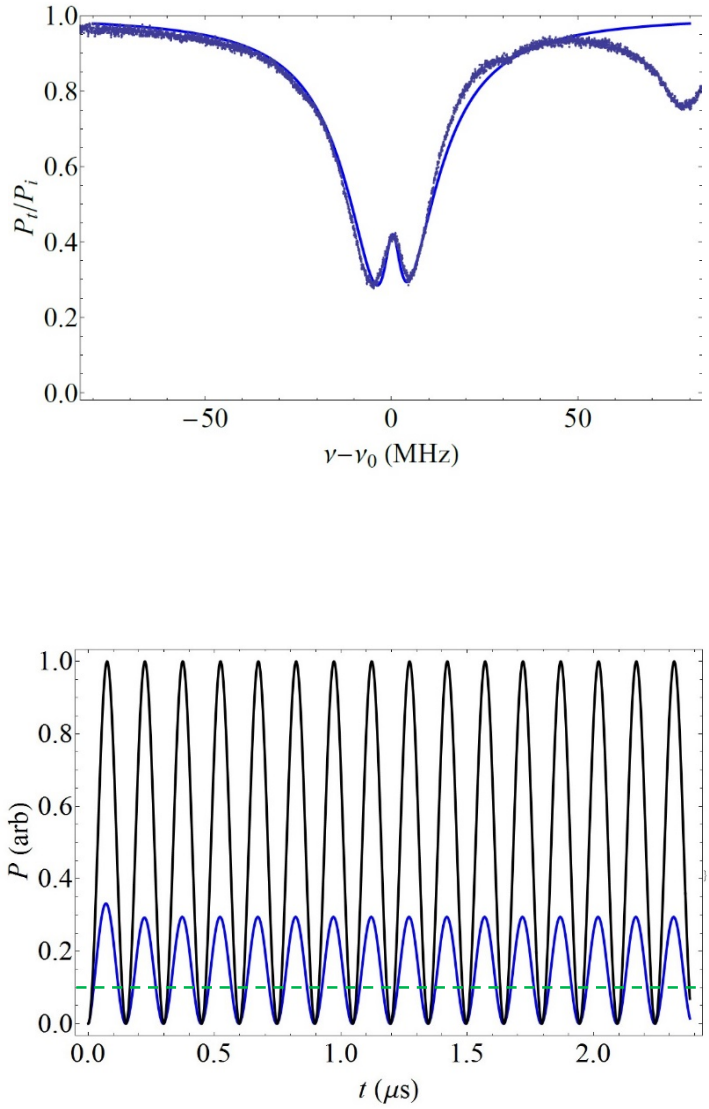

Figure 5.22. CMIT (TE input) with 180-μm-radius HBR.
Top: experimental throughput trace (gray) fit into the model (blue) throughput spectra, which gives $T_s = 1.26 \times 10^{-8}$. Bottom: Modeled relative modulation amplitude of 0.29 corresponding to the fitted T_s. Mode parameters: $Q_1 = 7.7 \times 10^6$, $Q_2 = 5.4 \times 10^7$; $M_1 = 0.76$ (undercoupled), $M_2 = 0.81$ (overcoupled); detuning = 0.4 MHz. A minimum relative modulation amplitude of 0.10 was found (green dashed line) at 6.5 MHz using the AOM, giving $T_s = 4.89 \times 10^{-8}$.

For TE input polarization, Figs. 5.23 – 5.30 show some experimental ATS throughput spectra (gray) fitted with model (blue) in the top figures; and the bottom figures show the modeled relative modulation amplitude (blue) corresponding to the fitted T_s compared to the minimum relative modulation amplitude (green dashed lines) found in the experiment. The results are presented with increasing modulation frequency of the AOM.

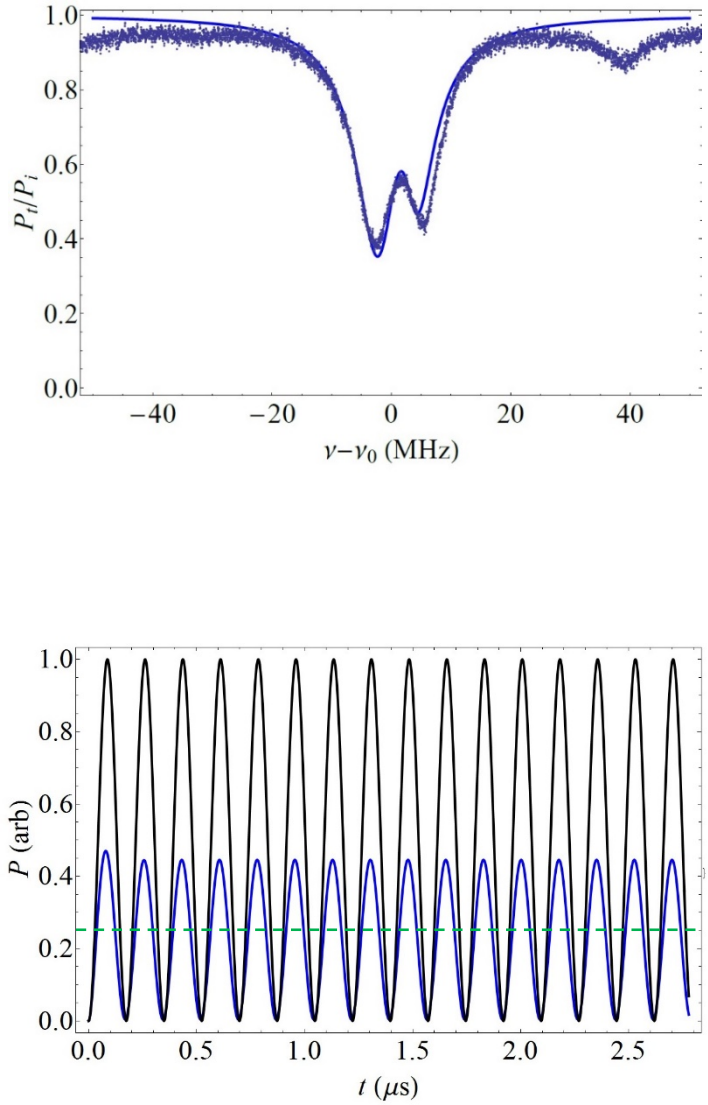

Figure 5.23. ATS (TE input) with 180-μm-radius HBR.
Top: experimental throughput trace (gray) fit into the model (blue) throughput spectra, which gives $T_s = 1.00 \times 10^{-8}$. Bottom: Modeled relative modulation amplitude of 0.44 corresponding to the fitted T_s. Mode parameters: $Q_1 = 1.9 \times 10^7$, $Q_2 = 5.3 \times 10^7$; $M_1 = 0.72$ (undercoupled), $M_2 = 0.34$ (overcoupled); detuning = 1.5 MHz. A minimum relative modulation amplitude of 0.25 was found (green dashed line) at 4.1 MHz using the AOM, giving $T_s = 1.95 \times 10^{-8}$.

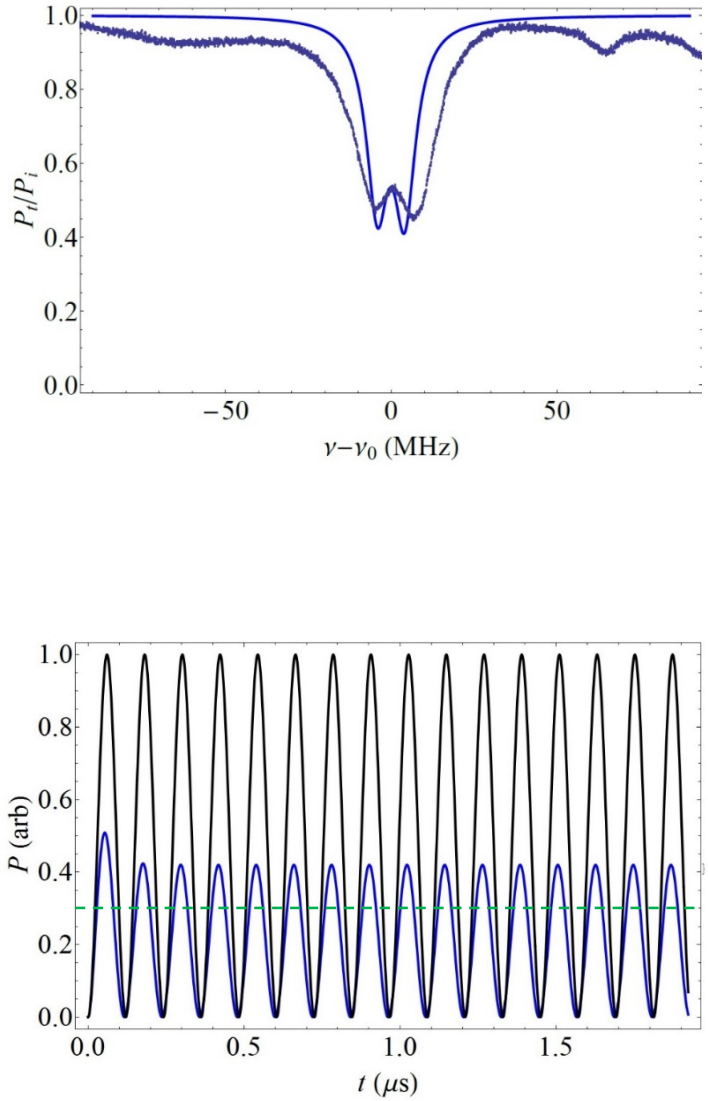

Figure 5.24. ATS (TE input) with 180-µm-radius HBR.
Top: experimental throughput trace (gray) fit into the model (blue) throughput spectra, which gives $T_s = 1.99 \times 10^{-8}$. Bottom: Modeled relative modulation amplitude of 0.4 corresponding to the fitted T_s. Mode parameters: $Q_1 = 2.3 \times 10^7$, $Q_2 = 2.9 \times 10^7$; $M_1 = 0.81$ (undercoupled), $M_2 = 0.67$ (undercoupled); detuning = -0.2 MHz. A minimum relative modulation amplitude of 0.30 was found (green dashed line) at 4.2 MHz using the AOM, giving $T_s = 2.04 \times 10^{-8}$.

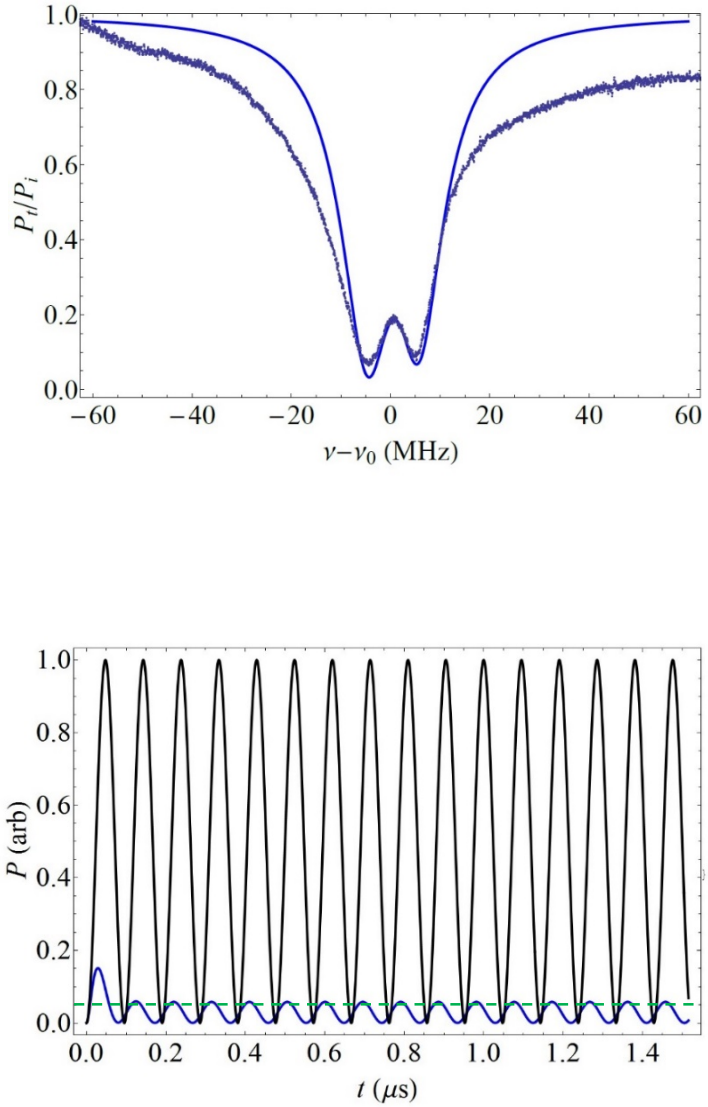

Figure 5.25. ATS (TE input) with 180-μm-radius HBR.
Top: experimental throughput trace (gray) fit into the model (blue) throughput spectra, which gives $T_s = 3.16 \times 10^{-8}$. Bottom: Modeled relative modulation amplitude of 0.05 corresponding to the fitted T_s. Mode parameters: $Q_1 = 1.3 \times 10^7$, $Q_2 = 2.7 \times 10^7$; $M_1 = 0.99$ (overcoupled), $M_2 = 0.72$ (undercoupled); detuning = 1.0 MHz. A minimum relative modulation amplitude of 0.05 was found (green dashed line) at 5.2 MHz using the AOM, giving $T_s = 3.13 \times 10^{-8}$.

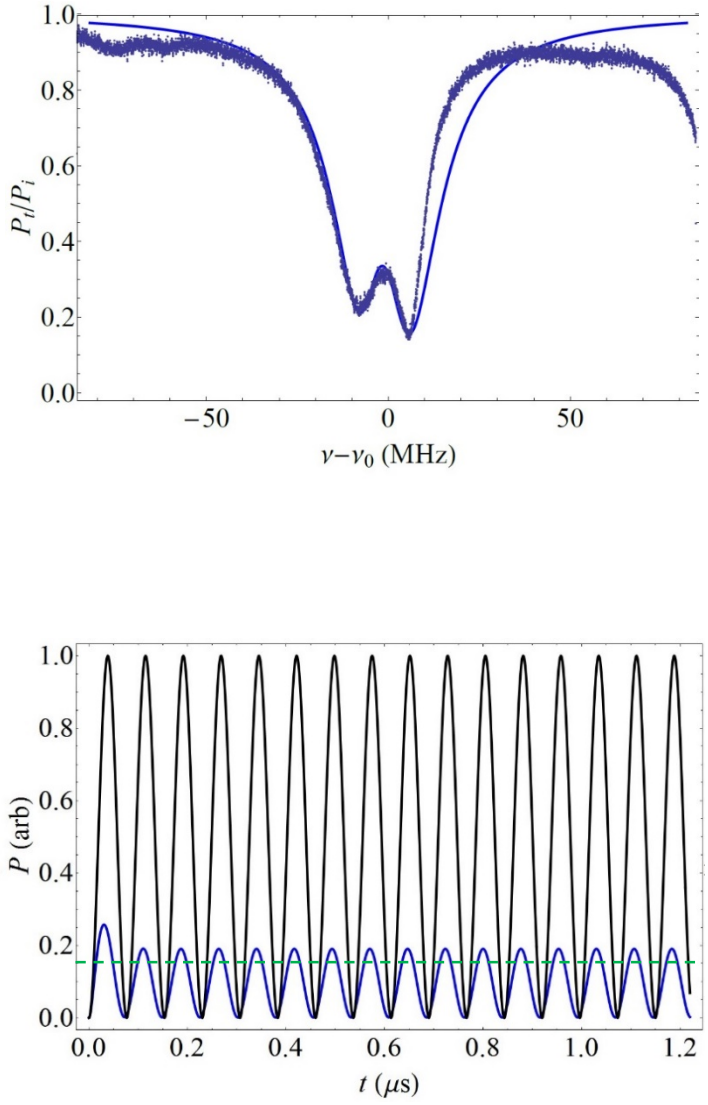

Figure 5.26. ATS (TE input) with 180-μm-radius HBR.
Top: experimental throughput trace (gray) fit into the model (blue) throughput spectra, which gives $T_s = 3.98 \times 10^{-8}$. Bottom: Modeled relative modulation amplitude of 0.18 corresponding to the fitted T_s. Mode parameters: $Q_1 = 8.0 \times 10^6$, $Q_2 = 2.3 \times 10^7$; $M_1 = 0.93$ (undercoupled), $M_2 = 0.72$ (undercoupled); detuning = -2.0 MHz. A minimum relative modulation amplitude of 0.15 was found (green dashed line) at 6.7 MHz using the AOM, giving $T_s = 5.21 \times 10^{-8}$.

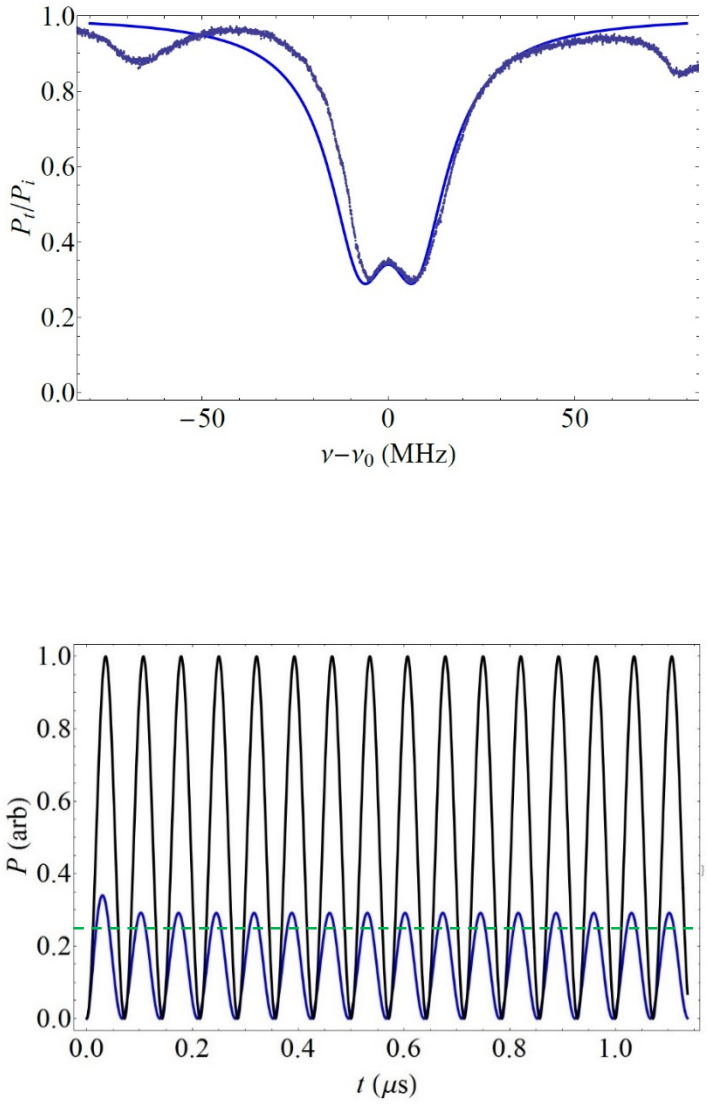

Figure 5.27. ATS (TE input) with 190-μm-radius HBR.
Top: experimental throughput trace (gray) fit into the model (blue) throughput spectra, which gives $T_s = 6.31 \times 10^{-8}$. Bottom: Modeled relative modulation amplitude of 0.28 corresponding to the fitted T_s. Mode parameters: $Q_1 = 8.5 \times 10^6$, $Q_2 = 1.4 \times 10^7$; $M_1 = 0.87$ (undercoupled), $M_2 = 0.81$ (undercoupled); detuning = 0 MHz. A minimum relative modulation amplitude of 0.25 was found (green dashed line) at 7.2 MHz using the AOM, giving $T_s = 6.69 \times 10^{-8}$.

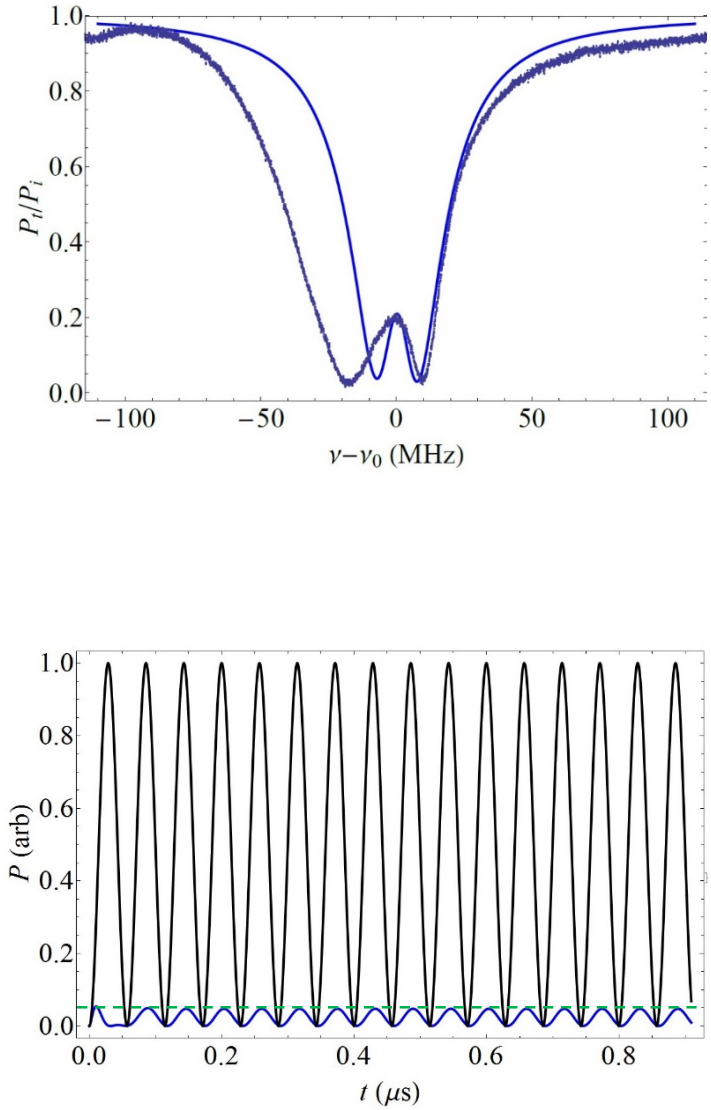

Figure 5.28. ATS (TE input) with 190-μm-radius HBR.
Top: experimental throughput trace (gray) fit into the model (blue) throughput spectra, which gives $T_s = 1.00 \times 10^{-7}$. Bottom: Modeled relative modulation amplitude of 0.05 corresponding to the fitted T_s. Mode parameters: $Q_1 = 5.8 \times 10^6$, $Q_2 = 3.7 \times 10^7$; $M_1 = 0.85$ (overcoupled), $M_2 = 0.72$ (undercoupled); detuning = 0.5 MHz. A minimum relative modulation amplitude of 0.05 was found (green dashed line) at 8.5 MHz using the AOM, giving $T_s = 9.30 \times 10^{-8}$.

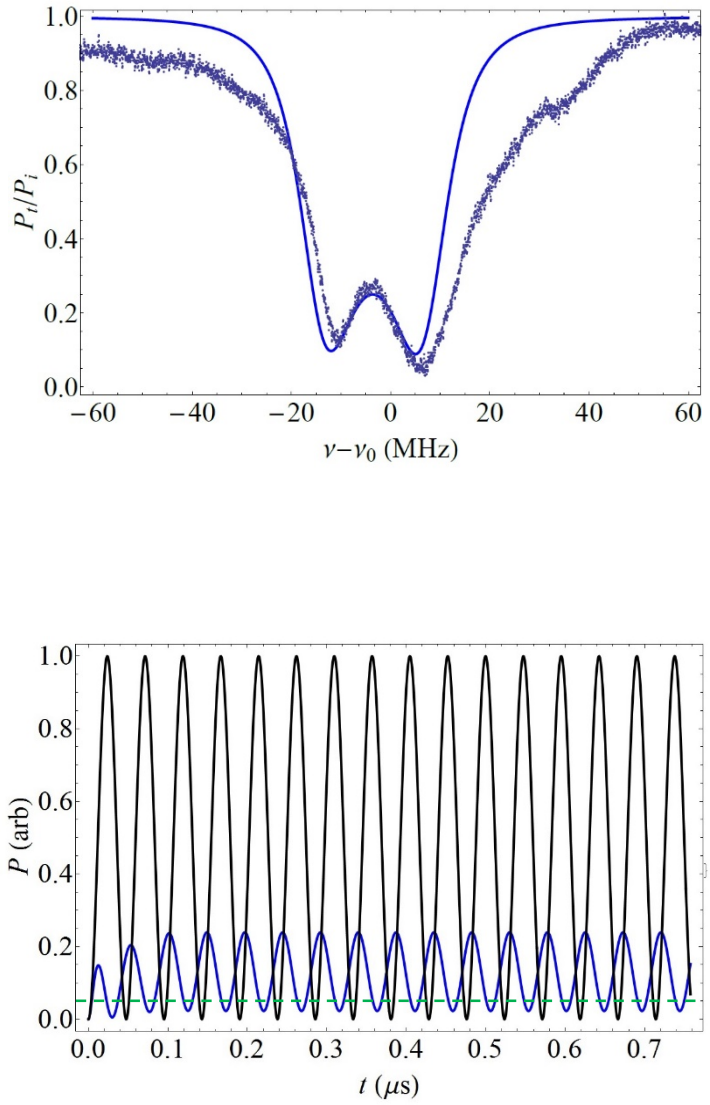

Figure 5.29. ATS (TE input) with 180-µm-radius HBR.
Top: experimental throughput trace (gray) fitted with the model (blue) throughput spectra, which gives $T_s = 1.26 \times 10^{-7}$. Bottom: Modeled relative modulation amplitude of 0.25 corresponding to the fitted T_s. Mode parameters: $Q_1 = 1.3 \times 10^7$, $Q_2 = 1.4 \times 10^7$; $M_1 = 0.17$ (overcoupled), $M_2 = 0.85$ (undercoupled); detuning = -7 MHz. A minimum relative modulation amplitude of 0.05 was found (green dashed line) at 9.0 MHz using the AOM, giving $T_s = 9.40 \times 10^{-8}$.

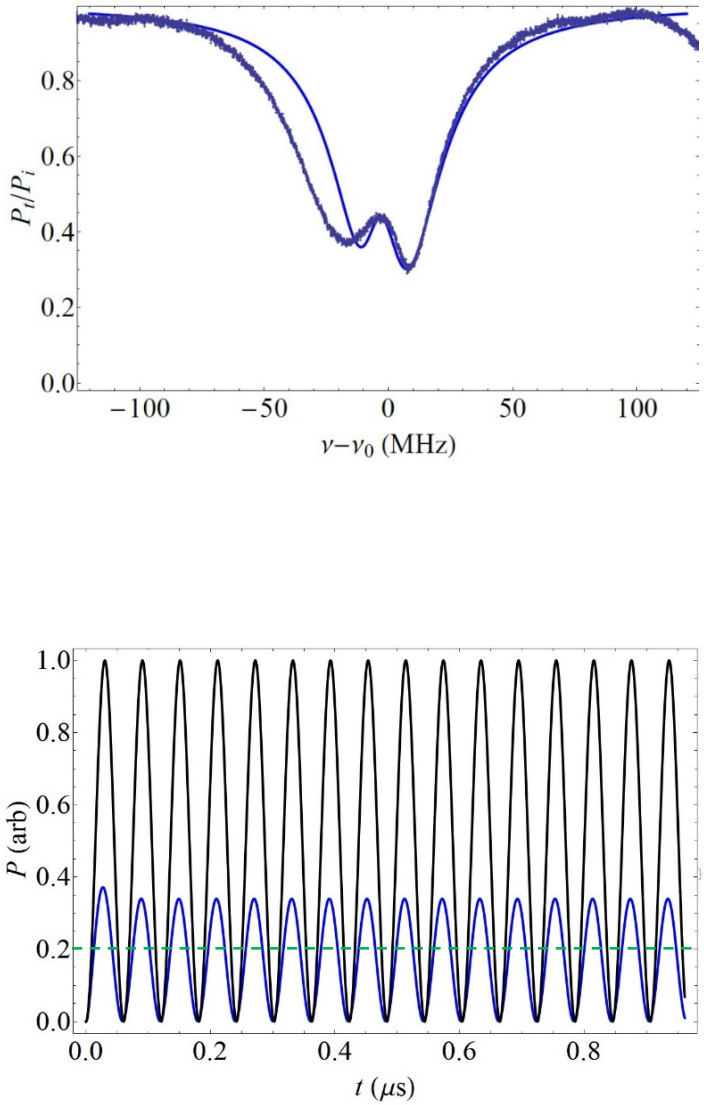

Figure 5.30. ATS (TE input) with 200-μm-radius HBR.
Top: experimental throughput trace (gray) fit into the model (blue) throughput spectra, which gives $T_s = 1.00 \times 10^{-7}$. Bottom: Modeled relative modulation amplitude of 0.33 corresponding to the fitted T_s. Mode parameters: $Q_1 = 5.0 \times 10^6$, $Q_2 = 1.6 \times 10^7$; $M_1 = 0.77$ (undercoupled), $M_2 = 0.68$ (undercoupled); detuning = -3.5 MHz. A minimum relative modulation amplitude of 0.20 was found (green dashed line) at 9.5 MHz using the AOM, giving $T_s = 1.29 \times 10^{-7}$.

Now, let's look at some cases when the input has TM polarization. Fig. 5.31 shows an experimental CMIT throughput spectrum (gray) fitted with model (blue) in the top figure; and the bottom figure shows the modeled relative modulation amplitude (blue) corresponding to the fitted T_s compared to the minimum relative modulation amplitude (green dashed lines) found in the experiment.

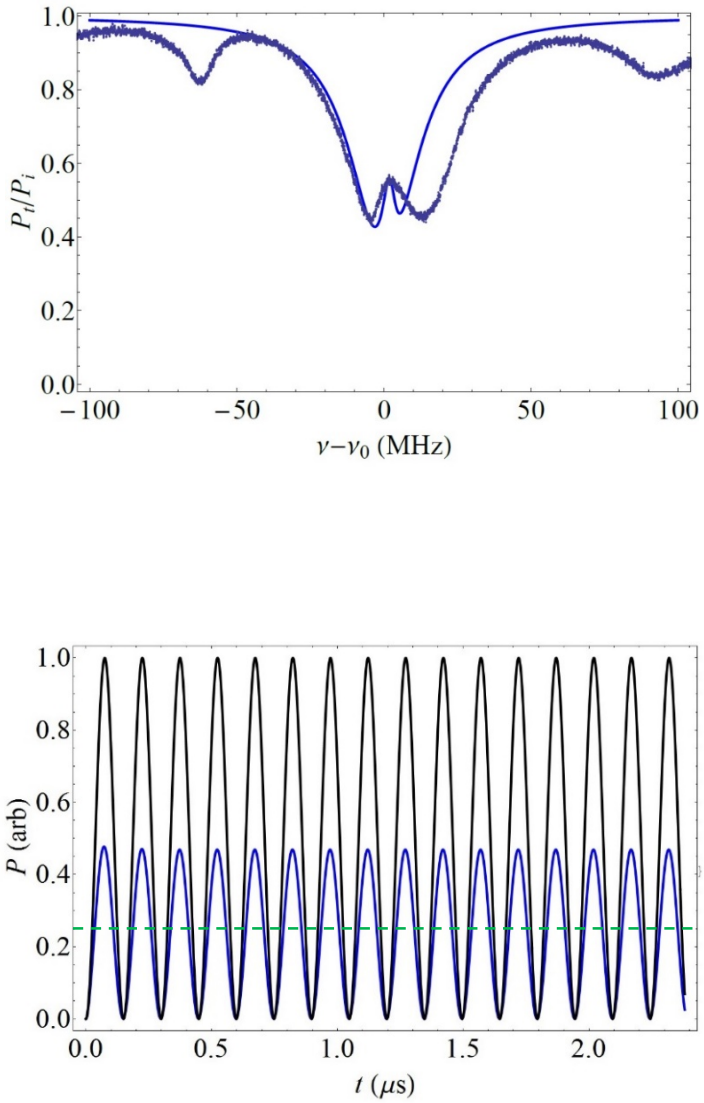

Figure 5.31. CMIT (TM input) with 180-μm-radius HBR.
Top: experimental throughput trace (gray) fit into the model (blue) throughput spectra, which gives $T_s = 1.26 \times 10^{-8}$. Bottom: Modeled relative modulation amplitude of 0.47 corresponding to the fitted T_s. Mode parameters: $Q_1 = 7.5 \times 10^6$, $Q_2 = 5.3 \times 10^7$; $M_1 = 0.60$ (undercoupled), $M_2 = 0.73$ (undercoupled); detuning = 2.0 MHz. A minimum relative modulation amplitude of 0.25 was found (green dashed line) at 4.8 MHz using the AOM, giving $T_s = 2.67 \times 10^{-8}$.

For TM input polarization, Figs. 5.32 – 5.35 show some experimental ATS throughput spectrum (gray) fitted with model (blue) in the top figures; and the bottom figures show the modeled relative modulation amplitude (blue) corresponding to the fitted T_s compared to the minimum relative modulation amplitude (green dashed lines) found in the experiment. The results are presented with increasing modulation frequency of the AOM.

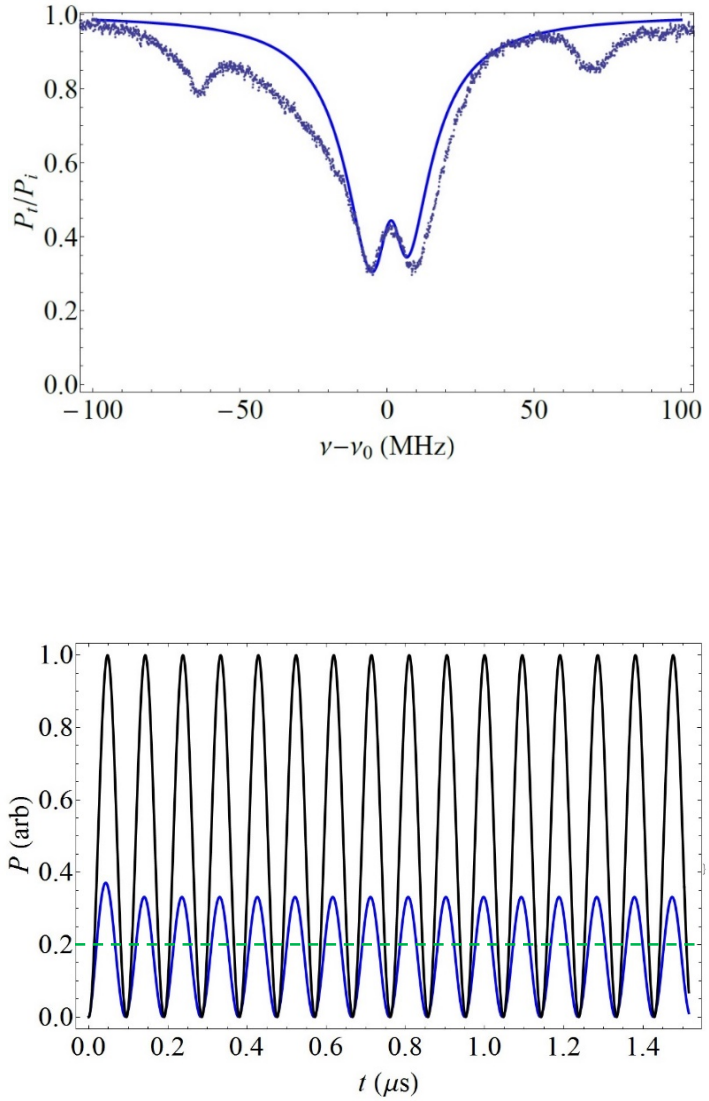

Figure 5.32. ATS (TM input) with 180-μm-radius HBR.
Top: experimental throughput trace (gray) fit into the model (blue) throughput spectra, which gives $T_s = 3.16 \times 10^{-8}$. Bottom: Modeled relative modulation amplitude of 0.33 corresponding to the fitted T_s. Mode parameters: $Q_1 = 7.6 \times 10^6$, $Q_2 = 2.7 \times 10^7$; $M_1 = 0.77$ (undercoupled), $M_2 = 0.64$ (undercoupled); detuning = 1.6 MHz. A minimum relative modulation amplitude of 0.20 was found (green dashed line) at 6.1 MHz using the AOM, giving $T_s = 4.30 \times 10^{-8}$.

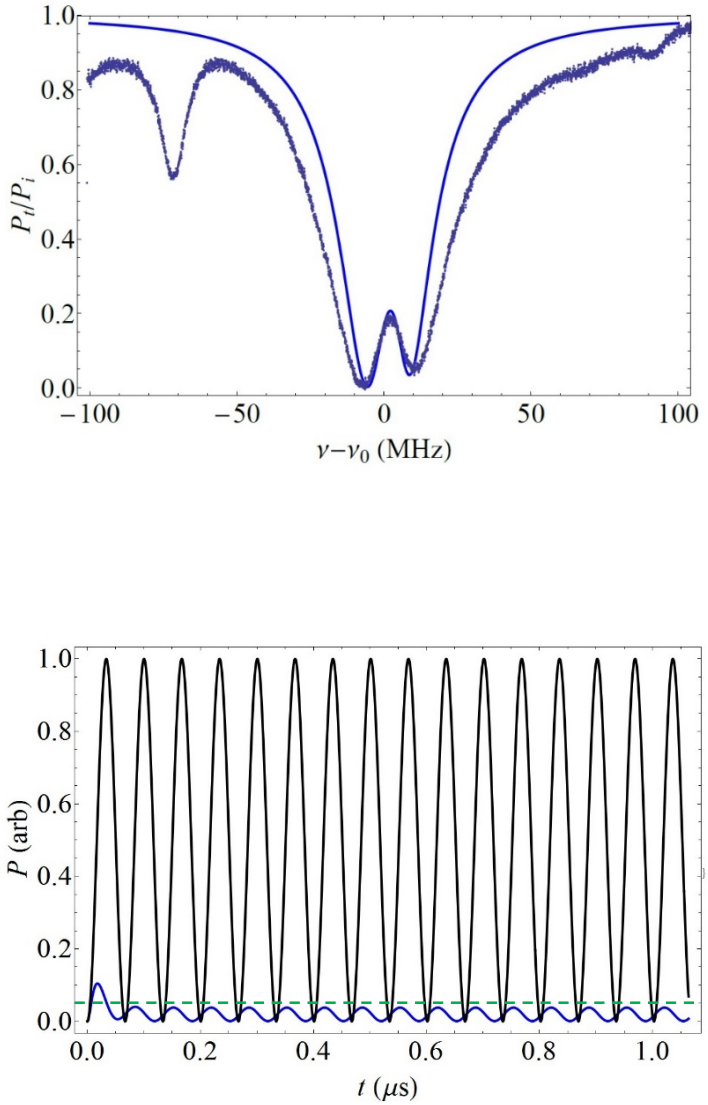

Figure 5.33. ATS (TM input) with 200-μm-radius HBR.
Top: experimental throughput trace (gray) fit into the model (blue) throughput spectra, which gives $T_s = 6.31 \times 10^{-8}$. Bottom: Modeled relative modulation amplitude of 0.03 corresponding to the fitted T_s. Mode parameters: $Q_1 = 7.0 \times 10^6$, $Q_2 = 2.7 \times 10^7$; $M_1 = 0.99$ (overcoupled), $M_2 = 0.71$ (undercoupled); detuning = 3.0 MHz. A minimum relative modulation amplitude of 0.05 was found (green dashed line) at 7.5 MHz using the AOM, giving $T_s = 8.07 \times 10^{-8}$.

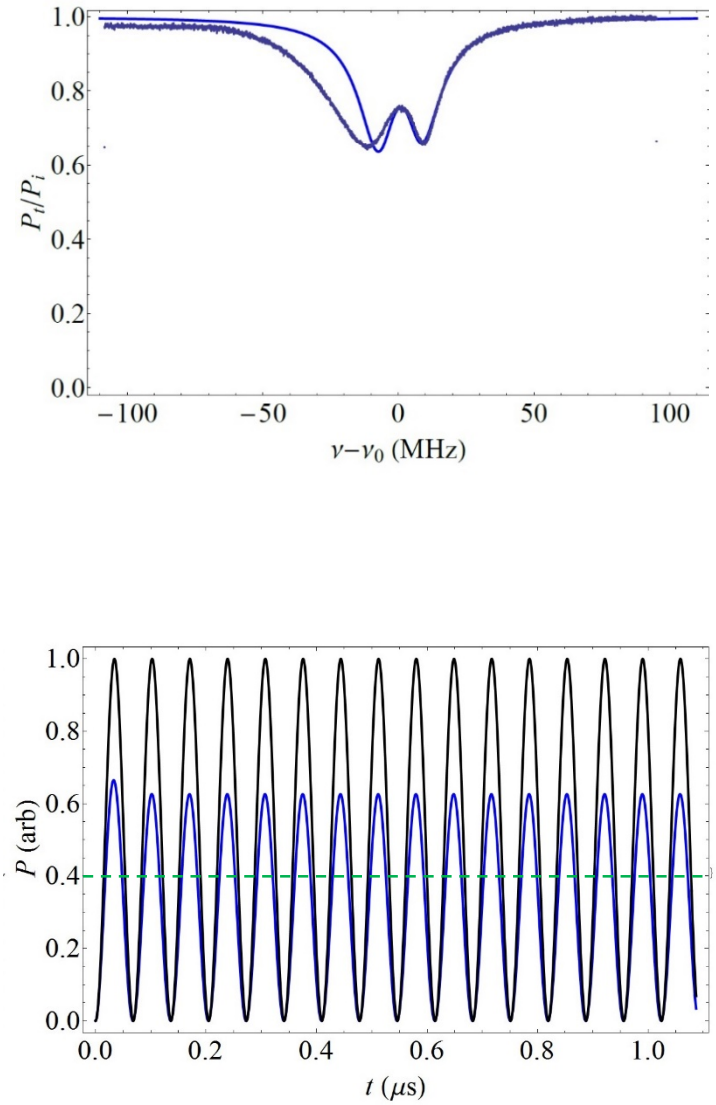

Figure 5.34. ATS (TM input) with 180-μm-radius HBR.
Top: experimental throughput trace (gray) fit into the model (blue) throughput spectra, which gives $T_s = 6.31 \times 10^{-8}$. Bottom: Modeled relative modulation amplitude of 0.63 corresponding to the fitted T_s. Mode parameters: $Q_1 = 9.4 \times 10^6$, $Q_2 = 2.0 \times 10^7$; $M_1 = 0.46$ (undercoupled), $M_2 = 0.75$ (overcoupled); detuning = 1.2 MHz. A minimum relative modulation amplitude of 0.40 was found (green dashed line) at 9.5 MHz using the AOM, giving $T_s = 1.05 \times 10^{-7}$.

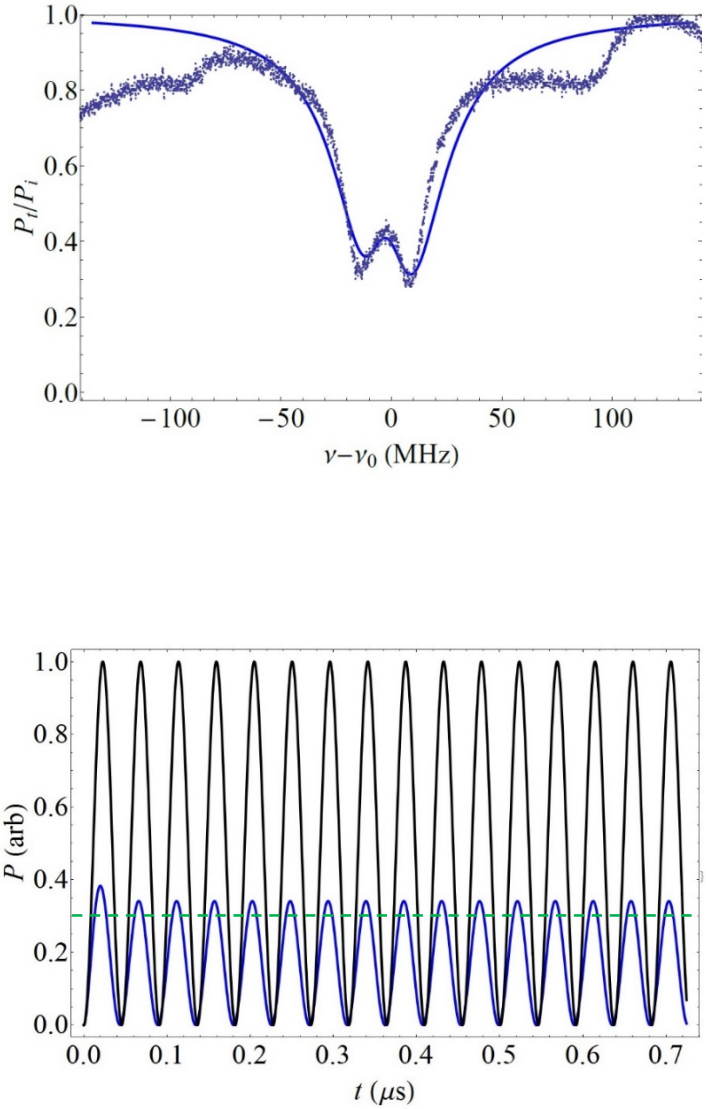

Figure 5.35. ATS (TM input) with 190-µm-radius HBR.
Top: experimental throughput trace (gray) fit into the model (blue) throughput spectra, which gives $T_s = 1.26 \times 10^{-7}$. Bottom: Modeled relative modulation amplitude of 0.35 corresponding to the fitted T_s. Mode parameters: $Q_1 = 4.5 \times 10^6$, $Q_2 = 1.1 \times 10^7$; $M_1 = 0.78$ (undercoupled), $M_2 = 0.94$ (overcoupled); detuning = -3.0 MHz. A minimum relative modulation amplitude of 0.30 was found (green dashed line) at 10 MHz using the AOM, giving $T_s = 1.29 \times 10^{-7}$.

The uncertainty in $\log(T_s)$ is 0.1 in all the fitting done in the cases shown here. This means the T_s found by fitting has an uncertainty of 25%. The uncertainty in the modulation frequency v is about 0.1 MHz. From $v = \Omega/2\pi$ and $\Omega_{\min}{}^2 = \frac{T_s}{\tau_{rt}{}^2}$, we can estimate the corresponding uncertainty in T_s ranges from 6% to 2% as v ranges from 3.5 MHz to 10 MHz. However, other effects (described later) suggests that a better estimate of the uncertainty in the T_s found by modulation is 25%.

The percent difference is defined as: $\frac{T_s{}^{ampl} - T_s{}^{fit}}{(T_s{}^{ampl} + T_s{}^{fit})/2} \times 100\%$, where $T_s{}^{fit}$ is the coupling strength obtained by model fitting and $T_s{}^{ampl}$ is the coupling strength found from amplitude modulation. Then we can calculate the percent difference between the two estimated values of T_s for each case. Then we can make a comparison as in Table 3.

Table 3. Comparing the values of T_s from numerical fitting and from amplitude modulation.

Modulation frequency (ν_{min} = $\Omega_{min}/2\pi$)	**Effect**	**Q values (Q_1), (Q_2)**	**T_s (±25%) (model fitting)**	**T_s (±25%) (amplitude modulation)**	**%diff.**
3.5 MHz	CMIT	(1.5×10^7), (8.6×10^7)	1.26×10^{-8}	2.11×10^{-8}	50.4%
4.0 MHz	CMIT	(9.6×10^6), (5.2×10^7)	1.99×10^{-8}	2.29×10^{-8}	14.0%
4.0 MHz	CMIT	(1.6×10^7), (9.7×10^7)	2.51×10^{-8}	2.29×10^{-8}	-9.2%
4.5 MHz	CMIT	(7.7×10^6), (3.7×10^7)	1.58×10^{-8}	2.35×10^{-8}	39.2%
5.0 MHz	CMIT	(4.1×10^6), (5.0×10^7)	2.51×10^{-8}	2.90×10^{-8}	14.4%
6.5 MHz	CMIT	(6.4×10^6), (6.4×10^7)	3.98×10^{-8}	5.45×10^{-8}	31.2%
6.5 MHz	CMIT	(7.7×10^6), (5.4×10^7)	1.26×10^{-8}	4.89×10^{-8}	118.0%
4.1 MHz	ATS	(1.9×10^6), (5.3×10^7)	1.00×10^{-8}	1.95×10^{-8}	64.4 %
4.2 MHz	ATS	(2.3×10^7), (2.9×10^7)	1.99×10^{-8}	2.04×10^{-8}	2.5%
5.2 MHz	ATS	(1.3×10^7), (2.7×10^7)	3.16×10^{-8}	3.13×10^{-8}	-1.0%
6.7 MHz	ATS	(8.0×10^6), (2.3×10^7)	3.98×10^{-8}	5.21×10^{-8}	26.8%
7.2 MHz	ATS	(8.5×10^6), (1.4×10^7)	6.31×10^{-8}	6.69×10^{-8}	5.8%
8.5 MHz	ATS	(5.8×10^6), (3.7×10^7)	1.00×10^{-7}	9.30×10^{-8}	-7.3%
9.0 MHz	ATS	(1.3×10^7), (1.4×10^7)	1.26×10^{-7}	9.40×10^{-8}	-29.1%
9.5 MHz	ATS	(5.0×10^6), (1.6×10^7)	1.00×10^{-7}	1.29×10^{-7}	25.3%
4.8 MHz	CMIT	(7.5×10^6), (5.3×10^7)	1.26×10^{-8}	2.67×10^{-8}	71.8%
6.1 MHz	ATS	(7.6×10^6), (2.7×10^7)	3.16×10^{-8}	4.30×10^{-8}	30.6%
7.5 MHz	ATS	(7.0×10^6), (2.7×10^7)	6.31×10^{-8}	8.07×10^{-8}	24.5%
9.5 MHz	ATS	(9.4×10^6), (2.0×10^7)	6.31×10^{-8}	1.05×10^{-7}	49.9%
10.0 MHz	ATS	(4.5×10^6), (1.1×10^7)	1.26×10^{-7}	1.29×10^{-7}	2.4%

Out of the results, those with percent difference less than 40% are within the expected experimental uncertainty (15 out of 20 cases). For most cases of ATS, the two values of CPC strength for each case agree well, with only a small percent difference. We also had some good agreements for CMIT cases. Even for the cases that had percent difference of greater than 40%, because CPC from TE to TM can have a different strength from the CPC from TM to TE, the results might be in good agreement.

Based on these results, we can say that we have developed an independent method of estimating the CPC strength, by amplitude modulation (without the need to fit into a computer model).

So far we have three different methods for finding the CPC strength. First method is by fitting the experimental throughput spectra to a computational model to infer the CPC strength indirectly; second method is a theoretical calculation of CPC strength based on the transverse structure of WGMs [38]; and the third method is directly estimating the CPC strength from the response of the throughput amplitude to a sinusoidal modulation, which is presented in this dissertation. All three methods give us about same order of magnitude of the CPC strength. Before us, no one even knew what order of magnitude the CPC strength should be.

Here, for the cases of CMIT and ATS, most of our results gave the same order of magnitude for the values of the CPC strength. But we had better agreements for the cases of ATS than for the cases of CMIT. There might be several reasons for this trend of disagreement. First, the CMIT feature itself is hard to observe given the level of mode overlap in our experiment. Second, our measurements of the mode parameters may not be accurate enough (for example, coupling regimes). Third, the AOM we used in the modulation experiments has a finite response time, so the modulation signal may have been distorted for the higher frequencies, making it harder for us to observe the modulation amplitude.

In addition to the potential experimental difficulties noted above, two assumptions made in the analysis of Chapter IV may be violated in some cases. We assumed $Q_2 >> Q_1$, but in many of the examples of Table 3, this is not true and the value of T_s found by amplitude modulation may be too low since then κ_2^2 cannot be neglected in Eq. (4.28). Also, it may be the case that the modulation frequencies for zero phase and minimum throughput amplitude are not always equal. Further investigation needs to be done on these two points. Another potential problem is discussed in the next chapter.

CHAPTER VI

CONCLUSIONS

6.1. Summary

The coupling effect between orthogonally polarized modes in a single resonator can lead to CMIT/CMIA or to ATS. These effects enable slow light or fast light and have potential applications, which make it important for us to get a clear understanding of the dynamics of the CPC. Previously, the intermode coupling strength was determined by fitting the experimental throughput spectra to a Mathematica model. Now the modulation response gives us an independent way to find the value of the CPC strength T_s. Being able to determine the intermode coupling strength without model fitting may help us to get a better understanding of the dynamics of the CPC effect in microresonators. In particular, a good understanding of the exceptional point, where the IT – ATS transition takes place, may enhance slow light and sensing applications of microresonators. We also expect other applications to be improved with the help of our dynamics study.

6.2. Future Work

As we mentioned in Chapter V, some of the experimental results in the cases of CMIT don't agree with the model prediction to within the expected uncertainty, but the disagreements are not large (say, greater than a factor of 2). Some possible reasons were discussed in the previous chapter.

It has recently been shown [38] that the CPC from TE to TM can have a different strength from the CPC from TM to TE, and because of this the values of T_s found by fitting and by modulation can be different. A revised model is currently being investigated in our lab, and this may help to resolve some of the disagreement in the results presented in Table 3. Thus we plan to do further CMIT/ATS experiments to test the revised model and try to determine the two CPC strengths separately.

Other experimental goals are to further reduce mode overlap, and find cases with $Q_2 >> Q_1$ and relatively low $v_{\min}$. The results from further CMIT/ATS experiments testing the revised model will be compared to expectations from the analytical analysis in order to predict which parameter ranges should enhance experimental observation of the CPC effects.

REFERENCES

[1] L. Rayleigh, “The problem of the whispering gallery,” Phil. Mag. **20**, 1001–1004 (1910).

[2] C. G. Garrett, W. Kaiser, and W. L. Bond, "Stimulated Emission into Optical Whispering Modes of Spheres," Phys. Rev. **1**, 1807-1809 (1961).

[3] H. M. Tzeng, K. F. Wall, M. B. Long, and R. K. Chang, "Laser-Emission from Individual Droplets at Wavelengths Corresponding to Morphology-Dependent Resonances," Opt. Lett. **9**, 499-501 (1984).

[4] H. B. Lin, A. L. Huston, B. L. Justus, and A. J. Campillo, "Some Characteristics of a Droplet Whispering-Gallery-Mode Laser," Opt. Lett. **11**, 614-616 (1986).

[5] J. B. Snow, S. X. Qian, and R. K. Chang, "Stimulated Raman-Scattering from Individual Water and Ethanol Droplets at Morphology-Dependent Resonances," Opt. Lett. **10**, 37-39 (1985).

[6] S. X. Qian, J. B. Snow, and R. K. Chang, "Coherent Raman Mixing and Coherent Anti-Stokes Raman-Scattering from Individual Micrometer-Size Droplets," Opt. Lett. **10**, 499-501 (1985).

[7] V. B. Braginsky, M. L. Gorodetsky, and V. S. Ilchenko, “Quality factor and nonlinear properties of optical whispering-gallery modes,” Phys. Lett. A **137**, 393–397 (1989).

[8] K. J. Vahala, “Optical microcavities,” Nature **424**, 839-846 (2003)

[9] https://www.ijs.si/ijs/dept/f5-softmatter/images/wgm_reprensetation.jpg. (2019).

[10] V. V. Vassiliev, V. L. Velichansky, V. S. Ilchenko, M. L. Gorodetsky, L. Hollberg, and A. V. Yarovitsky, "Narrow-line-width diode laser with a high-Q microsphere resonator," Opt Commun **158**, 305-312 (1998).

[11] M. J. Humphrey, E. Dale, A. T. Rosenberger, and D. K. Bandy, "Calculation of optimal fiber radius and whispering-gallery mode spectra for a fiber-coupled microsphere," Opt. Commun. **271**, 124-131 (2007).

[12] E. Hecht and A. Zajac, Optics, 2nd ed. (Addison-Wesley Pub. Co., Reading, Mass., 1987).

[13] I. Teraoka, S. Arnold, and F. Vollmer, "Perturbation approach to resonance shifts of whispering-gallery modes in a dielectric microsphere as a probe of a surrounding medium," J. Opt. Soc. Am. B **20**, 1937-1946 (2003).

[14] N. M. Hanumegowda, C. J. Stica, B. C. Patel, I. White and X. Fan, "Refractometric sensors based on microsphere resonators," Appl. Phys. Lett. **87**, 201107 (2005).

[15] G. Farca, S. I. Shopova, and A. T. Rosenberger, "Cavity-enhanced laser absorption spectroscopy using microresonator whispering-gallery modes," Opt. Express **15**, 17443-17448 (2007).

[16] A. T. Rosenberger, "Analysis of whispering-gallery microcavity enhanced chemical absorption sensors," Opt. Express **15**, 12959-12964 (2007).

[17] A. M. Armani and K. J. Vahala, "Heavy water detection using ultra-high-Q microcavities," Opt. Lett. **31**, 1896-1898 (2006).

[18] D. Ganta, E. B. Dale, J. P. Rezac, and A. T. Rosenberger, "Optical method for measuring thermal accommodation coefficients using a whispering-gallery microresonator," J. Chem. Phys. **135**, 084313 (2011).

[19] M. Fleischhauer, A. Imamoglu, and J. P. Marangos, “Electromagnetically induced transparency: Optics in Coherent Media,” Rev. Mod. Phys. **77**, 633-673 (2005).

[20] S.E. Harris, J.E.Field and A. Imamoglu, “Nonlinear Optical Processes Using Electromagnetically Induced Transparency,” Phys. Rev. Lett. **64**, 1107-1110 (1990).

[21] K.-J. Boller, A. Imamoglu, and S.E. Harris, “Observation of Electromagnetically Induced Transparency,” Phys. Rev. Lett. **66**, 2593-2596 (1991).

[22] R. W. Boyd, “TOPICAL REVIEW Slow and fast light: fundamentals and applications,” J. Mod. Opt. **56**, 1908-1915 (2009).

[23] S. H. Autler, and C. H. Townes, “Stark effect in rapidly varying fields,” Phys. Rev. **100**, 703-722 (1955).

[24] B. Peng, Ş. K. Özdemir, W. Chen, F. Nori, and L. Yang, “What is and what is not electromagnetically induced transparency in whispering-gallery microcavities,” Nat. Commun. **5**, 5082 (2014).

[25] D. D. Smith, H. Chang, K. A. Fuller, A. T. Rosenberger, and R. W. Boyd, “Coupled resonator induced transparency,” Phys. Rev. A **69**, 063804 (2004).

[26] A. Naweed, G. Farca, S. I. Shopova, and A. T. Rosenberger, “Induced transparency and absorption in coupled whispering-gallery microresonators,” Phys. Rev. A **71**, 043804 (2005).

[27] E. B. Dale, *Coupling Effects in Dielectric Microcavities*, PhD dissertation, Oklahoma State University, 2010.

[28] A. T. Rosenberger, “EIT analogs using orthogonally polarized modes of a single whispering-gallery microresonator,” Proc. SPIE **8636**, 863602 (2013).

[29] K. V. Bui and A. T. Rosenberger, “Experimental study of induced transparency or absorption and slow or fast light using orthogonally polarized whispering-gallery modes of a single microresonator,” Proc. SPIE **9763**, 97630W (2016).

[30] K. V. Bui, *Induced Transparency and Pulse Delay Plus Induced Absorption and Pulse Advancement Using the Orthogonally Polarized Whispering Gallery Modes of a Single Microresonator*, PhD dissertation, Oklahoma State University, 2016.

[31] A. T. Rosenberger, “Comparison of methods for achieving induced transparency or absorption with pulse delay or advancement in a single microresonator,” Proc. SPIE **9763**, 97631E (2016).

[32] Y. Yang, S. Saurabh, J, Ward, and S. N. Chormaic, “Coupled-mode-induced transparency in aerostatically tuned microbubble whispering-gallery resonators,” Opt. Lett.**40**, 1834–1837 (2015).

[33] C. Dong, C. Zou, Y. Xiao, J. Cui, Z. Han, and G. Guo, “Modified transmission spectrum induced by two-mode interference in a single silica microsphere,” J. Phys. B **42**, 215401 (2009).

[34] B. Li, Y. Xiao, C. Zou, Y. Liu, X. Jiang, Y. Chen, Y. Li, and Q. Gong, “Experimental observation of Fano resonance in a single whispering-gallery microresonator,” Appl. Phys. Lett. **98**, 021116 (2011).

[35] H. Goldstein, C. Poole, and J. Safko, *Classical Mechanics, 3nd ed*. (Addison-Wesley, Reading, MA, 2000), Chap. 6.

[36] C. Mi, S. Chen, X. Zhou, K. Tian, H. Luo, and S. Wen, “Observation of tiny polarization rotation rate in total internal reflection via weak measurements,” Photonics Research **5**, 92-96 (2017).

[37] R. I. Stoian, K. V. Bui, and A. T. Rosenberger, “Silica hollow bottle resonators for use as whispering gallery mode based chemical sensors,” J. Opt. **17**, 125011 (2015).

[38] A. T. Rosenberger, “Cross-polarization coupling of whispering-gallery modes due to the spin-orbit interaction of light,” Proc. SPIE **10904**, 109041C (2019).

VITA

LIMU KE

Candidate for the Degree of

Doctor of Philosophy

Dissertation: THE DYNAMICS OF CROSS-POLARIZATION COUPLING IN A SINGLE WHISPERING-GALLERY MICRORESONATOR

Major Field: Photonics

Biographical:

Education:

Completed the requirements for the Doctor of Philosophy in Photonics at Oklahoma State University, Stillwater, Oklahoma in May, 2019.

Completed the requirements for the Bachelor of Science in Physics at Hunan University, Changsha, China in 2011.

Experience:

Microresonator optics.

Professional Memberships:

Optical Society of America (student member)